METHOD

Ranking species based on sensitivity to perturbations under non-equilibrium community dynamics

Lucas P. Medeiros[1,2] | **Stefano Allesina**[3,4] | **Vasilis Dakos**[5] | **George Sugihara**[6] | **Serguei Saavedra**[1]

[1]Department of Civil and Environmental Engineering, Massachusetts Institute of Technology, Massachusetts, Cambridge, USA

[2]Institute of Marine Sciences, University of California Santa Cruz, California, Santa Cruz, USA

[3]Department of Ecology & Evolution, University of Chicago, Illinois, Chicago, USA

[4]Northwestern Institute on Complex Systems, Northwestern University, Illinois, Evanston, USA

[5]Institut des Sciences de l'Evolution de Montpellier, Université de Montpellier, Montpellier, France

[6]Scripps Institution of Oceanography, University of California San Diego, California, La Jolla, USA

Correspondence
Lucas P. Medeiros, Institute of Marine Sciences, University of California Santa Cruz, Santa Cruz, California, USA.
Email: lumedeir@ucsc.edu

Funding information
DoD-Strategic Environmental Research and Development Program 15, Grant/Award Number: RC-2509; DOI USDI-NPS, Grant/Award Number: P20AC00527; Martin Family Society of Fellows for Sustainability; MIT Sea grant, Massachusetts Institute of Technology; National Science Foundation, Grant/Award Number: ABI-1667584, DEB-1655203 and DEB-2024349

Handling Editor: Frederick Adler

Abstract

Managing ecological communities requires fast detection of species that are sensitive to perturbations. Yet, the focus on recovery to equilibrium has prevented us from assessing species responses to perturbations when abundances fluctuate over time. Here, we introduce two data-driven approaches (expected sensitivity and eigenvector rankings) based on the time-varying Jacobian matrix to rank species over time according to their sensitivity to perturbations on abundances. Using several population dynamics models, we demonstrate that we can infer these rankings from time-series data to predict the order of species sensitivities. We find that the most sensitive species are not always the ones with the most rapidly changing or lowest abundance, which are typical criteria used to monitor populations. Finally, using two empirical time series, we show that sensitive species tend to be harder to forecast. Our results suggest that incorporating information on species interactions can improve how we manage communities out of equilibrium.

KEYWORDS
eigenvector, forecasting, Jacobian matrix, population dynamics, species interactions, time series

INTRODUCTION

Ecological communities are subject to external perturbations such as fires, storms, pollution, and overfishing, which are increasing in magnitude and frequency due

to anthropogenic impacts (Barlow et al., 2018; Jackson et al., 2001; Turner et al., 1997). Indeed, strong and frequent perturbations can lead to species extinctions and, as a consequence, to the loss of critical ecosystem services (Cardinale et al., 2012; Levin & Lubchenco, 2008).

In order to avoid the loss of biodiversity and ecosystem services under these circumstances, it is crucial to understand not only the response of the whole community to perturbations but also the response of its constituent species. Individual species may vary in their sensitivity to perturbations—that is, how much their abundance changes after a perturbation—and such sensitivity may be linked to their role in the community (Beauchesne et al., 2021; Dirzo et al., 2014; Estes et al., 2011). For instance, keystone species such as apex predators can be highly sensitive to perturbations and also crucial to maintain community functioning (Estes et al., 2011). Therefore, detecting sensitive species has the potential to greatly improve management and conservation strategies for maintaining community functioning and avoiding biodiversity loss.

Traditional studies in theoretical population ecology have established several important measures of how single species respond to perturbations (Caswell, 2000; Morris & Doak, 2002). Following these developments, indicators such as species abundance or rate of decline are routinely used to characterize the behaviour of populations and determine extinction risks (Mace et al., 2008). More recently, several studies have incorporated information on species interactions to further explore how individual species respond to perturbations (Arnoldi et al., 2018; Beauchesne et al., 2021; Medeiros et al., 2021; Saavedra et al., 2011; Weinans et al., 2019) and, in turn, how individual species can inform us about whole-community changes (i.e. best-indicator or sensor species) (Aparicio et al., 2021; Dakos, 2018; Ghadami et al., 2020; Lever et al., 2020; Patterson et al., 2021). These studies often rely on the assumption of a population dynamics model under a stable equilibrium to which the community returns after a small pulse perturbation on abundances. A pulse perturbation is defined as an instantaneous external shock (e.g. fire, storm) that causes a change in species abundance (Bender et al., 1984; Kéfi et al., 2019). Under this assumption, information on the Jacobian matrix—the matrix containing the local effects of each species on the growth rate of other species and itself (Song & Saavedra, 2021)—can be used to partition the recovery rate of the community into its constituent species (Arnoldi et al., 2018; Ives et al., 1999; Medeiros et al., 2021). A community slightly displaced from equilibrium will asymptotically return along the direction spanned by the leading eigenvector of the Jacobian matrix, that is, the eigenvector associated with the leading (i.e. largest) eigenvalue (Dakos, 2018; Patterson et al., 2021; Strogatz, 2018). Thus, over the short-term, different species may show distinct recovery rates after a perturbation depending on the direction of the leading eigenvector (Arnoldi et al., 2018; Dakos, 2018; Ghadami et al., 2020; Patterson et al., 2021; Weinans et al., 2019). Nevertheless, these ideas cannot be directly applied to communities without a stable equilibrium for which abundances fluctuate over time such as communities with cyclic or chaotic dynamics (Benincà et al., 2009, 2015; Clark & Luis, 2020; Krebs et al., 1995; Sugihara, 1994; Ushio et al., 2018). Moreover, from a practical point of view, it can be unfeasible to monitor how species respond to perturbations using parameterized models given the large amounts of data required to test model assumptions and infer parameters (Bartomeus et al., 2021; Bender et al., 1984).

These limitations raise the question of whether we can measure species responses to perturbations in communities for which dynamics are not at equilibrium. To address this problem, recent methodologies have focused on extracting information directly from abundance time series and measuring how non-equilibrium communities respond to perturbations (Cenci & Saavedra, 2019; Rogers et al., 2022; Ushio et al., 2018). Using a data-driven method known as the S-map to reconstruct the time-varying Jacobian matrix (Deyle et al., 2016; Sugihara, 1994), recent studies have investigated how communities respond to perturbations on abundances (Ushio et al., 2018) and on the governing dynamics (Cenci & Saavedra, 2019). Regarding perturbations on abundances, it has been suggested that the leading eigenvalue of the Jacobian matrix can be used to quantify how communities respond to small perturbations at any given time (Ushio et al., 2018). Differently from a recovery rate in a community with a stable equilibrium, under non-equilibrium dynamics, the leading eigenvalue approximates the local growth rate of small perturbations along a given direction (Eckmann & Ruelle, 1985; Mease et al., 2003; Vallejo et al., 2017). Thus, in contrast to a community at equilibrium with a constant capacity to recover from perturbations, a community under non-equilibrium dynamics has a response to perturbations that depends on how species abundances change over time (i.e. state-dependent) (Cenci & Saavedra, 2019). In particular, the state of a community may determine its response to perturbations not only through the local species' effects on each other (i.e. Jacobian matrix) but also through the local time scale of the dynamics (e.g. perturbation effects may take longer to appear under a long transient) (Hastings et al., 2018; Rinaldi & Scheffer, 2000). Because of such state-dependent behaviour, species abundances have been shown to be harder to forecast, on average, in states where a community is more sensitive to perturbations (Cenci et al., 2020). The question that remains to be answered is whether we can decompose a community's response to monitor the time-varying sensitivity of each of its species and whether this can complement traditional single-species indicators that do not use the information on species interactions. Developing such a species-level measure of response to perturbations could also allow us to test the hypothesis that, as observed for entire communities (Cenci et al., 2020), species that are more sensitive to perturbations at a given state are also harder to forecast.

Here, we develop two complementary approaches based on dynamical systems theory and nonlinear time

series analysis to rank species over time under non-equilibrium dynamics according to their sensitivity to small pulse perturbations on abundances. By doing so, we provide a data-driven framework to detect which species in a community are the most and least sensitive to such perturbations at any given time. Our ranking approaches consist of an analytical measure of the expected sensitivity of each species and an alignment measure of each species with the leading eigenvector of the Jacobian matrix. We test both approaches by performing perturbation analyses using five synthetic time series generated from population dynamics models. We show that we can accurately rank species sensitivities, especially using the expected sensitivity approach. However, the eigenvector approach requires no a priori information about perturbations and performs better when information about perturbations—used to compute expected sensitivities—is biased. Importantly, we show that both approaches remain accurate when inferring the Jacobian matrix directly from the time series with the S-map. Finally, we apply both approaches to two empirical time series and show that species that are more sensitive to perturbations at a given time tend to have larger abundance forecast errors, especially when the local growth rate of perturbations is high.

QUANTIFYING SPECIES SENSITIVITIES TO PERTURBATIONS

To quantify species sensitivities to perturbations, we assume that species abundances in a community with S species change through time according to a generic function: $\frac{d\mathbf{N}}{dt} = \mathbf{f}(\mathbf{N})$, where $\mathbf{f}$ ($\mathbf{f}: \mathbb{R}^S \to \mathbb{R}^S$) is an unknown nonlinear model and $\mathbf{N} = \left[N_1, \ldots, N_S\right]^\top$ is the vector of species abundances (Cenci & Saavedra, 2019). At any given time, the community can be affected by a pulse perturbation $\mathbf{p} = \left[p_1, \ldots, p_S\right]^\top$ that changes $\mathbf{N}$ into $\tilde{\mathbf{N}}$ (i.e. $\tilde{\mathbf{N}} = \mathbf{N} + \mathbf{p}$) (Bender et al., 1984). The vector $\tilde{\mathbf{N}}$ would then change in time according to $\mathbf{f}$. Following similar definitions in ecology, we conceptually define sensitivity as the amount of change in species abundances following a perturbation (Dakos, 2018; Domínguez-García et al., 2019). Mathematically, we define the sensitivity of species i to a specific perturbation $\mathbf{p}$ from time t to $t + k$ as the squared difference between its perturbed and unperturbed abundance at the time $t + k$ in relation to the initial squared difference caused by the perturbation at the time t:

$$s_i = \frac{\left[\tilde{N}_i(t+k) - N_i(t+k)\right]^2}{\left[\tilde{N}_i(t) - N_i(t)\right]^2} = \frac{p_i(t+k)^2}{p_i(t)^2}. \tag{1}$$

Therefore, s_i quantifies the distance between perturbed and unperturbed states over time, similarly to measures of sensitivity to initial conditions (Eckmann & Ruelle, 1985;

Strogatz, 2018; Vallejo et al., 2017). However, s_i is completely dependent on $\mathbf{p}$. In natural communities, we typically have no prior information about the direction and magnitude of $\mathbf{p}$—that is, there is large uncertainty about how much each species will be affected by a perturbation. To quantify species sensitivity in a way that embraces this uncertainty, we focus on a collection of randomly perturbed abundances (Arnoldi et al., 2018; Bender et al., 1984). Thus, we define the sensitivity of species i from time t to $t + k$ as the average squared difference between a set of n randomly perturbed abundances and its unperturbed abundance at the time $t + k$ in relation to the initial average squared difference at the time t:

$$\langle s_i \rangle = \frac{\frac{1}{n}\sum_{j=1}^{n}\left[\tilde{N}_i^{(j)}(t+k) - N_i(t+k)\right]^2}{\frac{1}{n}\sum_{j=1}^{n}\left[\tilde{N}_i^{(j)}(t) - N_i(t)\right]^2} = \frac{\frac{1}{n}\sum_{j=1}^{n}p_i^{(j)}(t+k)^2}{\frac{1}{n}\sum_{j=1}^{n}p_i^{(j)}(t)^2}, \tag{2}$$

where $\tilde{N}_i^{(j)}(t)$ is the jth perturbed abundance of species i at time t. The denominator in Equation (2) controls for the initial displacement of species abundances but can be ignored if the variance of perturbations is the same for every species (SI Section 4). Note that we use $\langle s_i \rangle$ as a notation for the ratio of the mean squared deviations and that $\langle s_i \rangle$ is greater than zero but not bounded because the numerator may be arbitrarily large.

Under non-equilibrium dynamics, the identity of the most and least sensitive species can change over time. We illustrate this statement using the following 3-species food chain model that exhibits chaotic dynamics (Hastings & Powell, 1991) (parameter values given in SI Section 3):

$$\begin{aligned}\frac{dN_1}{dt} &= rN_1\left(1 - \frac{N_1}{K}\right) - \frac{a_1 N_1 N_2}{1 + b_1 N_1}\\\frac{dN_2}{dt} &= -sN_2 + hN_1 N_2 - \frac{a_2 N_2 N_3}{1 + b_2 N_2}\\\frac{dN_3}{dt} &= -lN_3 + nN_2 N_3,\end{aligned} \tag{3}$$

where N_1, N_2 and N_3 are the abundances of the primary producer, primary consumer, and secondary consumer, respectively. To study species sensitivities under this model, we numerically integrate Equation (3) producing time series (Figure 1a,b) that can be visualized as an attractor in state space (Figure 1c,d). Then, we perform a small arbitrary pulse perturbation $\mathbf{p}$ to species abundances at the time t (orange vertical line in Figure 1a,b) and compute species sensitivities to it (s_i) after $k = 1$ time step (red vertical line in Figure 1a,b). We use $k = 1$ as an example here, but explore the effects of changing this time step in our analyses. Figure 1a,b shows that even under the same perturbation $\mathbf{p}$, species exhibit drastically different sensitivities depending on when the perturbation occurs. That is, the species that has the largest sensitivity to this
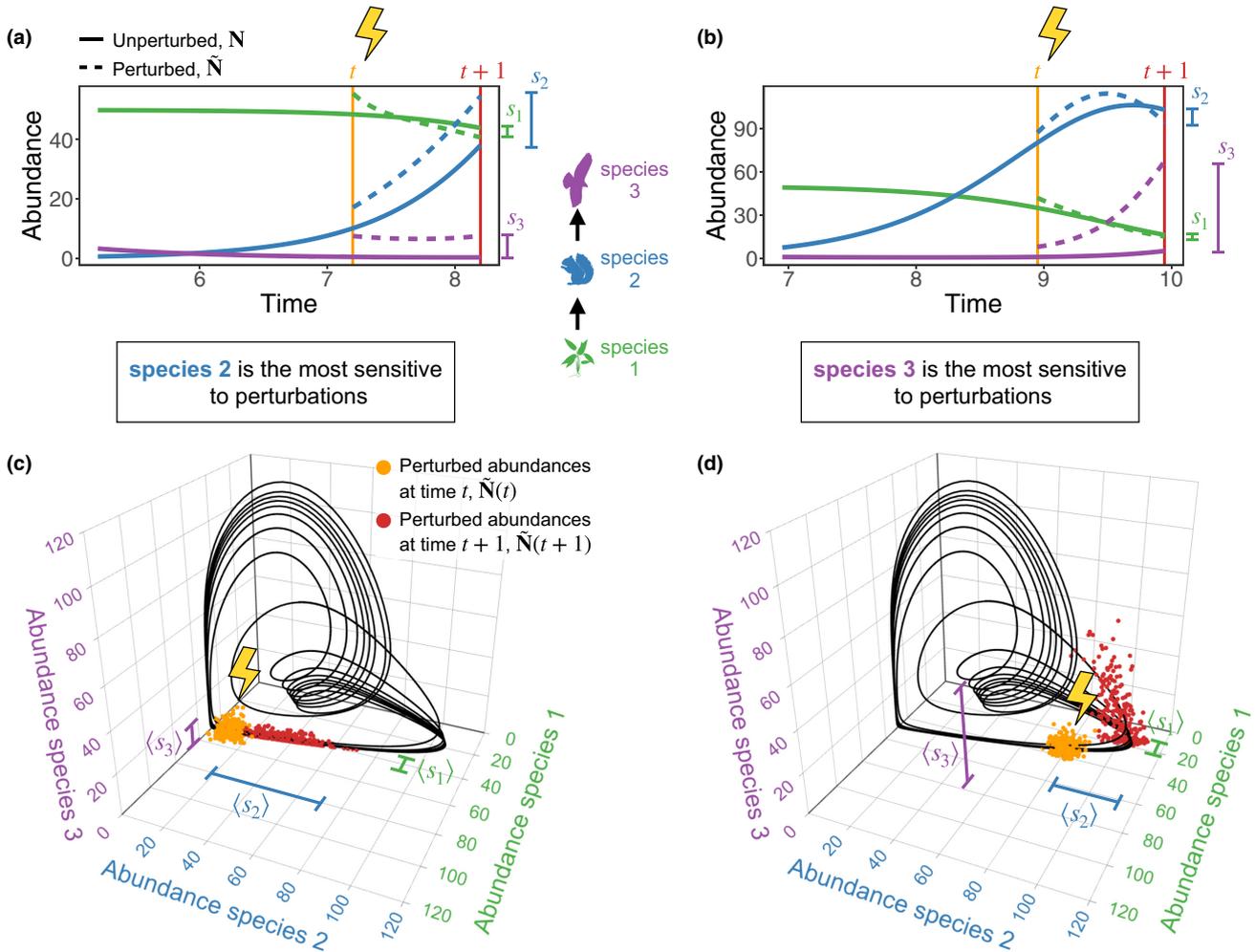
FIGURE 1 Identity of most sensitive species to perturbations changes through time under non-equilibrium dynamics. (a, b) Abundance time series generated from a 3-species chaotic food chain model (Equation 3) showing the effect of a pulse perturbation $\mathbf{p} = [7,7,7]^\top$ that increases all abundances at different times t. Whereas species 2 (primary consumer, blue) shows the highest sensitivity s_i to $\mathbf{p}$ (i.e. the largest squared difference between perturbed and unperturbed abundance at $t+1$) in (a), species 3 (secondary consumer, purple) shows the highest s_i to $\mathbf{p}$ just a few time steps ahead in (b). (c, d) Chaotic attractor of the food chain model (black) with multiple perturbed abundances around $\mathbf{N}(t)$ ($\tilde{\mathbf{N}}(t)$, orange points) at different times t. The red points show these perturbed abundances after one time step ($\tilde{\mathbf{N}}(t+1)$). We can measure the sensitivity of species i to random perturbations ($\langle s_i \rangle$) by computing the average squared difference between its set of perturbed abundances ($\tilde{N}_i(t+1)$) and its unperturbed abundance ($N_i(t+1)$) at $t+1$. Note that this sensitivity measure is normalized by the average squared difference between $\tilde{N}_i(t)$ and $N_i(t)$ at time t (Equation 2). Whereas species 2 shows the highest $\langle s_i \rangle$ in (c), species 3 shows the highest $\langle s_i \rangle$ in (d).

particular perturbation can change from the primary (species 2 in Figure 1a) to the secondary consumer (species 3 in Figure 1b) after a short time. Next, we extend this illustration and consider how multiple randomly perturbed abundances ($\tilde{\mathbf{N}}(t)$, orange points in Figure 1c,d) change after one time step ($\tilde{\mathbf{N}}(t+1)$, red points in Figure 1c,d) by computing species sensitivities ($\langle s_i \rangle$). Figure 1c,d confirms that the most sensitive species changes from the primary (species 2 in Figure 1c) to the secondary consumer (species 3 in Figure 1d) under random perturbations. Therefore, the problem we aim to solve in this study is how to predict the order of the $\langle s_i \rangle$ values of all species in a community at any given time. Clearly, in natural communities, we cannot produce multiple random perturbations to compare the responses of different species in perturbed and unperturbed communities. Therefore, in what follows, we provide a

rationale for using the Jacobian matrix at time t to predict the order of $\langle s_i \rangle$.

RANKING SPECIES SENSITIVITIES TO PERTURBATIONS

Without loss of generality, we can write the linearized dynamics of a small perturbation on abundances as $\frac{d\mathbf{p}}{dt} = \mathbf{Jp}$, where $\mathbf{J}$ is the Jacobian matrix of $\mathbf{f}$ evaluated at $\mathbf{N}$ (SI Section 1) (Boyce et al., 2017; Eckmann & Ruelle, 1985; Mease et al., 2003; Strogatz, 2018). Following results from dynamical systems theory (Arnoldi et al., 2018; Boyce et al., 2017; Strogatz, 2018), we propose two complementary approaches to rank species according to their sensitivity to perturbations (Boxes 1 and 2). These

---

BOX 1   Expected sensitivity ranking

Rationale

This approach is based on analytically computing an expected value for the sensitivity of species i to perturbations ($\mathbb{E}(s_i)$) using the solution $\mathbf{p}(t+k) = e^{\mathbf{J}k}\mathbf{p}(t)$ of the linearized dynamics (SI Section 2) (Boyce et al., 2017). Note that, for sufficiently small perturbations under equilibrium dynamics, this solution is exact because $\mathbf{J}$ is constant when evaluated at an equilibrium point ($\mathbf{N}^*$ for which $\mathbf{f}(\mathbf{N}^*) = \mathbf{0}$). By assuming that $\mathbf{p}(t)$ follows a distribution with mean zero, we can obtain $\mathbb{E}(s_i)$ at time t from the covariance matrix of $\mathbf{p}(t+k)$: $\boldsymbol{\Sigma}_{t+k} = e^{\mathbf{J}k}\boldsymbol{\Sigma}_t(e^{\mathbf{J}k})^\top$, where $\boldsymbol{\Sigma}_t$ is the covariance matrix of $\mathbf{p}(t)$. A distribution with a mean zero for $\mathbf{p}(t)$ represents the most uninformative case where all perturbation directions (i.e. which species are most impacted) are equally likely to occur. Thus, the distribution of perturbed abundances ($\tilde{\mathbf{N}}$) described by $\boldsymbol{\Sigma}_t$ will approximate $\boldsymbol{\Sigma}_{t+k}$ after k time steps (Figure 2a). Then, we can compute the expected sensitivity of species i as: $\mathbb{E}(s_i) = \sigma^2_{i,t+k}$, where $\sigma^2_{i,t+k}$ is the ith diagonal element of $\boldsymbol{\Sigma}_{t+k}$ (i.e. the variance of $p_i(t+k)$). We define the order of $\mathbb{E}(s_i)$ values across species as the expected sensitivity ranking and use it to predict the order of species sensitivities to perturbations ($\langle s_i \rangle$; Figure 2a).

Application

Three ingredients are required to apply the expected sensitivity ranking. First, we need the Jacobian matrix of the community ($\mathbf{J}$) evaluated using the abundances ($\mathbf{N}$) at time t. This matrix can be computed directly from a parameterized population dynamics model (SI Section 1) or, as we focus here, inferred from the time series without assuming a specific model (SI Section 5). Second, we need to define an initial covariance matrix of perturbations at time t ($\boldsymbol{\Sigma}_t$). Without any knowledge of perturbations, we suggest an uninformative approach by setting $\boldsymbol{\Sigma}_t = \mathbf{I}$, where $\mathbf{I}$ is the identity matrix (i.e. perturbations to each species are independent of each other). Finally, we need to specify the time for which perturbations evolve (k) on the time unit of the time series (e.g. day, month). Because information on the local time scale of the dynamics can be challenging to obtain, we suggest using a small value for k to investigate short-term species sensitivities (e.g. $k = 1$). Alternatively, it is possible to set k to be inversely proportional to the local rate of change calculated from the time series (SI Section 4). In conclusion, although this approach has the advantage of using the information on the entire Jacobian matrix to compute $\mathbb{E}(s_i)$, it has the disadvantage of requiring additional information that may be hard to obtain in natural communities ($\boldsymbol{\Sigma}_t$ and k).

---

approaches are based on the assumption that if $\mathbf{J}$ is nearly constant from time t to $t+k$, the solution $\mathbf{p}(t+k)$ of the linearized dynamics provides a good approximation of how perturbed abundances change over this time period. Thus, in addition to the challenge of approximating a nonlinear system (i.e. $\mathbf{f}(\mathbf{N})$) by its linearized dynamics, here we explore the extent to which the linearized dynamics inform us about species sensitivities under non-equilibrium dynamics (i.e. when $\mathbf{J}$ is state-dependent). Importantly, we use information from the Jacobian matrix (i.e. community-level information) to measure how individual species respond to perturbations.

We illustrate how $\mathbb{E}(s_i)$ (Box 1) and $|\mathbf{v}_{1i}|$ (Box 2) allow us to predict the order of $\langle s_i \rangle$ under three simple scenarios of Lotka-Volterra dynamics at equilibrium (SI Section 13). These examples contain an unstable equilibrium point—that is, $\mathbf{J}$ evaluated at $\mathbf{N}^*$ has at least one $\lambda_i > 0$, as is typically observed for points along a non-equilibrium attractor (e.g. limit cycle, chaotic attractor). We show that the order of $\mathbb{E}(s_i)$ is exactly the same as the order of $\langle s_i \rangle$, whereas the order of $|\mathbf{v}_{1i}|$ is similar to the order of $\langle s_i \rangle$ for all three scenarios (Figures S1–S3). A potential limitation of these approaches, however, is that they rely on a parameterized model ($\mathbf{f}$) to obtain $\mathbf{J}$,

which we rarely have. Therefore, in addition to computing $\mathbb{E}(s_i)$ and $|\mathbf{v}_{1i}|$ using the analytical $\mathbf{J}$, we show that we can accurately rank $\langle s_i \rangle$ by inferring $\mathbf{J}$ using the S-map. The S-map is a locally weighted state-space regression method that has been shown to provide accurate inferences of the time-varying Jacobian matrix from time series (Cenci et al., 2019; Deyle et al., 2016; Sugihara, 1994) (SI Section 5).

TESTING RANKING APPROACHES WITH SYNTHETIC TIME SERIES

To test whether the order of expected sensitivities ($\mathbb{E}(s_i)$; Box 1) and eigenvector alignments ($|\mathbf{v}_{1i}|$; Box 2) can predict the order of species sensitivities ($\langle s_i \rangle$), we perform perturbation analyses using synthetic time series. Specifically, we generate multivariate time series with 500 points ($\{\mathbf{N}(t)\}$, $t = 1, \ldots, 500$) using five population dynamics models that produce non-equilibrium dynamics (Figure S5; SI Section 3). Then, for half of each time series ($t = 250, \ldots, 500$), we perform $n = 300$ random perturbations at each time t: $\tilde{\mathbf{N}} = \mathbf{N} + \mathbf{p}$, where $\mathbf{p} \sim \mathcal{N}(\mathbf{0}, \boldsymbol{\Sigma}_t)$ with $\boldsymbol{\Sigma}_t$ being a diagonal matrix with diagonal element i
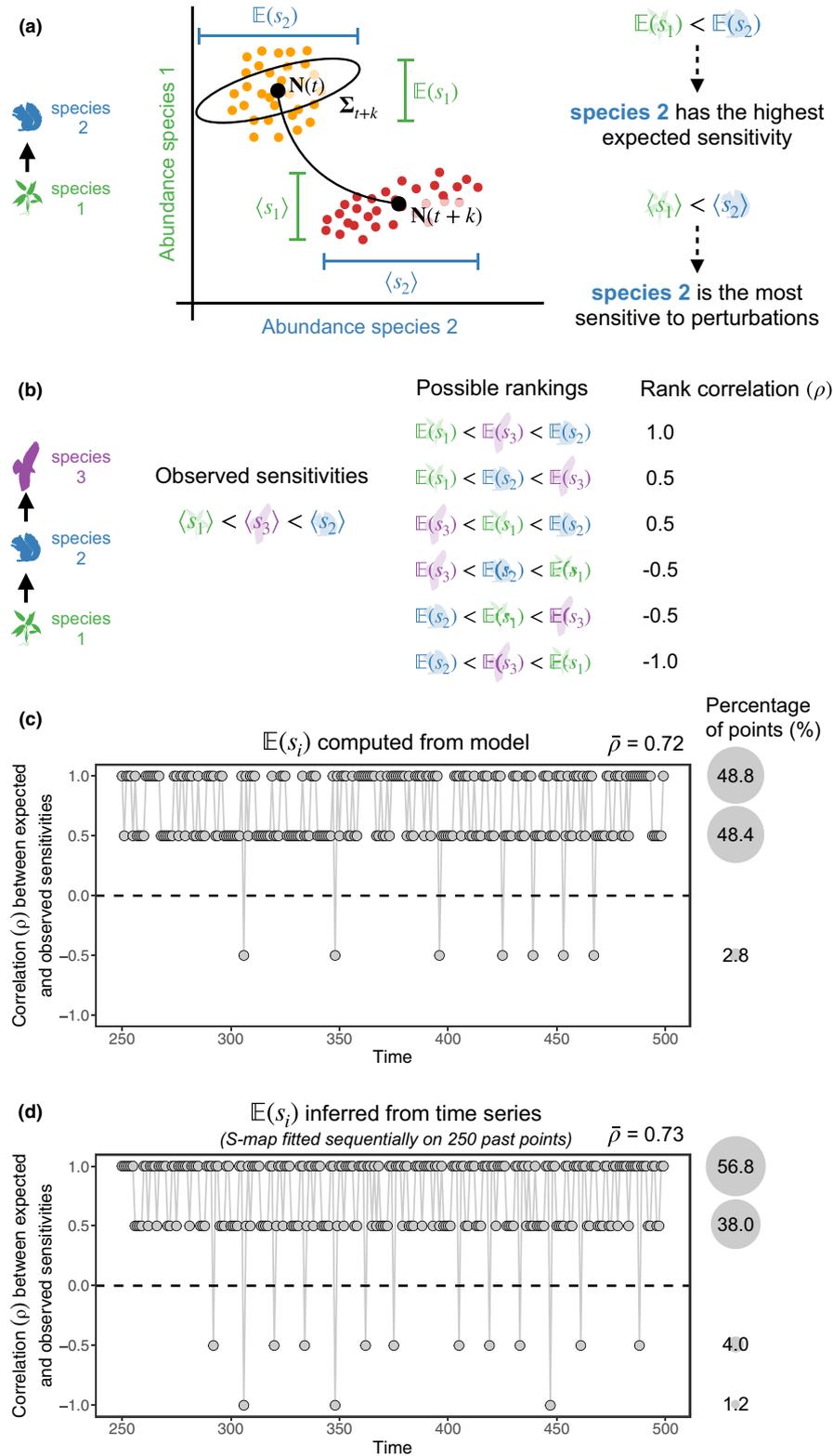
FIGURE 2 Ranking species sensitivities to perturbations. (a) Illustration with two species showing the expansion of perturbed abundances ($\tilde{\mathbf{N}}(t)$, orange points) after k time steps ($\tilde{\mathbf{N}}(t+k)$, red points). The expected sensitivity of species i to perturbations ($\mathbb{E}(s_i)$) can be computed as the corresponding variance of the predicted distribution of perturbations (i.e. ith diagonal element of covariance matrix $\mathbf{\Sigma}_{t+k}$ depicted in black). Note that $\mathbf{\Sigma}_{t+k}$ is shown at time t as it is computed using only information at that time point. We propose that the order of $\mathbb{E}(s_i)$ values can be used to predict the order of species sensitivities to perturbations ($\langle s_i \rangle$ values). Alternatively, the order of species alignments with the leading eigenvector of the Jacobian matrix ($|\mathbf{v}_{1i}|$ values) can be used to predict the order of $\langle s_i \rangle$ values. (b) for the 3-species food chain model (Equation 3) at a given time, there are six possible ways to rank $\langle s_i \rangle$ values, each one giving a Spearman's rank correlation value (ρ). (c) Rank correlation (ρ) between $\mathbb{E}(s_i)$ (computed analytically from the model) and $\langle s_i \rangle$ over time quantified for a synthetic time series generated from the 3-species food chain model. The vast majority of points (97.2%) show a positive ρ. (d) Same as (c) but with the Jacobian matrix used to compute $\mathbb{E}(s_i)$ inferred with the S-map using only past time-series data. Again, the great majority of points (94.8%) show a positive ρ.

BOX 2 Eigenvector ranking

Rationale

This approach is based on the alignment of species i with the leading eigenvector ($\mathbf{v}_1$) of $\mathbf{J} \mid \mathbf{v}_{1i} \mid$. The solution of the linearized dynamics can also be written as $\mathbf{p}(t + k) = \sum_{i=1}^{S} c_i e^{\lambda_i k} \mathbf{v}_i$, where $\mathbf{v}_i$ is the real part of the ith eigenvector of $\mathbf{J}$, λ_i is the real part of the ith eigenvalue $\left(\lambda_S \leq \cdots \leq \lambda_1 \right)$, and each c_i is a constant determined by the initial condition $\mathbf{p}(t)$ (SI Section 9) (Boyce et al., 2017, Strogatz, 2018). As long as the imaginary parts are small compared to real parts, $\mid \mathbf{v}_{1i} \mid$ can still be used to estimate species sensitivities even under small local oscillations caused by complex eigenvalues (SI Section 9). After a sufficient amount of time k, λ_1 will dominate over other eigenvalues and the solution can be approximated by $\mathbf{p}(t + k) \approx c_1 e^{\lambda_1 k} \mathbf{v}_1$. Thus, $\mathbf{v}_1$ dictates the local direction of the greatest expansion (or smallest contraction) of perturbations. That is, the distribution of perturbed abundances ($\tilde{\mathbf{N}}$) will expand over time approximately along the direction of $\mathbf{v}_1$ and at a rate given by λ_1 (positive values lead to expansion, whereas negative values lead to contraction). We also show that $\mathbf{v}_1$ serves as a proxy for the local leading Lyapunov vector, which provides the exact direction of perturbation growth under non-equilibrium dynamics (Kuptsov & Parlitz, 2012; Mease et al., 2003; Vallejo et al., 2017) (Figure S4; SI Section 10). Specifically, we compute the alignment of species i with $\mathbf{v}_1$ as the absolute value of its ith element ($\mid \mathbf{v}_{1i} \mid$), where $\| \mathbf{v}_1 \| = 1$. We define the order of $\mid \mathbf{v}_{1i} \mid$ values across species as the eigenvector ranking and use it to predict the order of $\langle s_i \rangle$ (SI Section 11). Note that we use the absolute value because only the line spanned by $\mathbf{v}_1$ and not its direction determines how perturbed abundances change over time.

Application

Similarly to the expected sensitivity ranking, the Jacobian matrix of the community ($\mathbf{J}$) evaluated using the abundances ($\mathbf{N}$) at time t is also required to apply the eigenvector ranking. The main advantage of the eigenvector ranking is that $\mathbf{J}$ is the only ingredient required to compute $\mid \mathbf{v}_{1i} \mid$ and we do not need to specify the initial covariance matrix of perturbations ($\mathbf{\Sigma}_t$) nor the time for which perturbations evolve (k). Nevertheless, using a single eigenvector instead of the entire Jacobian matrix, the eigenvector ranking uses less information than the expected sensitivity ranking. Importantly, we show that $\mathbb{E}(s_i)$ and $\mid \mathbf{v}_{1i} \mid$ are related in the special case of a symmetric $\mathbf{J}$ (SI Section 12), which is also when all eigenvalues of $\mathbf{J}$ are real.

---

given by $\sigma_{i,t}^2 = r^2$ (i.e. independent normally distributed perturbations for each species with the same variance r^2). We set r to be 15% of the mean standard deviation of species abundances, but relax this assumption in additional analyses (SI Section 4). Next, we numerically integrate the model $\mathbf{f}$ for a time k using each $\tilde{\mathbf{N}}$ as an initial condition. Because the response of communities to perturbations can depend on the time scale of the dynamics (Hastings et al., 2018; Rinaldi & Scheffer, 2000), we set k to be inversely proportional to the mean rate of change of the dynamics (SI Section 4). Then, we compute $\langle s_i \rangle$ from time t to $t + k$ as well as $\mathbb{E}(s_i)$ and $\mid \mathbf{v}_{1i} \mid$ using $\mathbf{J}$ at time t as described in Boxes 1 and 2. We compute $\mathbb{E}(s_i)$ and $\mid \mathbf{v}_{1i} \mid$ both analytically from the true $\mathbf{J}$ evaluated at $\mathbf{N}$ and by sequentially inferring $\mathbf{J}$ with the S-map on 250 past points.

To assess how well the order of $\mathbb{E}(s_i)$ and $\mid \mathbf{v}_{1i} \mid$ predicts the order of $\langle s_i \rangle$, we compute the Spearman's rank correlation (ρ) between each ranking and $\langle s_i \rangle$ at each time t. We focus on predicting the order instead of the exact values of $\langle s_i \rangle$ for two reasons. First, the exact values of $\langle s_i \rangle$ depend on the initial covariance matrix $\mathbf{\Sigma}_t$ and on the time step k, which we rarely know for natural communities. Second, we can only infer an approximation of $\mathbf{J}$ with the S-map even from ideal time-series data (SI Section 5; Cenci & Saavedra, 2019). We can illustrate our

ranking procedure for $\mathbb{E}(s_i)$ by considering the 3-species food chain model (Figure 1; Equation 3). With 3 species, there are 6 possible ways to rank a given set of $\langle s_i \rangle$ at any given time, resulting in 4 different ρ values (Figure 2b). If the order of $\mathbb{E}(s_i)$ matches the order of $\langle s_i \rangle$ exactly, we obtain $\rho = 1$ (Figure 2b). Otherwise, ρ decreases depending on the mismatch between the order of $\mathbb{E}(s_i)$ and the order of $\langle s_i \rangle$. An advantage of using ρ is that it allows us to penalize prediction mistakes consistently, irrespective of whether the mistaken species are amongst the most or least sensitive ones. For example, in Figure 2b, the second and third rankings have   because both contain one correct prediction, which is the least sensitive species and the most sensitive species, respectively. Under the 3-species food chain model, we find that the order of   matches the order of $\langle s_i \rangle$ exactly (i.e. $\rho = 1$; Figure 2c) for 48.8% of points in the time series. For another 48.4% of points, the order of $\mathbb{E}(s_i)$ allows us to correctly detect the position of either the least or most sensitive species (i.e. $\rho = 0.5$). Finally, for 2.8% of points, the order of $\mathbb{E}(s_i)$ is not a good predictor of the order of $\langle s_i \rangle$ (i.e. $\rho < 0$). But most strikingly, we obtain very similar results when inferring $\mathbb{E}(s_i)$ directly from the synthetic time series using the S-map, without any knowledge of the underlying model (Figure 2d). Hence, this illustration suggests that we can accurately predict the relative

sensitivity position of most species (i.e. $\rho \geq 0.5$) for the vast majority of points in a time series.

To benchmark our approaches, we use two simple single-species indicators to predict the order of $\langle s_i \rangle$ values. First, we use abundances absolute percent change between $t-1$ and t: $\Delta N_i(t) = \left| \frac{N_i(t) - N_i(t-1)}{N_i(t-1)} \right|$. The rationale for this indicator is that a species will be more sensitive when its abundance is changing more rapidly. Second, we use abundances at time t after a sign reversal: $-N_i(t)$. This indicator is based on the notion that a species will be more sensitive when it has a low abundance, for example, due to density dependence effects. For both indicators, we compute the rank correlation ρ between $\langle s_i \rangle$ and the indicator at each time t. Note that computing $\Delta N_i(t)$ or $-N_i(t)$ for a given species i only requires species-level information (i.e. time series of species i) and not community-level information (i.e. Jacobian matrix) as $\mathbb{E}(s_i)$ and $|\mathbf{v}_{1i}|$ require.

We demonstrate the generality of our ranking approaches using the set of five synthetic time series (SI Section 3). Although we find a high variation in ρ over time (grey points in Figure 3a), the mean correlation $\bar{\rho}$ between $\langle s_i \rangle$ and $\mathbb{E}(s_i)$ as well as between $\langle s_i \rangle$ and $|\mathbf{v}_{1i}|$ is positive and high for all five models when we compute these rankings from the model (horizontal lines in Figure 3a). In particular, we find that $\mathbb{E}(s_i)$ shows the higher accuracy in ranking $\langle s_i \rangle$, followed by $|\mathbf{v}_{1i}|$, $\Delta N_i(t)$, and $-N_i(t)$. Note that we focus on $\bar{\rho}$ given that ρ is expected to vary over time due to changes in nonlinearity and rate of change of $\mathbf{J}$. Importantly, we obtain very similar results for all models when inferring $\mathbb{E}(s_i)$ and $|\mathbf{v}_{1i}|$ using the S-map (horizontal lines in Figure 3b). In addition to quantifying prediction accuracy, we can visualize how the value of $\langle s_i \rangle$, $\mathbb{E}(s_i)$, and $|\mathbf{v}_{1i}|$ of each species changes over time (Figure S6). We find that, even when inferring $\mathbb{E}(s_i)$ and $|\mathbf{v}_{1i}|$ with the S-map, we are able to detect shifts in $\langle s_i \rangle$ across species (Figure S6).

Although $\mathbb{E}(s_i)$ is in general more accurate than $|\mathbf{v}_{1i}|$, we can use information on the leading eigenvalue (λ_1) to increase the accuracy of the latter approach. We expect that the higher λ_1, the greater the local growth rate of perturbations in the direction of $\mathbf{v}_1$, which should improve our ability to rank $\langle s_i \rangle$ using $|\mathbf{v}_{1i}|$. For the non-equilibrium attractors used here, λ_1 is generally positive, whereas subsequent eigenvalues are negative or close to zero, implying that λ_1 alone carries enough information to improve the eigenvector approach. Indeed, we find that $\bar{\rho}$ generally increases for the eigenvector approach when using only a subset of points with a high value of λ_1 (Figure S7). We also find a positive correlation between the analytical and inferred λ_1 (2-species predator–prey: 0.52; 3-species food chain: 0.70; 3-species food web: 0.57; 4-species competitors: 0.23; and 5-species food web: 0.70) and a high alignment between the analytical and inferred $\mathbf{v}_1$ for all models (Figure S8).

For most models, the expected sensitivity ($\mathbb{E}(s_i)$) and eigenvector ($|\mathbf{v}_{1i}|$) approaches computed from the analytical $\mathbf{J}$ show a high accuracy in ranking species sensitivities ($\langle s_i \rangle$) when using different perturbation distributions (Figures S9 and S10) or time steps (k) to evolve perturbations (Figures S11 and S12; SI Section 4). In particular, $\mathbb{E}(s_i)$ shows an extremely high accuracy when k is small and fixed over time (e.g. $k = 1$; Figure S11), given that the solution for the linearized dynamics ($\mathbf{p}(t+k)$) is more precise for smaller k. In contrast, we find that $|\mathbf{v}_{1i}|$ performs best when k depends on the time scale of the dynamics (Figure 3), given that the eigenvector approach depends on the convergence of $\mathbf{p}(t+k)$ to the line spanned by $\mathbf{v}_1$, which requires a larger k when dynamics are slower. We also find that the accuracy of $\mathbb{E}(s_i)$ computed using wrong values of k and Σ_t remains high (Figures S10 and S13), except when these values are greatly misspecified (Figure S14). Finally, although the accuracy decreases in some cases, we find that $\mathbb{E}(s_i)$ and $|\mathbf{v}_{1i}|$ inferred with the S-map remain accurate when normalizing species abundances (Figure S15), using shorter time series (Figure S16), adding observational noise to the time series (Figure S17) or adding process noise to the model (Figure S18; SI Section 6).

DETECTING SENSITIVE SPECIES IN EMPIRICAL TIME SERIES

To illustrate the implementation of our data-driven approaches, we apply them to rank species sensitivities (Boxes 1 and 2) using two empirical time series. Each time series depicts a different marine community with four interacting variables that have been shown to exhibit non-equilibrium dynamics (SI Section 7; Benincà et al., 2009, 2015). Note that some variables represent physical attributes (e.g. bare rock) and others consist of species aggregations (e.g. barnacles) but we use the term species to refer to all variables. We first fit the S-map sequentially to both time series to infer $\mathbb{E}(s_i)$ and $|\mathbf{v}_{1i}|$ (SI Section 7). Because we do not know the governing population dynamics in these communities (i.e. $\mathbf{f(N)}$), we cannot compute $\langle s_i \rangle$. Instead, we perform abundance forecasts using a Long Short-Term Memory (LSTM) neural network (James et al., 2021) and test the hypothesis that species that are more sensitive to perturbations (i.e. have a higher value of $\mathbb{E}(s_i)$ or $|\mathbf{v}_{1i}|$) at a given time will be harder to forecast. That is, for a community under perturbations, the LSTM neural network will not be able to accurately forecast the abundance of a given species at a point in time when that species is highly sensitive to perturbations (Cenci et al., 2020). Both empirical communities described above are thought to be under perturbations triggered by changes in environmental conditions (Benincà et al., 2009, 2015).

For both the Jacobian matrix inference (i.e. S-map) and the forecasts (i.e. LSTM neural network), we assign 70% of the data as a training set and use the remaining 30% as a test set. For each time t in the test set, we

(a)

(b)
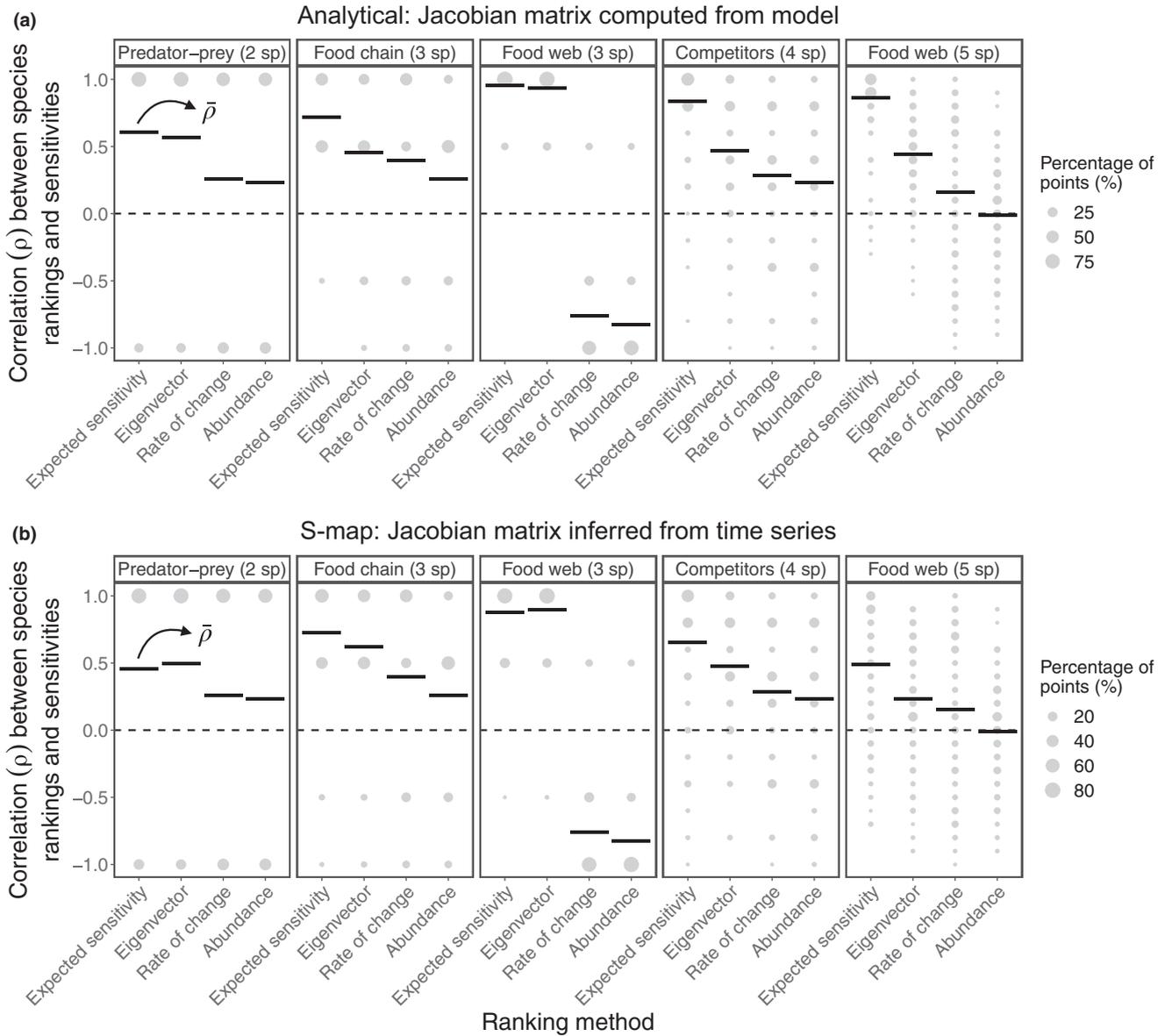
FIGURE 3 Expected sensitivity and eigenvector approaches allow us to accurately rank species sensitivities to perturbations under several population dynamics models. (a) Rank correlation (ρ) between species sensitivities to perturbations ($\langle s_i \rangle$) and four different approaches (expected sensitivity, $\mathbb{E}(s_i)$; eigenvector, $|\mathbf{v}_{1i}|$; rate of change, $\Delta N_i(t)$; and abundance, $-N_i(t)$). Note that the Jacobian matrix and, therefore, $\mathbb{E}(s_i)$ and $|\mathbf{v}_{1i}|$ are computed analytically from the model. Each panel shows the percentage of points with a given ρ value (size of grey points) and the average of these values across time ($\bar{\rho}$, black horizontal lines) for a synthetic time series generated from the corresponding population dynamics model. (b) Same as (a) but with the Jacobian matrix and, therefore, $\mathbb{E}(s_i)$ and $|\mathbf{v}_{1i}|$ inferred with the S-map using only past time-series data. In (a), the expected sensitivity approach shows a higher $\bar{\rho}$ than the other three ranking approaches under all models. In (b), the expected sensitivity approach outperforms the eigenvector approach for three out of five models.

compute a standardized forecast root-mean-square error (RMSE) for each species i as (Perretti et al., 2013):

$$\epsilon_i = \frac{\sqrt{\frac{1}{\tau} \sum_{j=t}^{t+\tau-1} \left[N_i(j) - \hat{N}_i(j) \right]^2}}{\sqrt{\frac{1}{\tau} \sum_{j=t}^{t+\tau-1} \left[N_i(j) - N_i(t-1) \right]^2}}, \qquad (4)$$

where $\tau = 3$ is the number of forecasts, the numerator is the RMSE for the LSTM neural network forecast ($\hat{N}_i(j)$), and the denominator is the RMSE for a naive forecast using the

last point in the current training set ($N_i(t-1)$). We then compute the rank correlation (ρ) between $\mathbb{E}(s_i)$ and ϵ_i as well as between $|\mathbf{v}_{1i}|$ and ϵ_i at each point in the test set to test the hypothesis that our rankings can predict the order of forecast errors. We also compute the rank correlation between each of the two alternative indicators previously described ($\Delta N_i(t)$ and $-N_i(t)$) and ϵ_i to verify whether these single-species indicators can predict the order of forecast errors. Because we do not know how perturbations affect these communities, we set $\Sigma_t = \mathbf{I}$ and $k = \tau$ to compute $\mathbb{E}(s_i)$ (Box 1). We confirm the rationale behind

our hypothesis by performing forecasts under perturbations with the five models used in our theoretical analyses (Figure S19; SI Section 8).

We first illustrate our approaches to detect sensitive species with a rocky intertidal community. We find that barnacles have the highest expected sensitivity ($\mathbb{E}(s_i)$) followed by either algae or mussels depending on the point in time (Figure 4a and Figure S20). Interestingly, barnacles also show the highest alignment with the leading eigenvector ($|\mathbf{v}_{1i}|$) for the majority of points in time (Figure S20). We also find consistent results for $\mathbb{E}(s_i)$ and $|\mathbf{v}_{1i}|$ with a marine plankton community (Figures S20 and S21). Thus, although the values of $\mathbb{E}(s_i)$ over time are different from those of $|\mathbf{v}_{1i}|$, these two complementary approaches suggest some general patterns in how species sensitivities change over time in these two communities. Importantly, we find that the mean rank correlation $\overline{\rho}$ between $\mathbb{E}(s_i)$ and ϵ_i is positive for both time series, but only significant for one of them (rocky intertidal community: $\overline{\rho} = 0.04$, p-value = 0.287, 1000 randomizations; marine plankton community: $\overline{\rho} = 0.23$, p-value <0.001; Figure 4b). However, we find that the mean rank correlation $\overline{\rho}$ between $|\mathbf{v}_{1i}|$ and ϵ_i is positive and significant for both
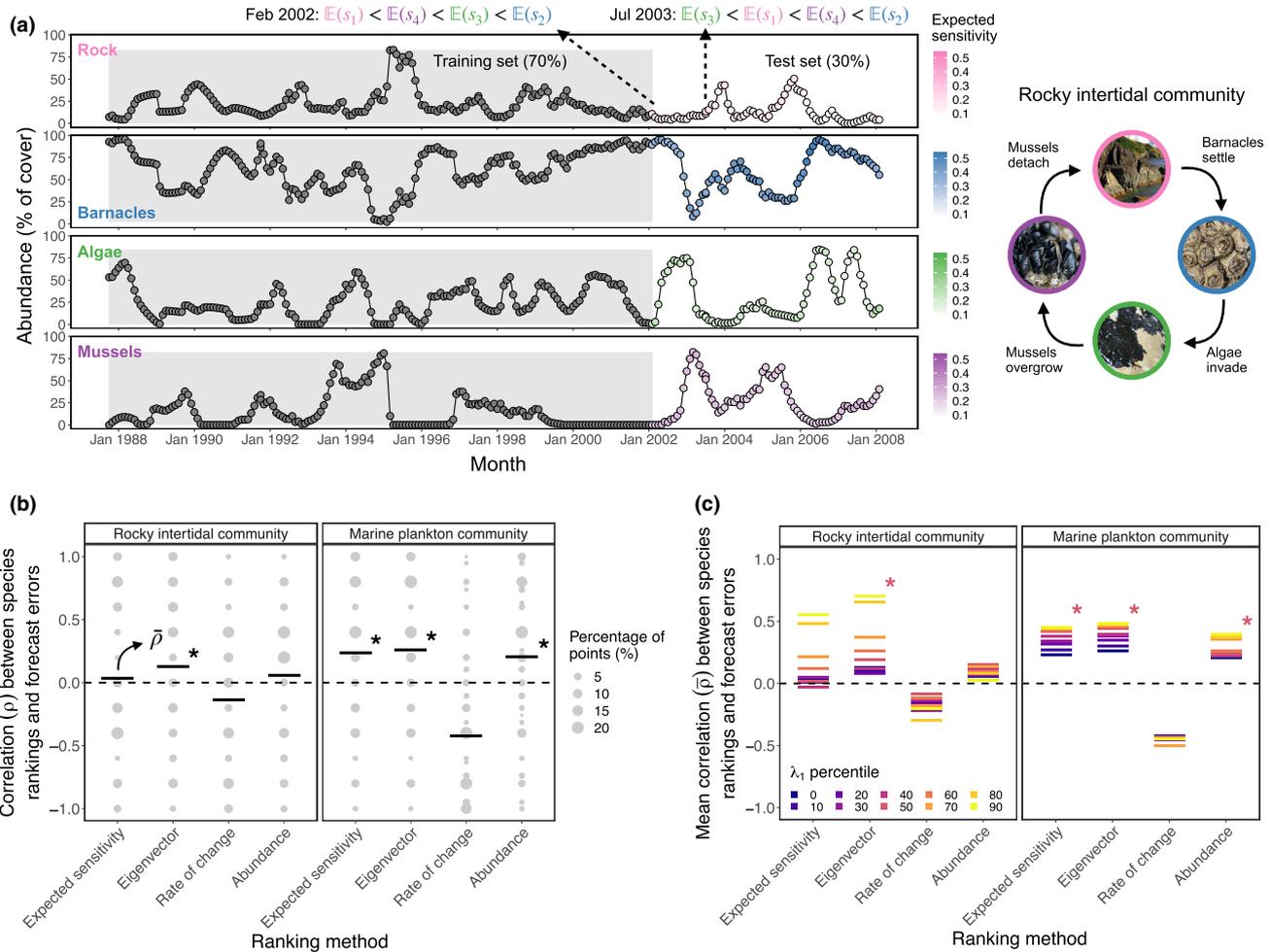
FIGURE 4 Species abundance forecast errors are associated with species sensitivities to perturbations. (a) Time series of a rocky intertidal community containing four variables (bare rock, barnacles, algae, and mussels). The diagram on the right depicts the cyclic succession in this community (adapted from Benincà et al., 2015). Note that percentage of cover does not necessarily sum to 100% as individuals of different species may overlap on top of the rock. We use a moving training set (grey region) to train the S-map and compute expected sensitivities ($\mathbb{E}(s_i)$) as well as species alignments with the leading eigenvector ($|\mathbf{v}_{1i}|$) at the last point in the training set. Simultaneously, we train an LSTM neural network to forecast species abundances and compute species forecast errors (ϵ_i). Barnacles (blue) show the highest value of $\mathbb{E}(s_i)$ followed by either algae (green) or mussels (purple) depending on the point in time. Note that $\mathbb{E}(s_i)$ values across species sum to 1 for each point in time (darker points denote higher $\mathbb{E}(s_i)$). (b) Rank correlation (ρ) between ϵ_i and four different approaches (expected sensitivity, $\mathbb{E}(s_i)$; eigenvector, $|\mathbf{v}_{1i}|$; rate of change, $\Delta N_i(t)$; and abundance, $-N_i(t)$). Each panel shows the percentage of points with a given ρ value (size of grey points) and the average of these values over the test set ($\overline{\rho}$, black horizontal lines) for a given empirical time series (asterisks denote a p-value less than 0.05 for $\overline{\rho}$ according to a randomization test). (c) Average correlation ($\overline{\rho}$) between ϵ_i and the different ranking approaches computed for points in the test set with a λ_1 value higher than a given percentile of the λ_1 distribution. For the expected sensitivity and eigenvector approaches, $\overline{\rho}$ increases as we only use points with successively higher values of λ_1 for both time series (asterisks denote a p-value less than 0.05 for $\overline{\rho}$ using the 50th percentile). Pictures are under the creative commons Licence: Rock by Piotr Zurek, barnacles by tangatawhenua, algae by redrovertracy, and mussels by Wayne Martin.

time series (rocky intertidal community: $\overline{\rho} = 0.13$, p-value = 0.023; marine plankton community: $\overline{\rho} = 0.26$, p-value <0.001; Figure 4b).

We find further evidence that species with higher $\mathbb{E}(s_i)$ or $|\mathbf{v}_{1i}|$ are harder to forecast by computing $\overline{\rho}$ only for points in the test set with successively higher values of λ_1 (i.e. higher local growth rate of perturbations; Figure 4c). For example, as expected from our analyses with synthetic time series (Figure S7), $\overline{\rho}$ between $|\mathbf{v}_{1i}|$ and ϵ_i increases for both time series when we only use points for which λ_1 is higher than its 50th percentile (rocky intertidal community: $\overline{\rho} = 0.19$, p-value = 0.021; marine plankton community: $\overline{\rho} = 0.45$, p-value <0.001; Figure 4c). The fact that $\overline{\rho}$ does not increase in general by using only points with a high λ_1 for the alternative indicators ($\Delta N_i(t)$ and $-N_i(t)$) supports our ranking approaches in linking species forecast errors to their sensitivities (Figure 4c). We find these results to remain similar when changing the size of the training set and the number of steps ahead (τ) to forecast (Figures S22–S24) as well as to normalize species abundances before performing the S-map (Figure S25).

DISCUSSION

Understanding how individual species affect the response to perturbations of the whole community and, in turn, how species interactions at the community level affect the responses of individual species is paramount to ecological management and conservation (Beauchesne et al., 2021; Clark et al., 2021; Kéfi et al., 2019; Levin & Lubchenco, 2008). Yet, the traditional focus of ecology on recovery to equilibrium using parameterized models has hampered efforts to understand how species respond to perturbations when community dynamics are out of equilibrium. Here, we introduce a data-driven framework to solve a previously unexplored problem: how to rank the species that compose a community according to their sensitivity to small pulse perturbations under non-equilibrium dynamics? Our findings provide three main insights into how communities and their constituent species respond to perturbations.

First, we show that information on the time-varying local effects between interacting species (i.e. Jacobian matrix) can be used to determine which species will be most affected by perturbations at a given time. In particular, using dynamical systems theory (Arnoldi et al., 2018; Mease et al., 2003; Strogatz, 2018) and non-linear time series methods (Cenci et al., 2019; Deyle et al., 2016; Sugihara, 1994), we develop two complementary approaches that can accurately rank species from most to least sensitive to small perturbations on abundances under non-equilibrium dynamics. Both the expected sensitivity and the eigenvector ranking allow us to detect which of the species that compose a natural community are the most and least sensitive in real time if a long-time series is available. Hence, it may be possible

to inform management and conservation programs regarding which species are currently the most sensitive ones. Our measure of sensitivity uses community-level information to quantify the likelihood of large changes (either decreases or increases) in the abundance of a given species. Therefore, species sensitivities may complement indicators that estimate single-species vulnerability to perturbations (Caswell, 2000; Mace et al., 2008; Morris & Doak, 2002). That is, whilst some species obviously require constant monitoring due to a high extinction risk (Dirzo et al., 2014; Estes et al., 2011), other species may require more attention during periods of time when they have a high sensitivity, irrespective of their abundance. Our results, however, cannot be extrapolated beyond a given studied community as our framework uses information on that specific community to rank species sensitivities.

Importantly, the expected sensitivity ranking is more accurate than the eigenvector ranking for most of our perturbation analyses with synthetic time series. In particular, the expected sensitivity ranking has its best performance when the time over which perturbations evolve (k) is small and fixed, and its worse performance when the covariance matrix of perturbations ($\mathbf{\Sigma}_t$) and k are greatly misspecified. In contrast, the eigenvector ranking has the advantage of not depending on $\mathbf{\Sigma}_t$ and k for its computation and has its best performance when k depends on the local time scale of the dynamics. Indeed, in communities under non-equilibrium dynamics, large differences in time scale and, therefore, in the time it takes for perturbation effects to appear are widespread (Hastings et al., 2018; Rinaldi & Scheffer, 2000; Strogatz, 2018). Thus, it is reasonable to expect that as a practical tool the heuristic eigenvector ranking may be as useful as the more theoretically complete but assumption bound expected sensitivity ranking.

Second, we find support for our hypothesis that the abundance forecast errors for the different species in a community are associated with their sensitivity to perturbations. The predictability of ecological dynamics is known to change across communities (Dietze, 2017; Pennekamp et al., 2019) and, for a single community, across time (Cenci et al., 2020). In particular, it has been shown that at points in time when a community is more sensitive to perturbations its local predictability can be lower and, therefore, the average abundance forecast error can be higher (Cenci et al., 2020). Here, we have extended this result for individual species by showing that the local predictability of a given species is associated with its sensitivity to perturbations, which we infer through its expected sensitivity and its alignment with the leading eigenvector. The fact that the correlation between forecast errors and our ranking approaches strengthens when the leading eigenvalue is high (i.e. perturbations grow rapidly along a given direction in state space) further supports our hypothesis that species forecast errors are associated with their sensitivities. In

addition, the better performance with empirical data of the eigenvector approach in relation to the expected sensitivity approach suggests that we may be misspecifying the information required to compute expected sensitivities. These results provide empirical support to the leading eigenvector as a way to detect sensitive species using minimal information inferred from time-series data. Overall, our findings suggest that sensitivity to perturbations is an additional factor influencing the intrinsic predictability of different species in ecological communities (Dietze, 2017, Pennekamp et al., 2019).

Applying our ranking approaches to empirical data requires accurate inference of the Jacobian matrix with the S-map. Although the S-map has been shown to provide accurate inferences when time series are noisy (Cenci et al., 2019; Deyle et al., 2016), several limitations remain. Because information on the shape of the attractor is required to fit the S-map, longer time series with smaller amounts of noise improve inference quality, all else being equal. In our analyses with synthetic time series, we show that our ranking approaches remain accurate when using shorter time series (Figure S16) or under small amounts of noise (Figures S17 and S18). Long time series with a strong signal of non-equilibrium deterministic dynamics, such as the rocky intertidal or plankton community investigated here (Benincà et al., 2009, 2015), are examples of ideal data sets to apply our approaches. Thus, even if small perturbations are continually impacting the community (e.g. ongoing process noise), if the attractor is not completely distorted, the S-map should be able to accurately reconstruct the time-varying Jacobian matrix required to compute species sensitivities (Cenci et al., 2019) (Figure S18). Although here we focus on small communities and small amounts of noise, future work may combine our ranking approaches with recent improvements in the S-map (e.g. regularization and multiview distance; Cenci et al., 2019; Chang et al., 2021) to detect sensitive species under more challenging settings.

Finally, we show that approaches based on linear dynamical systems that are typically used for communities close to equilibrium can also provide information for communities under non-equilibrium dynamics (Cenci & Saavedra, 2019; Ushio et al., 2018). Even though the methodology may be similar in both cases, the interpretation is completely different. For instance, whereas the linearized dynamics can be used to compute a recovery rate under equilibrium (Arnoldi et al., 2018; Medeiros et al., 2021; Strogatz, 2018), we show that they can be used to derive the time-varying expected sensitivity of different species to perturbations under non-equilibrium dynamics. In addition, we use the leading eigenvector, which has been previously employed to decompose community responses into species responses to perturbations under equilibrium dynamics (Dakos, 2018; Ghadami et al., 2020; Patterson et al., 2021; Weinans et al., 2019). Therefore, the approaches introduced here to increase our understanding of how communities and their constituent species respond to perturbations when there is no stable equilibrium. Both approaches are based on a linearization of the dynamics and, thereby, only provide an assessment of responses to small perturbations. Moreover, both approaches assume that the Jacobian matrix does not change much over the time period for which perturbations evolve. Improving our framework to deal with strong nonlinearities, fast changes in the Jacobian matrix and local oscillations due to complex eigenvalues are promising avenues for future research. As our knowledge of the impact of perturbations on a community increases, it might also be possible to incorporate biased (e.g. certain species are more impacted) or correlated (e.g. certain species are impacted in the same way) perturbation distributions into our approaches. Overall, our findings illustrate how integrating well-known results of equilibrium dynamics with data-driven methods for non-equilibrium dynamics provides a fruitful avenue for future development and new insights into the response of single species and entire communities to perturbations.

AUTHOR CONTRIBUTIONS

Lucas P. Medeiros and Serguei Saavedra designed research with inputs from Stefano Allesina, Vasilis Dakos and George Sugihara; Lucas P. Medeiros performed analyses; Serguei Saavedra supervised the study; Lucas P. Medeiros and Serguei Saavedra wrote the paper with substantial revisions from Stefano Allesina, Vasilis Dakos and George Sugihara.

ACKNOWLEDGEMENTS

CONFLICT OF INTEREST

The authors declare no competing interests.

PEER REVIEW

The peer review history for this article is available at https://publons.com/publon/10.1111/ele.14131.

DATA AVAILABILITY STATEMENT

The data and code supporting the results are archived on Github (https://github.com/lucaspdmedeiros/ranking-species-sensitivity) and Zenodo (https://doi.org/10.5281/zenodo.7120866).

ORCID

Lucas P. Medeiros 🄿 https://orcid.org/0000-0002-0320-5058
Stefano Allesina 🄿 https://orcid.org/0000-0003-0313-8374
Vasilis Dakos 🄿 https://orcid.org/0000-0001-8862-718X
George Sugihara 🄿 https://orcid.org/0000-0002-2863-6946
Serguei Saavedra 🄿 https://orcid.org/0000-0003-1768-363X

REFERENCES

Aparicio, A., Velasco-Hernández, J.X., Moog, C.H., Liu, Y.Y. & Angulo, M.T. (2021) Structure-based identification of sensor species for anticipating critical transitions. *Proceedings of the National Academy of Sciences of the United States of America*, 118, e2104732118.

Arnoldi, J.F., Bideault, A., Loreau, M. & Haegeman, B. (2018) How ecosystems recover from pulse perturbations: a theory of short-to long-term responses. *Journal of Theoretical Biology*, 436, 79–92.

Barlow, J., França, F., Gardner, T.A., Hicks, C.C., Lennox, G.D., Berenguer, E. et al. (2018) The future of hyperdiverse tropical ecosystems. *Nature*, 559, 517–526.

Bartomeus, I., Saavedra, S., Rohr, R.P. & Godoy, O. (2021) Experimental evidence of the importance of multitrophic structure for species persistence. *Proceedings of the National Academy of Sciences of the United States of America*, 118, e2023872118.

Beauchesne, D., Cazelles, K., Archambault, P., Dee, L.E. & Gravel, D. (2021) On the sensitivity of food webs to multiple stressors. *Ecology Letters*, 24, 2219–2237.

Bender, E.A., Case, T.J. & Gilpin, M.E. (1984) Perturbation experiments in community ecology: theory and practice. *Ecology*, 65, 1–13.

Benincà, E., Ballantine, B., Ellner, S.P. & Huisman, J. (2015) Species fluctuations sustained by a cyclic succession at the edge of chaos. *Proceedings of the National Academy of Sciences of the United States of America*, 112, 6389–6394.

Benincà, E., Jöhnk, K.D., Heerkloss, R. & Huisman, J. (2009) Coupled predator–prey oscillations in a chaotic food web. *Ecology Letters*, 12, 1367–1378.

Boyce, W.E., DiPrima, R.C. & Meade, D.B. (2017) *Elementary differential equations*. Hoboken, NJ: John Wiley & Sons.

Cardinale, B.J., Duffy, J.E., Gonzalez, A., Hooper, D.U., Perrings, C., Venail, P. et al. (2012) Biodiversity loss and its impact on humanity. *Nature*, 486, 59–67.

Caswell, H. (2000) *Matrix population models*, Vol. 1. Sunderland, MA: Sinauer.

Cenci, S., Medeiros, L.P., Sugihara, G. & Saavedra, S. (2020) Assessing the predictability of nonlinear dynamics under smooth parameter changes. *Journal of the Royal Society Interface*, 17, 20190627.

Cenci, S. & Saavedra, S. (2019) Non-parametric estimation of the structural stability of non-equilibrium community dynamics. *Nature Ecology & Evolution*, 3, 912–918.

Cenci, S., Sugihara, G. & Saavedra, S. (2019) Regularized s-map for inference and forecasting with noisy ecological time series. *Methods in Ecology and Evolution*, 10, 650–660.

Chang, C.W., Miki, T., Ushio, M., Ke, P.J., Lu, H.P., Shiah, F.K. et al. (2021) Reconstructing large interaction networks from empirical time series data. *Ecology Letters*, 24, 2763–2774.

Clark, A.T., Arnoldi, J.F., Zelnik, Y.R., Barabas, G., Hodapp, D., Karakoç, C. et al. (2021) General statistical scaling laws for stability in ecological systems. *Ecology Letters*, 24, 1474–1486.

Clark, T. & Luis, A.D. (2020) Nonlinear population dynamics are ubiquitous in animals. *Nature Ecology & Evolution*, 4, 75–81.

Dakos, V. (2018) Identifying best-indicator species for abrupt transitions in multispecies communities. *Ecological Indicators*, 94, 494–502.

Deyle, E.R., May, R.M., Munch, S.B. & Sugihara, G. (2016) Tracking and forecasting ecosystem interactions in real time. *Proceedings of the Royal Society B: Biological Sciences*, 283, 20152258.

Dietze, M.C. (2017) *Ecological forecasting*. Princeton, NJ: Princeton University Press.

Dirzo, R., Young, H.S., Galetti, M., Ceballos, G., Isaac, N.J. & Collen, B. (2014) Defaunation in the anthropocene. *Science*, 345, 401–406.

Domínguez-García, V., Dakos, V. & Kéfi, S. (2019) Unveiling dimensions of stability in complex ecological networks. *Proceedings of the National Academy of Sciences of the United States of America*, 116, 25714–25720.

Eckmann, J.P. & Ruelle, D. (1985) Ergodic theory of chaos and strange attractors. In: Hunt, B.R., Li, T.Y., Kennedy, J.A. & Nusse, H.E. (Eds.) *The theory of chaotic attractors*. New York, NY: Springer, pp. 273–312.

Estes, J.A., Terborgh, J., Brashares, J.S., Power, M.E., Berger, J., Bond, W.J. et al. (2011) Trophic downgrading of planet earth. *Science*, 333, 301–306.

Ghadami, A., Chen, S. & Epureanu, B.I. (2020) Data-driven identification of reliable sensor species to predict regime shifts in ecological networks. *Royal Society Open Science*, 7, 200896.

Hastings, A., Abbott, K.C., Cuddington, K., Francis, T., Gellner, G., Lai, Y.C. et al. (2018) Transient phenomena in ecology. *Science*, 361, eaat6412.

Hastings, A. & Powell, T. (1991) Chaos in a three-species food chain. *Ecology*, 72, 896–903.

Ives, A.R., Gross, K. & Klug, J.L. (1999) Stability and variability in competitive communities. *Science*, 286, 542–544.

Jackson, J.B., Kirby, M.X., Berger, W.H., Bjorndal, K.A., Botsford, L.W., Bourque, B.J. et al. (2001) Historical overfishing and the recent collapse of coastal ecosystems. *Science*, 293, 629–637.

James, G., Witten, D., Hastie, T. & Tibshirani, R. (2021) *An introduction to statistical learning: with applications in R*. New York, NY: Springer.

Kéfi, S., Domnguez-Garca, V., Donohue, I., Fontaine, C., Thébault, E. & Dakos, V. (2019) Advancing our understanding of ecological stability. *Ecology Letters*, 22, 1349–1356.

Krebs, C.J., Boutin, S., Boonstra, R., Sinclair, A., Smith, J., Dale, M.R. et al. (1995) Impact of food and predation on the snowshoe hare cycle. *Science*, 269, 1112–1115.

Kuptsov, P.V. & Parlitz, U. (2012) Theory and computation of covariant lyapunov vectors. *Journal of Nonlinear Science*, 22, 727–762.

Lever, J.J., van de Leemput, I.A., Weinans, E., Quax, R., Dakos, V., van Nes, E.H. et al. (2020) Foreseeing the future of mutualistic communities beyond collapse. *Ecology Letters*, 23, 2–15.

Levin, S.A. & Lubchenco, J. (2008) Resilience, robustness, and marine ecosystem-based management. *BioScience*, 58, 27–32.

Mace, G.M., Collar, N.J., Gaston, K.J., Hilton-Taylor, C., Akçakaya, H.R., Leader-Williams, N. et al. (2008) Quantification of extinction risk: IUCN's system for classifying threatened species. *Conservation Biology*, 22, 1424–1442.

Mease, K., Bharadwaj, S. & Iravanchy, S. (2003) Timescale analysis for nonlinear dynamical systems. *Journal of Guidance, Control, and Dynamics*, 26, 318–330.

Medeiros, L.P., Song, C. & Saavedra, S. (2021) Merging dynamical and structural indicators to measure resilience in multispecies systems. *Journal of Animal Ecology*, 90, 2027–2040.

Morris, W.F. & Doak, D.F. (2002) *Quantitative conservation biology*. Sunderland, MA: Sinauer.

Patterson, A.C., Strang, A.G. & Abbott, K.C. (2021) When and where we can expect to see early warning signals in multispecies systems approaching tipping points: insights from theory. *The American Naturalist*, 198, E12–E26.

Pennekamp, F., Iles, A.C., Garland, J., Brennan, G., Brose, U., Gaedke, U. et al. (2019) The intrinsic predictability of ecological time series and its potential to guide forecasting. *Ecological Monographs*, 89, e01359.

Perretti, C.T., Munch, S.B. & Sugihara, G. (2013) Model-free forecasting outperforms the correct mechanistic model for simulated

and experimental data. *Proceedings of the National Academy of Sciences of the United States of America*, 110, 5253–5257.

Rinaldi, S. & Scheffer, M. (2000) Geometric analysis of ecological models with slow and fast processes. *Ecosystems*, 3, 507–521.

Rogers, T.L., Johnson, B.J. & Munch, S.B. (2022) Chaos is not rare in natural ecosystems. *Nature Ecology & Evolution*, 6, 1–7.

Saavedra, S., Stouffer, D.B., Uzzi, B. & Bascompte, J. (2011) Strong contributors to network persistence are the most vulnerable to extinction. *Nature*, 478, 233–235.

Song, C. & Saavedra, S. (2021) Bridging parametric and nonparametric measures of species interactions unveils new insights of non-equilibrium dynamics. *Oikos*, 130, 1027–1034.

Strogatz, S.H. (2018) *Nonlinear dynamics and chaos: with applications to physics, biology, chemistry, and engineering.* Boulder, CO: Westview Press.

Sugihara, G. (1994) Nonlinear forecasting for the classification of natural time series. *Philosophical Transactions of the Royal Society of London. Series A: Physical and Engineering Sciences*, 348, 477–495.

Turner, M.G., Dale, V.H. & Everham, E.H. (1997) Fires, hurricanes, and volcanoes: comparing large disturbances. *BioScience*, 47, 758–768.

Ushio, M., Hsieh, C.H., Masuda, R., Deyle, E.R., Ye, H., Chang, C.W. et al. (2018) Fluctuating interaction network and time-varying stability of a natural fish community. *Nature*, 554, 360–363.

Vallejo, J.C., Sanjuan, M.A. & Sanjuán, M.A. (2017) *Predictability of chaotic dynamics.* Cham, Switzerland: Springer.

Weinans, E., Lever, J.J., Bathiany, S., Quax, R., Bascompte, J., Van Nes, E.H. et al. (2019) Finding the direction of lowest resilience in multivariate complex systems. *Journal of the Royal Society Interface*, 16, 20190629.

SUPPORTING INFORMATION

Additional supporting information can be found online in the Supporting Information section at the end of this article.

Supporting Information

Ranking species based on sensitivity to perturbations under non-equilibrium community dynamics

Lucas P. Medeiros[1,2], Stefano Allesina[3,4], Vasilis Dakos[5],
George Sugihara[6] and Serguei Saavedra[1]

[1] Department of Civil and Environmental Engineering, Massachusetts Institute of Technology,
Cambridge, MA, USA
[2] Institute of Marine Sciences, University of California Santa Cruz, Santa Cruz, CA, USA
[3] Department of Ecology & Evolution, University of Chicago, Chicago, IL, USA
[4] Northwestern Institute on Complex Systems, Northwestern University, Evanston, IL, USA
[5] Institut des Sciences de l'Evolution de Montpellier, Université de Montpellier, Montpellier, France
[6] Scripps Institution of Oceanography, University of California San Diego, La Jolla, CA, USA

Contents

1 Derivation of the dynamics of small perturbations

In this section, we provide a derivation of the linear dynamics of small perturbations, which is the foundation of our approaches to rank species sensitivities to perturbations. Let us consider the most general form of a population dynamics model for a given species i within a community with S species (Case, 2000):

$$\frac{dN_i}{dt} = f_i(\mathbf{N}), \tag{S1}$$

where N_i is the abundance of species i, $\mathbf{N} = [N_1, ..., N_S]^\top$ is the vector of abundances of all species, and f_i ($f_i \colon \mathbb{R}^S \to \mathbb{R}$) is the function describing how the growth rate of species i depends on the abundances of all species. Note that f_i also depends on a set of parameters, which we consider to be fixed over time. We can write equation (S1) for all species in the community as $\frac{d\mathbf{N}}{dt} = \mathbf{f}(\mathbf{N})$, where $\frac{d\mathbf{N}}{dt} = [\frac{dN_1}{dt}, ..., \frac{dN_S}{dt}]^\top$ and $\mathbf{f} \colon \mathbb{R}^S \to \mathbb{R}^S$. See below (*Section 3*) for some examples of population dynamics models of this form.

In this study, we are interested in ranking species according to their sensitivity to perturbations, that is, how much their abundance trajectories are expected to change after some time following a small random wiggle on abundances. Then, let us consider a random pulse perturbation $\mathbf{p}$ that changes $\mathbf{N}$ into $\tilde{\mathbf{N}}$ (i.e., $\tilde{\mathbf{N}} = \mathbf{N} + \mathbf{p}$). Now, we can write the Taylor expansion of $\frac{d\tilde{\mathbf{N}}}{dt}$ around $\mathbf{N}$ (Strogatz, 2018):

$$\frac{d\tilde{\mathbf{N}}}{dt} = \mathbf{f}(\mathbf{N}) + \frac{\partial \mathbf{f}}{\partial \tilde{\mathbf{N}}}\Big|_{\tilde{\mathbf{N}}=\mathbf{N}} \cdot (\tilde{\mathbf{N}} - \mathbf{N}) + O(\mathbf{p}^\top \mathbf{p}), \tag{S2}$$

where $\frac{\partial \mathbf{f}}{\partial \mathbf{N}} = \mathbf{J}$ is the Jacobian matrix of partial derivatives with $j_{ij} = \frac{\partial f_i}{\partial N_j}$. If $\mathbf{p}$ is small, we can approximate its dynamics by taking just the linear term (i.e., ignoring higher-order terms):

$$
\begin{aligned}
\frac{d\tilde{\mathbf{N}}}{dt} &= \mathbf{f}(\mathbf{N}) + \frac{\partial \mathbf{f}}{\partial \tilde{\mathbf{N}}}\Big|_{\tilde{\mathbf{N}}=\mathbf{N}} \cdot (\tilde{\mathbf{N}} - \mathbf{N}) \\
\frac{d\mathbf{N}}{dt} + \frac{d\mathbf{p}}{dt} &= \frac{d\mathbf{N}}{dt} + \mathbf{J}|_{\tilde{\mathbf{N}}=\mathbf{N}} \cdot \mathbf{p} \\
\frac{d\mathbf{p}}{dt} &= \mathbf{J}|_{\tilde{\mathbf{N}}=\mathbf{N}} \cdot \mathbf{p}.
\end{aligned}
\tag{S3}
$$

Thus, as it is known (Boyce *et al.*, 2017, Kuptsov & Parlitz, 2012, Mease *et al.*, 2003, Strogatz, 2018, Vallejo *et al.*, 2017), the dynamics of a small perturbation $\mathbf{p}$ can be approximated by the linear equation above called the tangent dynamics of $\frac{d\mathbf{N}}{dt}$. Note that we have not assumed the existence of an equilibrium here (i.e., $\mathbf{N}^*$ for which $\mathbf{f}(\mathbf{N}^*) = \mathbf{0}$) and, therefore, equation (S3) is valid irrespective of whether $\mathbf{N}$ is close to equilibrium or not.

2 Derivation of analytical expected sensitivity

Here we derive the expected value ($\mathbb{E}(s_i)$; Box 1 in the main text) of the sensitivity s_i (equation (1) in the main text) of species i to small perturbations ($\mathbf{p}$) affecting species abundances ($\mathbf{N}$). We assume that $\mathbf{p}(t)$ follows a distribution with mean zero and covariance matrix $\boldsymbol{\Sigma}_t$. We

assume a distribution with mean zero because unbiased perturbations are the most uninformative way to consider how perturbations may impact a community. In most of our perturbation analyses, we assume that $\mathbf{p}(t)$ follows a multivariate normal distribution (i.e., $\mathbf{p}(t) \sim \mathcal{N}(\mathbf{0}, \mathbf{\Sigma}_t)$), but this assumption is not necessary for the derivation below. The linearized dynamics of a small perturbation is given by $\frac{d\mathbf{p}}{dt} = \mathbf{J}\mathbf{p}$ (see *Section 1*) (Boyce *et al.*, 2017, Eckmann & Ruelle, 1985, Mease *et al.*, 2003, Strogatz, 2018). We can obtain the solution for this linear system as $\mathbf{p}(t + k) = e^{\mathbf{J}k}\mathbf{p}(t)$, where $e^{\mathbf{A}} = \sum_{i=1}^{\infty} \frac{1}{i!}\mathbf{A}^i$ is the exponential of matrix $\mathbf{A}$ (Arnoldi *et al.*, 2018, Boyce *et al.*, 2017). By defining $\mathbf{M} = e^{\mathbf{J}k}$, we can compute the expected value of $\mathbf{p}(t + k)$:

$$\mathbb{E}[\mathbf{p}(t + k)] = \mathbb{E}[\mathbf{M}\mathbf{p}(t)]$$
$$= \mathbf{M}\mathbb{E}[\mathbf{p}(t)]$$
$$= \mathbf{0}. \tag{S4}$$

Thus, $\mathbf{p}(t + k)$ also follows a distribution with mean zero. In the special case where $\mathbf{p}(t)$ follows a normal distribution, $\mathbf{p}(t + k)$ also follows a normal distribution because $\mathbf{M}\mathbf{p}(t)$ is a weighted sum of normal distributions.

Because $p_i(t)$ and $p_i(t + k)$ have mean zero, the sensitivity of species i can be approximated by the ratio of the variance of $p_i(t + k)$ and the variance of $p_i(t)$:

$$\langle s_i \rangle = \frac{\frac{1}{n}\sum_{j=1}^{n} p_i^{(j)}(t + k)^2}{\frac{1}{n}\sum_{j=1}^{n} p_i^{(j)}(t)^2} = \frac{\mathrm{Var}[p_i(t + k)]}{\mathrm{Var}[p_i(t)]}, \tag{S5}$$

where n is the number of random perturbations and $\mathrm{Var}[p_i(t)] = \sigma_{i,t}^2$ is the ith diagonal element of $\mathbf{\Sigma}_t$. Assuming that $\sigma_{i,t}^2$ is the same for every species i, we can ignore it for the purpose of ranking species sensitivities and focus only on $\mathrm{Var}[p_i(t + k)]$. We can obtain $\mathrm{Var}[p_i(t + k)]$ by computing the covariance matrix of $\mathbf{p}(t + k)$:

$$\mathbf{\Sigma}_{t+k} = \mathbb{E}[\mathbf{p}(t + k)\mathbf{p}(t + k)^\top]$$
$$= \mathbb{E}[(\mathbf{M}\mathbf{p}(t))(\mathbf{M}\mathbf{p}(t))^\top]$$
$$= \mathbf{M}\mathbb{E}[\mathbf{p}(t)\mathbf{p}(t)^\top]\mathbf{M}^\top$$
$$= \mathbf{M}\mathbf{\Sigma}_t\mathbf{M}^\top. \tag{S6}$$

Therefore, we define the expected sensitivity of species i at time t as: $\mathbb{E}(s_i) = \mathrm{Var}[p_i(t + k)] = \sigma_{i,t+k}^2$, where $\sigma_{i,t+k}^2$ is the ith diagonal element of $\mathbf{\Sigma}_{t+k}$. Note that we can normalize $\mathbb{E}(s_i)$ by dividing it by $\sum_{i=1}^{S} \sigma_{i,t+k}^2$, which has been shown to correspond to the expected magnitude of $\mathbf{p}(t+k)$ (i.e., $\mathbb{E}[||\mathbf{p}(t+k)||^2]$) (Arnoldi *et al.*, 2018). Although this normalization does not change the order of $\mathbb{E}(s_i)$ values, it allows us to interpret the normalized $\mathbb{E}(s_i)$ as the relative contribution of species i to the expected magnitude of $\mathbf{p}(t+k)$.

In addition to knowing $\mathbf{J}$, knowledge of $\mathbf{\Sigma}_t$ and k is required to compute $\mathbb{E}(s_i)$. In our main set of perturbation analyses, we compute $\mathbb{E}(s_i)$ using the true value of k used to evolve perturbed

abundances but do not use the true value of $\mathbf{\Sigma}_t$. Specifically, we set $\mathbf{\Sigma}_t = \mathbf{I}$, where $\mathbf{I}$ is the identity matrix. We test the robustness of the expected sensitivity ranking under uncertainty in k and $\mathbf{\Sigma}_t$ in three different ways. First, we compute $\mathbb{E}(s_i)$ using $\mathbf{\Sigma}_t = \mathbf{I}$ when $\sigma_{i,t}^2$ varies over time and across species (i.e., normally distributed perturbations with a variance proportional to relative species abundances; Fig. S10). Second, we compute $\mathbb{E}(s_i)$ using $k = 1$ when k varies over time (i.e., k inversely proportional to the local rate of change of the dynamics; Fig. S13). Third, we compute $\mathbb{E}(s_i)$ as described above for our main set of analyses but add 100% of normally distributed noise to $\mathbf{\Sigma}_t$ and k at each point in time (Fig. S14).

3   Synthetic time series from population dynamics models

To test whether expected sensitivities ($\mathbb{E}(s_i)$; Box 1 in the main text) and species alignments with the leading eigenvector ($|\mathbf{v}_{1i}|$; Box 2 in the main text) can accurately rank species sensitivities to perturbations ($\langle s_i \rangle$, equation (2) in the main text), we perform perturbation analyses using synthetic time series. We generate synthetic time series using five different population dynamics models with the generic form: $\frac{d\mathbf{N}}{dt} = \mathbf{f}(\mathbf{N})$, where $\mathbf{f} \colon \mathbb{R}^S \to \mathbb{R}^S$ is a nonlinear function. Here, we present the equations, parameter values and references for each model.

The first model contains two species and depicts the interactions between a predator (species 1) and its prey (species 2), producing a limit cycle (Yodzis, 1989) (Fig. S5):

$$
\begin{aligned}
\frac{dN_1}{dt} &= kN_1\Big(\frac{aN_2^2}{1+ahN_2^2}\Big) - dN_1 \\
\frac{dN_2}{dt} &= rN_2\Big(1 - \frac{N_2}{K}\Big) - N_1\Big(\frac{aN_2^2}{1+ahN_2^2}\Big),
\end{aligned}
\tag{S7}
$$

where $k = 0.5$ $a = 0.002$, $h = 4$, $d = 0.1$ $r = 0.5$, and $K = 100$.

The second model contains three species and depicts a food chain with a primary producer (species 1), a primary consumer (species 2), and a secondary consumer (species 3), producing chaotic dynamics (Hastings & Powell, 1991, Upadhyay, 2000) (Fig. 1 in the main text and Fig. S5):

$$
\begin{aligned}
\frac{dN_1}{dt} &= rN_1\Big(1 - \frac{N_1}{K}\Big) - \frac{a_1 N_1 N_2}{1 + b_1 N_1} \\
\frac{dN_2}{dt} &= -sN_2 + hN_1 N_2 - \frac{a_2 N_2 N_3}{1 + b_2 N_2} \\
\frac{dN_3}{dt} &= -lN_3 + nN_2 N_3,
\end{aligned}
\tag{S8}
$$

where $r = 4.3$, $K = 50$, $a_1 = 0.1$, $b_1 = 0.1$, $a_2 = 0.1$, $b_2 = 0.1$, $s = 1$, $h = 0.05$, $l = 1$, and $n = 0.03$.

The third and fourth models have the general form of the classic Lotka-Volterra model (Case,

4

2000):

$$\frac{dN_i}{dt} = N_i\left(r_i + \sum_{j=1}^{S} a_{ij}N_j\right) \tag{S9}$$

where r_i is an element of the vector $\mathbf{r}$ representing the intrinsic growth rate of species i and a_{ij} is an element of the interaction matrix $\mathbf{A}$ representing the interaction effect of species j on species i. The third model contains three species ($S = 3$) and produces chaotic dynamics between two prey and one predator (Gilpin, 1979) (Fig. S5) with the following values for r_i and a_{ij}:

$$\mathbf{r} = \begin{bmatrix} 1 \\ 1 \\ -1 \end{bmatrix}, \mathbf{A} = \begin{bmatrix} -0.1 & -0.1 & -1 \\ -0.15 & -0.1 & -0.1 \\ 0.5 & 0.05 & 0 \end{bmatrix}$$

The fourth model contains four competitor species ($S = 4$) and also produces chaotic dynamics (Vano $et\ al.$, 2006) (Fig. S5) with the following values for r_i and a_{ij}:

$$\mathbf{r} = \begin{bmatrix} 1 \\ 0.72 \\ 1.53 \\ 1.27 \end{bmatrix}, \mathbf{A} = \begin{bmatrix} -1 & -1.09 & -1.52 & 0 \\ 0 & -1 & -0.44 & -1.36 \\ -2.33 & 0 & -1 & -0.47 \\ -1.21 & -0.51 & -0.35 & -1 \end{bmatrix}$$

Finally, the fifth model depicts a 5-species food web with two secondary consumers (species 1 and 2), two primary consumers (species 3 and 4), and one primary producer (species 5) also generating chaotic dynamics (Deyle $et\ al.$, 2016) (Fig. S5):

$$\begin{aligned}
\frac{dN_1}{dt} &= \nu_1\lambda_1\frac{N_1 N_3}{N_3 + N_3^*} - \nu_1 N_1 \\
\frac{dN_2}{dt} &= \nu_2\lambda_2\frac{N_2 N_4}{N_4 + N_4^*} - \nu_2 N_2 \\
\frac{dN_3}{dt} &= \mu_1\kappa_1\frac{N_3 N_5}{N_5 + N_5^*} - \nu_1\lambda_1\frac{N_1 N_3}{N_3 + N_3^*} - \mu_1 N_3 \\
\frac{dN_4}{dt} &= \mu_2\kappa_2\frac{N_4 N_5}{N_5 + N_5^*} - \nu_2\lambda_2\frac{N_2 N_4}{N_4 + N_4^*} - \mu_2 N_4 \\
\frac{dN_5}{dt} &= N_5\left(1 - \frac{N_5}{K}\right) - \mu_1\kappa_1\frac{N_3 N_5}{N_5 + N_5^*} - \mu_2\kappa_2\frac{N_4 N_5}{N_5 + N_5^*},
\end{aligned} \tag{S10}$$

where $\nu_1 = 0.1$, $\nu_2 = 0.07$, $\lambda_1 = 3.2$, $\lambda_2 = 2.9$, $N_3^* = 0.5$, $N_4^* = 0.5$, $\mu_1 = 0.15$, $\mu_2 = 0.15$, $\kappa_1 = 2.5$, $\kappa_2 = 2$, $N_5^* = 0.3$, and $K = 1.2$.

For each model, we numerically integrate the dynamics using a Runge-Kutta method with a time step of 0.05 and obtain a time series with 10,000 points. Then, we sample equidistant points obtaining a final multivariate time series with 500 points ($\{\mathbf{N}(t)\}$, $t = 1, ..., 500$). Note that with this protocol we obtain time series that fully sample the attractor of each model and have a size

similar to the empirical time series used here (Fig. S5). Also note that by sampling equidistant
points we test the robustness of the S-map to infer $\mathbb{E}(s_i)$ and $|\mathbf{v}_{1i}|$ under the typical low sampling
frequency of empirical time series.

4 Perturbation analyses

For each synthetic time series, we perform random perturbations on abundances to compute
species sensitivities ($\langle s_i \rangle$; equation (2) in the main text). We apply $n = 300$ random pulse
perturbations $\mathbf{p}$ to the abundance vector $\mathbf{N}$ at each point in time: $\tilde{\mathbf{N}} = \mathbf{N} + \mathbf{p}$. We perform these
perturbations in three different ways. First, we assume perturbations are normally distributed
around $\mathbf{N}$ and use $p_i(t) \sim \mathcal{N}(\mu = 0, \sigma^2 = r^2)$ (Fig. 1c, d in the main text). Second, we
assume perturbations are uniformly distributed around $\mathbf{N}$ and apply $\mathbf{p}(t)$ such that $\tilde{\mathbf{N}}$ is uniformly
distributed inside a hypersphere of radius r centered in $\mathbf{N}$. Third, we assume normally distributed
perturbations with a variance proportional to relative species abundances, such that: $p_i(t) \sim$
$\mathcal{N}(\mu = 0, \sigma^2 = N_i'(t)r^2)$, where $N_i'(t) = \frac{N_i(t)}{\sum_{i=1}^{S} N_i(t)}$. Note that in this last scenario we relax
our assumption that the variance of $p_i(t)$ is fixed over time and equal for every species. For all
types of perturbation, we set r to be 15% of the mean standard deviation of species abundances:
$r = 0.15 \frac{1}{S} \sum_{i=1}^{S} \sigma_{N_i}$, where σ_{N_i} is the standard deviation of N_i for the whole time series. The
results for normally distributed perturbations are presented in the main text (Fig. 3), whereas
the results for the other perturbation types are shown in Figs. S9 and S10.

After applying perturbations, we numerically integrate model $\mathbf{f}$ for k time steps using each
perturbed abundance vector $\tilde{\mathbf{N}}$ as well as the unperturbed abundance vector $\mathbf{N}$ as initial condi-
tions. Then, we compute $\langle s_i \rangle$ using the initial (i.e., time t) and final (i.e., time $t + k$) perturbed
and unperturbed abundances (equation (2) in the main text). Because $\frac{d\mathbf{N}}{dt}$ (i.e., local rate of
change) can greatly vary across state space, impacting how perturbations grow over time, we set
k to be inversely proportional to the mean absolute percent change between $N_i(t+1)$ and $N_i(t)$.
Specifically, we use $k = \left[\frac{1}{S} \sum_{i=1}^{S} \left| \frac{N_i(t+1) - N_i(t)}{N_i(t)} \right| \right]^{-\frac{1}{2}}$. Thus, k increases as the percent change
decreases and we use a square root to damp the large variability in local rate of change found
for most models. We also perform these analyses using a fixed value of k ($k = 1$ or $k = 3$) for
all points in the time series (Figs. S11 and S12). Note that $k = 3$ can be considered a long time
period for some models, allowing us to test the robustness of our approaches for longer periods
of time.

5 Inference of Jacobian matrix with the S-map

We perform the S-map using the `rEDM` package in R to sequentially infer the Jacobian matrix
($\mathbf{J}$) through time using only past time-series data in order to compute expected sensitivities ($\mathbb{E}(s_i)$)
and species alignments with the leading eigenvector ($|\mathbf{v}_{1i}|$). The S-map is a locally weighted state-
space regression method that can be used to infer the time-varying Jacobian matrix of a dynamical
system (Cenci *et al.*, 2019, Deyle *et al.*, 2016, Sugihara, 1994). Given a time series ($\{\mathbf{N}(t)\}$,

$t = 1, ..., T$), we can fit a linear regression of the following form: $N_i(t+1) = c_{i0} + \sum_{j=1}^{S} c_{ij} N_j(t)$. Note that $c_{ij} = \frac{\partial N_i(t+1)}{\partial N_j(t)}$ is a discrete-time approximation of the Jacobian matrix element j_{ij}. The S-map consists of performing this linear regression locally for a given target point $\mathbf{N}(t^*)$ by giving a stronger weight to points that are closer to it in state space. This is done by finding a solution for $\mathbf{c}$ in $\mathbf{b} = \mathbf{Ac}$, where $b_t = w_t N_i(t+1)$, $a_{tj} = w_t N_j(t)$, $w_t = \exp\left[-\theta \frac{||\mathbf{N}(t) - \mathbf{N}(t^*)||}{\overline{d}}\right]$, and $\overline{d} = \frac{1}{T} \sum_{t=1}^{T} ||\mathbf{N}(t) - \mathbf{N}(t^*)||$. Thus, $\mathbf{b} \in \mathbb{R}^T$ contains the abundances at $t+1$ weighted by the relative distance of each point to the target point, $\mathbf{A} \in \mathbb{R}^{T \times (S+1)}$ is the weighted data matrix of abundances at t, and $\mathbf{c} \in \mathbb{R}^{S+1}$ estimates the ith row of the Jacobian matrix at $\mathbf{N}(t^*)$ as well as an intercept term. We obtain the solution for $\mathbf{c}$ via singular value decomposition (Deyle *et al.*, 2016), which is equivalent to the ordinary least squares solution (Cenci *et al.*, 2019). Importantly, the parameter θ tunes how strongly the regression is localized around the target point and is typically selected via abundance predictions with leave-one-out cross-validation (LOOCV) (Cenci *et al.*, 2019).

For each of the five synthetic time series, we fit the S-map sequentially to infer $\mathbf{J}$ for each point in time, which is then used to compute $\mathbb{E}(s_i)$ and $|\mathbf{v}_{1i}|$. To do so, we assign half of the time series (i.e., $\{\mathbf{N}(t)\}$, $t = 1, ..., 250$) as a training set to select the optimal θ ($\hat{\theta}$) via LOOCV by using the S-map to predict species abundances (Cenci *et al.*, 2019). Then, we use $\hat{\theta}$ to fit the S-map over the whole training set and infer $\mathbb{E}(s_i)$ and $|\mathbf{v}_{1i}|$ at the last point in the training set (i.e., $t = 250$) to rank $\langle s_i \rangle$ values (computed via the perturbation analyses). Next, we add a new point to the training set, remove its first point, and repeat the LOOCV and ranking procedures until the end of the time series. Note that we keep the size of the training set fixed after each update (e.g., $t = 2, ..., 251$ for the first update), controlling for the effects of time series length on the performance of the S-map. Also note that we can only infer the coefficients of $\mathbf{J}$ up to a constant (Cenci & Saavedra, 2019), so we only consider the direction of the leading eigenvector ($\mathbf{v}_1$) and the relative value of the leading eigenvalue (λ_1) through time.

Recent improvements of the S-map have been developed to deal with observational and process noise as well as with communities with a large number of species (Cenci *et al.*, 2019, Chang *et al.*, 2021). Here, we find that the classic S-map as described above (Deyle *et al.*, 2016, Sugihara, 1994) already provides a very good inference of expected sensitivities ($\mathbb{E}(s_i)$; Box 1 in the main text) and eigenvector alignments ($|\mathbf{v}_{1i}|$; Box 2 in the main text). In addition to the performance shown in Fig. 3, we show that the classic S-map allows us to accurately predict the order of species sensitivities ($\langle s_i \rangle$) when normalizing species abundances (Fig. S15), when using shorter time series (Fig. S16), when adding observational noise to the time series (Fig. S17), or when the model has a stochastic component (i.e., process noise; Fig. S18). Our analyses with short and noisy time series are described in the next section (see *Section 6*). We believe that combining our ranking approaches with recent developments of the S-map (Cenci *et al.*, 2019, Chang *et al.*, 2021) to deal with large amounts of noise or with communities with a large number of species is an exciting direction for future research.

6 Analyses with short and noisy synthetic time series

In our analyses with synthetic time series reported in the main text, we infer the Jacobian matrix ($\mathbf{J}$) and, therefore, expected sensitivities ($\mathbb{E}(s_i)$) and eigenvector alignments ($|\mathbf{v}_{1i}|$) using time series with 250 points and without noise. These conditions, however, are rarely observed in empirical time series, which are typically much shorter and contaminated with noise (Cenci *et al.*, 2019, Sugihara, 1994). In this section, we describe additional analyses with short and noisy synthetic time series.

To test the robustness of our ranking approaches (i.e., using $\mathbb{E}(s_i)$ or $|\mathbf{v}_{1i}|$ to rank $\langle s_i \rangle$ over time) with shorter time series, we perform the S-map using a smaller training set. Instead of using 250 points (e.g., $t = 1, ..., 250$ in the first training set) as described in the previous section, we use only 100 points (e.g., $t = 1, ..., 100$ in the first training set) to train the S-map and infer $\mathbb{E}(s_i)$ and $|\mathbf{v}_{1i}|$ at the last point in the training set to predict species sensitivities ($\langle s_i \rangle$). Fig. S16 shows that our results remain similar to the results in Fig. 3b, which use 250 points.

We also verify the performance of our ranking approaches inferred with the S-map under observational noise. To do so, we use the same synthetic time series and perturbation analyses as reported in the main text but add normally distributed noise to the time series used to train the S-map. That is, for each species i and time t in the training set, we transform $N_i(t)$ into $N_i(t) + \mathcal{N}(\mu = 0, \sigma^2 = [\delta N_i(t)]^2)$, where $\delta = 0.1$ (i.e., 10% of observational noise). Then, we use the noisy time series to infer $\mathbb{E}(s_i)$ and $|\mathbf{v}_{1i}|$ with the S-map and predict the order of $\langle s_i \rangle$ at each point in time. The middle column in Fig. S5 shows the attractors for each population dynamics model with observational noise. Fig. S17 shows that, although the mean rank correlation ($\bar{\rho}$) can decrease for some models, our results remain similar to the results in Fig. 3b, which do not contain noise.

We also perform analyses with synthetic time series with process noise. To do so, we generate synthetic time series using a modified version of our population dynamics models (equations (S7), (S8), (S9), and (S10)). In particular, we transform each deterministic population dynamics model $\frac{d\mathbf{N}}{dt} = \mathbf{f}(\mathbf{N})$ into a model with a stochastic component: $d\mathbf{N} = \mathbf{f}(\mathbf{N})dt + \mathbf{g}(\mathbf{N})dW$, where $\mathbf{f}(\mathbf{N})$ is the original deterministic part, $\mathbf{g}(\mathbf{N})$ is the stochastic part, and W is a Wiener process. We use the simplest form of stochasticity, which consists of independent process noise for each species. That is, $\mathbf{g}(\mathbf{N})$ is a diagonal matrix with $N_i\delta$ as the diagonal elements, where $\delta = 0.03$. We then use the stochastic version of the models to generate the synthetic time series but use the deterministic version (i.e., $\delta = 0$) to evolve perturbed points over time in our perturbation analyses (see *Section 4*). Finally, we inferred our ranking approaches with the S-map using the synthetic time series with process noise to predict the order of $\langle s_i \rangle$ over time. The right column in Fig. S5 shows the attractors for each population dynamics model with process noise. Fig. S18 shows that, although the mean rank correlation ($\bar{\rho}$) can decrease for some models, our results remain similar to the results in Fig. 3b.

7 Forecast analyses with empirical time series

We apply our ranking approaches to two empirical time series. Both time series contain four interacting variables (hereafter species) and have been shown to exhibit non-equilibrium dynamics for long periods of time (Beninèà *et al.*, 2015, 2009). The first time series has 251 points and reports the percentage of cover of barnacles, mussels, crustose algae, and bare rock in a pristine rocky intertidal site sampled monthly for 20 years (Beninèà *et al.*, 2015) (Fig. 4a in the main text). The second time series has 794 points and reports the abundance of picocyanobacteria, nanoflagellates, rotifers, and calanoid copepods in an experimental mesocosm sampled twice a week for 7 years (Beninèà *et al.*, 2009) (Fig. S21). Because both time series report species abundances on the same scale and unit, we do not normalize species abundances before performing the S-map in order to preserve properties of the Jacobian matrix (e.g., sign of Jacobian coefficients (Song & Saavedra, 2021); but see Fig. S25).

For each time series, we test the hypothesis that the order of species sensitivities ($\mathbb{E}(s_i)$) and species alignments with the leading eigenvector ($|\mathbf{v}_{1i}|$) should predict the order of species standardized forecast errors (ϵ_i; equation (4) in the main text). To do so, we fit the S-map to compute both rankings and use a Long Short-Term Memory (LSTM) neural network (James *et al.*, 2021) to forecast species abundances. Specifically, for each time series, we assign 70% of the data as the training set and sequentially infer the Jacobian matrix with the S-map by moving the training set forward while keeping its size fixed as described in the previous section. In addition, we independently train the LSTM neural network on the training set and forecast the abundances of all species for $\tau = 3$ steps ahead (Cenci *et al.*, 2020). Note that we normalize species abundances to mean zero and unit standard deviation before training the LSTM neural network. Then, we move the training set forward keeping its size fixed, fit the S-map and train the LSTM neural network in the new training set, and forecast abundances for $\tau = 3$ steps ahead until we reach the end of the time series. Thus, for each time t in the test set (i.e., last 30% of points in the time series), we obtain $\mathbb{E}(s_i)$, $|\mathbf{v}_{1i}|$ and ϵ_i for each species and compute the rank correlation ρ between them. Note that neither the S-map nor the LSTM neural network use information from abundances outside the current training set for inference and forecasting, respectively. Finally, we perform a randomization test to verify whether the mean rank correlation over the test set ($\bar{\rho}$) is significantly greater than zero. For each empirical time series and for each ranking approach, we shuffle ϵ_i values across species for each point in the test set and compute $\bar{\rho}$ 1,000 times to obtain a *p*-value. We also perform these analyses using $\tau = 2$ (Fig. S22) as well as using 60% and 50% of points in the training set (Figs. S23 and S24).

8 Forecast analyses with synthetic time series

In the previous section, we describe our analyses using empirical time series to test the hypothesis that species showing higher forecast errors (ϵ_i) at a given time are also more sensitive to perturbations (i.e., have a higher value of $\mathbb{E}(s_i)$ or $|\mathbf{v}_{1i}|$). Here, we describe similar analyses using

the five synthetic time series generated from population dynamics models (see *Section 3*). In these analyses, we compute an average forecast error ($\bar{\epsilon}_i$) for each species by trying to forecast species abundances with the LSTM neural network under perturbations (Cenci *et al.*, 2020, James *et al.*, 2021). First, we separate a given synthetic time series into a training set (first half of the time series) and a test set (second half of the time series). Then, we add 10% of observational noise to the training set (see *Section 6*) and use it to infer the Jacobian matrix with the S-map and to forecast species abundances with the LSTM at the last point in the training set. Following the analyses of the previous section, we forecast species abundances for $\tau = 3$ steps ahead and then move the training set forward by keeping its size fixed and repeat the inference and forecast procedures until the end of the time series. For each time t in the test set, we compute an average forecast root-mean-square error (RMSE) under perturbations for each species i as:

$$\bar{\epsilon}_i = \frac{1}{n} \sum_{j=1}^{n} \sqrt{[\tilde{N}_i^{(j)}(t + \tau - 1) - \hat{N}_i(t + \tau - 1)]^2}, \tag{S11}$$

where n is the number of perturbed abundances ($n = 300$), $\tilde{N}_i^{(j)}(t + \tau - 1)$ is the jth perturbed abundance of species i at time $t + \tau - 1$, and $\hat{N}_i(t + \tau - 1)$ is the forecast of the abundance of species i at time $t + \tau - 1$. Thus, we compute the average forecast error of each species for n potential perturbed abundances that could have been observed at a given point in time. Note that perturbed abundances are obtained from our perturbation analyses (see *Section 4*).

We then use the inferred expected sensitivity ($\mathbb{E}(s_i)$) and eigenvector ($|\mathbf{v}_{1i}|$) rankings as well as our alternative indicators (i.e., $\Delta N_i(t)$ or $-N_i(t)$) to predict the order of average forecast errors ($\bar{\epsilon}_i$) over the test set. Note that this analysis follows closely our analyses of predicting the order of species sensitivities ($\langle s_i \rangle$) described in the main text. Fig. S19 shows the results for these analyses as the Spearman's rank correlation (ρ) between a given ranking ($\mathbb{E}(s_i)$, $|\mathbf{v}_{1i}|$, $\Delta N_i(t)$, or $-N_i(t)$) and $\bar{\epsilon}_i$ over the test set. The figure shows that, except for the model with 4 competitor species, $\mathbb{E}(s_i)$ and $|\mathbf{v}_{1i}|$ show, on average, a positive rank correlation with $\bar{\epsilon}_i$ (Fig. S19). Furthermore, the figure shows that this is not the case for $\Delta N_i(t)$ and $-N_i(t)$ (Fig. S19). Therefore, this analysis illustrates that species forecast errors can be related to our measures of sensitivity to perturbations under synthetic time series.

9 Leading eigenvector and direction of greatest perturbation expansion under equilibrium dynamics

We now explain how the leading eigenvector of the Jacobian matrix $\mathbf{J}$ (see *Section 1*) points in the direction of greatest expansion of small perturbations under equilibrium dynamics. Under equilibrium dynamics and for sufficiently small perturbations, $\mathbf{J}$ evaluated at the equilibrium $\mathbf{N}^*$ is constant. Thus, we can obtain the general solution of the linear differential equation (S3) as

(Boyce *et al.*, 2017, Strogatz, 2018):

$$\mathbf{p}(t+k) = \sum_{i=1}^{S} c_i e^{\lambda_i k} \mathbf{v}_i, \tag{S12}$$

where where $\mathbf{v}_i$ is the real part of the ith eigenvector of $\mathbf{J}$, λ_i is the real part of the ith eigenvalue ($\lambda_S \leq ... \leq \lambda_1$), and each c_i is a constant that depends on the initial condition $\mathbf{p}(t) = \sum_{i=1}^{S} c_i \mathbf{v}_i$. Under equilibrium dynamics, $\lambda_i < 0$ for all i implies a stable equilibrium, whereas $\lambda_i > 0$ for any i implies an unstable equilibrium (Strogatz, 2018). Note that, without loss of generality, we can set $t = 0$ for the initial condition. Also note that the solution for $\mathbf{p}(t+k)$ can only be described by equation (S12) if $\mathbf{J}$ has S distinct eigenvalues and, therefore, a set of S linearly independent eigenvectors. We propose that given a sufficient amount of time k, $e^{\lambda_1 k}$ will become much larger than subsequent terms (i.e., $e^{\lambda_2 k}, ..., e^{\lambda_S k}$) and, therefore, equation (S12) can be approximated using only the leading eigenvalue and its associated leading eigenvector:

$$\mathbf{p}(t+k) \approx c_1 e^{\lambda_1 k} \mathbf{v}_1. \tag{S13}$$

Therefore, after a sufficient time k, perturbed abundances $\mathbf{p}$ will be located closely to the line spanned by $\mathbf{v}_1$.

It is important to note that the time k required for $c_1 e^{\lambda_1 k} \mathbf{v}_1$ to approximate $\mathbf{p}(t+k)$ depends on all eigenvalues and eigenvectors. For example, if $\lambda_S < ... < \lambda_2 < 0 < \lambda_1$ and eigenvectors are orthogonal to each other, then the time k for $c_1 e^{\lambda_1 k} \mathbf{v}_1$ to approximate $\mathbf{p}(t+k)$ is expected to be small (see first scenario in *Section 13* and Fig. S1). Importantly, this is the scenario we expect to observe in chaotic non-equilibrium dynamical systems that typically have directions of expansion (i.e., unstable manifold) and contraction (i.e., stable manifold) at each point along an attractor (Eckmann & Ruelle, 1985, Strogatz, 2018). On the other hand, if more than one eigenvalue is positive or if eigenvectors are not orthogonal, then the time k for $c_1 e^{\lambda_1 k} \mathbf{v}_1$ to approximate $\mathbf{p}(t+k)$ is expected to be large (see second scenario in *Section 13* and Fig. S2).

In addition, it is also important to consider the case of complex eigenvalues and eigenvectors. In this case, the real solution approximated using only λ_1 and $\mathbf{v}_1$ is given by (Boyce *et al.*, 2017):

$$\mathbf{p}(t+k) \approx c_1 \mathbf{p}_1 + c_2 \mathbf{p}_2, \tag{S14}$$

where c_1 and c_2 are constants and $\mathbf{p}_1$ and $\mathbf{p}_2$ are the two linearly independent real solutions given by:

$$\mathbf{p}_1 = e^{ak}[\mathbf{u}\cos(bk) - \mathbf{z}\sin(bk)]$$
$$\mathbf{p}_2 = e^{ak}[\mathbf{u}\sin(bk) + \mathbf{z}\cos(bk)], \tag{S15}$$

where $\lambda_1 = a + ib$, $\lambda_2 = a - ib$ is the pair of leading complex eigenvalues and $\mathbf{v}_1 = \mathbf{u} + i\mathbf{z}$, $\mathbf{v}_2 = \mathbf{u} - i\mathbf{z}$ is the pair of leading complex eigenvectors. Thus, in this case the solution $\mathbf{p}(t+k)$ is

oscillatory. However, we can see that if the imaginary parts of the leading eigenvalue and leading eigenvector (b and $\mathbf{z}$) are small, then their real parts (a and $\mathbf{u}$) still inform us about the magnitude and direction of greatest expansion of perturbations, respectively (see third scenario in *Section 13* and Fig. S3). Finally, we note that b (and therefore $\mathbf{z}$) is zero for the majority of points in three out of five synthetic time series that we analyze (predator-prey (2 sp): 47.7%; food chain (3 sp): 69.1%; food web (3 sp): 81.6%; competitors (4 sp): 26.4%; and food web (5 sp): 95.2%). To keep a simple notation, we use λ_i and $\mathbf{v}_i$ throughout the text to refer to the real part of the ith eigenvalue and eigenvector, respectively.

10 Leading Lyapunov vector and direction of greatest perturbation expansion under non-equilibrium dynamics

In this study, we focus on non-equilibrium attractors such as limit cycles or chaotic attractors (Fig. S5). By "non-equilibrium dynamics" we refer to trajectories of a deterministic dynamical system (e.g., population dynamics model) that do not settle to a stable equilibrium point. A large literature on nonlinear dynamics has shown that local Lyapunov exponents and their associated Lyapunov vectors determine how a (hyper)sphere of small perturbations at a given state $\mathbf{N}$ deforms into a (hyper)ellipsoid after sufficient time (Eckmann & Ruelle, 1985, Kuptsov & Parlitz, 2012, Mease *et al.*, 2003, Strogatz, 2018, Vallejo *et al.*, 2017). Let l_i ($l_S \leq ... \leq l_1$) and $\mathbf{w}_i$ denote the ith local Lyapunov exponent and vector, respectively. If at time t we apply S perturbations with a small norm $||\mathbf{p}_i(t)|| = \delta$ ($i = 1, ..., S$) in the directions of $\mathbf{w}_i$ (i.e., $\frac{\mathbf{p}_i(t)}{\delta} = \mathbf{w}_i$), then after some time k, $||\mathbf{p}_i(t + k)|| \approx ||\mathbf{p}_i(t)||e^{l_i k}$ denotes the length of the ith principal axis of the ellipsoid (Kuptsov & Parlitz, 2012, Mease *et al.*, 2003, Strogatz, 2018, Vallejo *et al.*, 2017). As we have mentioned in *Section 1*, small perturbations evolve according to $\frac{d\mathbf{p}}{dt} = \mathbf{J}\mathbf{p}$. If $\mathbf{J}$ is constant through time, as is the case when it is evaluated at an equilibrium point, it has been shown that Lyapunov vectors ($\mathbf{w}_1, ..., \mathbf{w}_S$) are equivalent to the eigenvectors of $\mathbf{J}$ ($\mathbf{v}_1, ..., \mathbf{v}_S$) and Lyapunov exponents ($l_S \leq ... \leq l_1$) are equivalent to the eigenvalues of $\mathbf{J}$ ($\lambda_S \leq ... \leq \lambda_1$) (Kuptsov & Parlitz, 2012, Mease *et al.*, 2003). Nevertheless, when $\mathbf{J}$ is not constant through time, it is necessary to incorporate information on all $\mathbf{J}$ matrices along a trajectory to estimate l_i and $\mathbf{w}_i$. The problem with this approach, however, is that it requires information beyond time t in order to detect the directions of perturbation expansion/contraction at time t and therefore is not useful for real-world applications. Thus, the question is whether the leading eigenvector can be used as a proxy for the leading Lyapunov vector to detect the direction of greatest expansion of small perturbations under non-equilibrium dynamics.

Here we specify the conditions under which the leading eigenvector $\mathbf{v}_1$ is a good approximation to the leading Lyapunov vector $\mathbf{w}_1$. On the one hand, we hypothesize that when the rate of change of the system ($\frac{d\mathbf{N}}{dt}$) is large, the Jacobian matrix $\mathbf{J}$ changes rapidly and $\mathbf{v}_1$ approximates $\mathbf{w}_1$ only for a small time k. Note that, under these circumstances, only a small amount of time is required for $c_1 e^{\lambda_1 k}\mathbf{v}_1$ to approximate $\mathbf{p}(t + k)$ (equation (S13)). On the other hand, we hypothesize that

when $\frac{d\mathbf{N}}{dt}$ is small, $\mathbf{J}$ changes slowly and $\mathbf{v}_1$ approximates $\mathbf{w}_1$ for a larger time k. Note that, under this scenario, a larger amount of time is required for $c_1 e^{\lambda_1 k} \mathbf{v}_1$ to approximate $\mathbf{p}(t + k)$. Therefore, the leading eigenvector must show a higher accuracy in detecting the direction of greatest perturbation expansion when the amount of time k for which perturbations evolve is inversely proportional to the current rate of change of the system. Note that we set k to be inversely proportional to the local rate of change of the system in our main perturbation analyses (see *Section 4*; Fig. 3 in the main text), but also perform perturbation analyses using fixed values of k (see *Section 4*; Figs. S11 and S12).

To verify how well the leading eigenvector $\mathbf{v}_1$ approximates the leading Lyapunov vector $\mathbf{w}_1$, we compute $\mathbf{w}_1$ for all points along each synthetic time series (see *Section 3*). Although computing the complete set of Lyapunov vectors is a more complicated procedure (Ginelli *et al.*, 2007, Kuptsov & Parlitz, 2012), computing just $\mathbf{w}_1$ (i.e., direction of greatest perturbation expansion) is straightforward (Vallejo *et al.*, 2017). Specifically, we compute $\mathbf{w}_1$ by applying a small perturbation $\mathbf{p}$ at time t and evolving the original dynamics ($\frac{d\mathbf{N}}{dt} = \mathbf{f}(\mathbf{N})$) and the tangent dynamics ($\frac{d\mathbf{p}}{dt} = \mathbf{J}\mathbf{p}$) simultaneously for k time steps. Then, $\mathbf{p}$ will rotate over time to the direction of $\mathbf{w}_1$ while expanding at a rate given by the leading Lyapunov exponent (l_1) (Kuptsov & Parlitz, 2012, Mease *et al.*, 2003, Vallejo *et al.*, 2017). For the convergence of $\mathbf{p}$ to $\mathbf{w}_1$ to be faster, we follow standard methods (Vallejo *et al.*, 2017) and choose $\mathbf{p}$ to be a vector with a small norm r in the direction of $\mathbf{v}_1$. Specifically $\mathbf{p} = r\frac{\mathbf{v}_1}{||\mathbf{v}_1||}$, where we set r to be 5% of the mean standard deviation of species abundances: $r = 0.05\frac{1}{S}\sum_{i=1}^{S} \sigma_{N_i}$. For each point in time, we use the same value of k as used in our perturbation analyses (i.e., k is inversely proportional to the local rate of change of the dynamics as described in *Section 4*). The leading Lyapunov vector at time t can then be estimated as $\mathbf{w}_1 = \mathbf{p}(t + k)$, whereas the leading Lyapunov exponent can be calculated as $l_1 = \frac{1}{k} \log \left(\frac{||\mathbf{p}(t+k)||}{||\mathbf{p}(t)||} \right)$. To verify how aligned $\mathbf{v}_1$ is with $\mathbf{w}_1$, we compute the absolute value of the cosine of the angle between $\mathbf{v}_1$ and $\mathbf{w}_1$ at each point in time. Thus, if $\mathbf{v}_1$ indeed points in the direction of $\mathbf{w}_1$, we expect that only the magnitude and not the direction of $\mathbf{p}$ will change after k time steps. In this case, the growth rate of the magnitude of $\mathbf{p}$ is given by l_1. To benchmark the observed alignment between $\mathbf{v}_1$ and $\mathbf{w}_1$, we repeat the procedure above but choose $\mathbf{p}$ to be a vector with norm r and a random direction at each point in time. We use this analysis to compare the alignment between $\mathbf{v}_1$ and $\mathbf{w}_1$ (expected to be high) with the alignment of a randomly chosen vector $\mathbf{p}(t)$ and $\mathbf{p}(t + k)$ (expected to be low). We find $\mathbf{v}_1$ to be highly aligned with $\mathbf{w}_1$ (i.e., absolute value of cosine close to 1) for all five synthetic time series (left boxplots in Fig. S4). In contrast, when the initial perturbation ($\mathbf{p}(t)$) has a random direction instead of the direction of $\mathbf{v}_1$, we find it to be poorly aligned with $\mathbf{p}(t + k)$ (right boxplots in Fig. S4).

13

11 From direction of greatest perturbation expansion to ranking species sensitivities

Now, we show how we can rank species sensitivities based on the direction of greatest perturbation expansion approximated by the leading eigenvector. We define the sensitivity of species i to a single perturbation $\mathbf{p}$ from time t to $t+k$ as the squared difference between its perturbed and unperturbed abundance in relation to the initial squared difference caused by the perturbation (equation (1) in the main text):

$$s_i = \frac{[\tilde{N}_i(t+k) - N_i(t+k)]^2}{[\tilde{N}_i(t) - N_i(t)]^2} = \frac{p_i(t+k)^2}{p_i(t)^2}. \tag{S16}$$

Note that under equilibrium dynamics, we can just change N_i to N_i^* and the derivation below remains the same. Let us first consider the numerator of the equation above by substituting the approximated solution of the linearized dynamics (equation (S13)) into it:

$$p_i(t+k)^2 \approx [c_1 e^{\lambda_1 k} \mathbf{v}_{1i}]^2$$
$$\approx c_1^2 e^{2\lambda_1 k} \mathbf{v}_{1i}^2, \tag{S17}$$

where $\mathbf{v}_{1i}^2$ corresponds to the square of the ith element of $\mathbf{v}_1$. Thus, $c_1^2 e^{2\lambda_1 k}$ represents the total amount of expansion, which depends on λ_1, k, and c_1 via the initial condition. Note, however, that this term is the same for every species i. Therefore, the values of $p_i(t+k)^2$ across species can be ranked using $|\mathbf{v}_{1i}|$, which follows the same order as $\mathbf{v}_{1i}^2$. We use $|\mathbf{v}_{1i}|$ instead of $\mathbf{v}_{1i}^2$ because it has a clear geometric interpretation as the alignment of $\mathbf{v}_1$ with the coordinate axis corresponding to species i in state space. That is, if $||\mathbf{v}_1|| = 1$, then $|\mathbf{v}_{1i}|$ is equivalent to the absolute value of the cosine of the angle α_i between $\mathbf{v}_1$ and $\mathbf{e}_i$: $|\mathbf{v}_{1i}| = |\cos \alpha_i| = |\mathbf{v}_1 \mathbf{e}_i|$, where $\mathbf{e}_i$ is the ith standard basis vector.

So far, we have only considered species sensitivities to a single perturbation $\mathbf{p}$. We now consider multiple perturbations at time t ($\mathbf{p}(t)$), which follow a given distribution with mean zero and covariance matrix $\mathbf{\Sigma}_t$. For a set of n randomly perturbed abundances, we can define the sensitivity of species i from time t to $t+k$ as the average squared difference between a set of n randomly perturbed abundances and its unperturbed abundance in relation to the initial average squared difference (equation (2) in the main text):

$$\langle s_i \rangle = \frac{\frac{1}{n}\sum_{j=1}^{n}[\tilde{N}_i^{(j)}(t+k) - N_i(t+k)]^2}{\frac{1}{n}\sum_{j=1}^{n}[\tilde{N}_i^{(j)}(t) - N_i(t)]^2} = \frac{\frac{1}{n}\sum_{j=1}^{n}p_i^{(j)}(t+k)^2}{\frac{1}{n}\sum_{j=1}^{n}p_i^{(j)}(t)^2}. \tag{S18}$$

By focusing on the numerator, we can see that $\frac{1}{n}\sum_{j=1}^{n}p_i^{(j)}(t+k)^2 = \mathbb{E}[c_1^2 e^{2\lambda_1 k} \mathbf{v}_{1i}^2] = e^{2\lambda_1 k}\mathbf{v}_{1i}^2\mathbb{E}[c_1^2]$, since $e^{2\lambda_1 k}$ and $\mathbf{v}_{1i}^2$ are constants. The expectation $\mathbb{E}[c_1^2]$ will depend on the distribution of initial conditions, but will affect the sensitivity of all species by the same amount. Finally, we note that because $p_i(t)$ has mean zero, the denominator of equation (S18) is a constant given by the

14

variance of $p_i(t)$ (i.e., the ith diagonal element $\sigma_{i,t}^2$ of $\boldsymbol{\Sigma}_t$; *Section 2*). Thus, if $\sigma_{i,t}^2$ is the same for every species i, the denominator of equation (S18) will not affect the order of $\langle s_i \rangle$ values and we can use $|\mathbf{v}_{1i}|$ to rank species sensitivities. However, we keep this denominator in our definition of $\langle s_i \rangle$ to control for distinct variances across species in one of our perturbation analyses (see *Section 4*).

12 Connection between expected sensitivity and eigenvector approaches

Here, we show a connection between our measures of expected sensitivity ($\mathbb{E}(s_i)$; Box 1 in the main text) and alignment with the leading eigenvector ($|\mathbf{v}_{1i}|$; Box 2 in the main text) under two simplifying assumptions. First, we assume that all species are affected by perturbations with the same variance and there is no covariance among species pairs (i.e., the covariance matrix of perturbations $\boldsymbol{\Sigma}_t$ is the identity matrix $\mathbf{I}$). Second, we assume that the Jacobian matrix $\mathbf{J}$ at time t is symmetric (i.e., $\mathbf{J} = \mathbf{J}^\top$). Note that all eigenvalues of $\mathbf{J}$ are guaranteed to be real when this matrix is symmetric. Although these assumptions may not be fulfilled in natural communities, they allow us to obtain a first insight into the connections between $\mathbb{E}(s_i)$ and $|\mathbf{v}_{1i}|$. Using these assumptions, we can write the following equation for the covariance matrix of perturbations at time $t + k$ (*Section 2*):

$$
\begin{aligned}
\boldsymbol{\Sigma}_{t+k} &= e^{\mathbf{J}k} \boldsymbol{\Sigma}_t e^{\mathbf{J}^\top k} \\
&= e^{\mathbf{J}k} e^{\mathbf{J}k} \\
&= e^{\mathbf{J}k + \mathbf{J}k} \\
&= e^{\mathbf{J}2k},
\end{aligned}
\tag{S19}
$$

where $e^{\mathbf{A}}$ is the exponential of a given matrix $\mathbf{A}$ and we have used the fact that if $\mathbf{A}$ and $\mathbf{B}$ commute then $e^{\mathbf{A}} e^{\mathbf{B}} = e^{\mathbf{A}+\mathbf{B}}$. Now, we can write the eigendecomposition of $\boldsymbol{\Sigma}_{t+k}$ as:

$$
\boldsymbol{\Sigma}_{t+k} = \mathbf{V} e^{\boldsymbol{\Lambda}2k} \mathbf{V}^\top,
\tag{S20}
$$

where $\mathbf{V}$ is the matrix containing the eigenvectors of $\mathbf{J}$ ($\mathbf{v}_i$) as column vectors and $\boldsymbol{\Lambda}$ is the diagonal matrix containing the eigenvalues of $\mathbf{J}$ (λ_i). Note that we have used the property that $\mathbf{A}$ and $e^{\mathbf{A}}$ share the same eigenvectors and that if λ_i is an eigenvalue of $\mathbf{A}$, then e^{λ_i} is the corresponding eigenvalue of $e^{\mathbf{A}}$. The expected sensitivity of species i is defined as the ith diagonal element of

15

$\mathbf{\Sigma}_{t+k}$ ($\sigma^2_{i,t+k}$; *Section 2*), which gives us:

$$\mathbb{E}(s_i) = \sigma^2_{i,t+k}$$
$$= \sum_{j=1}^{S} \mathbf{v}_{ji}^2 e^{\lambda_j 2k}$$
$$\approx \mathbf{v}_{1i}^2 e^{\lambda_1 2k}, \tag{S21}$$

where $\mathbf{v}_{ji}$ is the jth element of $\mathbf{v}_i$ and in the last step we used the fact that, given a sufficient amount of time k, $e^{\lambda_1 2k}$ will become much larger than $e^{\lambda_2 2k}, ..., e^{\lambda_S 2k}$ and will dominate the expression. Thus, the order of $\mathbb{E}(s_i)$ values will follow closely the order of $|\mathbf{v}_{1i}|$ values under the assumptions considered here. Finally, note that the final expression in equation (S21) is very similar to what we obtained in equation (S17) as an explanation of how we can use $|\mathbf{v}_{1i}|$ to rank species sensitivities to a given perturbation (s_i).

13   Illustrations with Lotka-Volterra dynamics at equilibrium

To illustrate how expected sensitivities ($\mathbb{E}(s_i)$; Box 1 in the main text) and alignments with the leading eigenvector ($|\mathbf{v}_{1i}|$; Box 2 in the main text) are able to rank species according to their sensitivity to perturbations ($\langle s_i \rangle$), we use the classic Lotka-Volterra model (equation (S9)) under equilibrium dynamics. For this model, the vector of species abundances at equilibrium is given by: $\mathbf{N}^* = -\mathbf{A}^{-1}\mathbf{r}$. While the focus of our study is on non-equilibrium dynamics, our goal here is simply to show the performance of these two proposed methods under three simple scenarios of equilibrium dynamics. Our results for non-equilibrium dynamics are described in the main text.

We use three different scenarios of the Lotka-Volterra dynamics with $S = 3$ species. For all scenarios we choose a combination of $\mathbf{r}$ and $\mathbf{A}$ giving the following feasible (i.e., positive abundances for all species) equilibrium: $\mathbf{N}^* = [1, 1, 1]^\top$. Note that for this feasible equilibrium, the Jacobian matrix evaluated at $\mathbf{N}^*$ is given by: $\mathbf{J} = \text{diag}(\mathbf{N}^*)\mathbf{A} = \mathbf{A}$. For each scenario, we compute the eigenvalues (λ_i) and eigenvectors ($\mathbf{v}_i$) of $\mathbf{J}$ as well as expected sensitivities ($\mathbb{E}(s_i)$) using $k = 0.1, 0.2, 0.3, 0.4$, and 0.5. We then perform 2,000 normally distributed perturbations $\mathbf{p}$ to $\mathbf{N}^*$ (i.e., $p_i \sim \mathcal{N}(\mu = 0, \sigma^2 = r^2)$ with $r = 0.05$) and evolve each perturbed abundance over time according to equation (S9) for $k = 0.5$ time steps. Finally, we compute species sensitivities ($\langle s_i \rangle$) at $t = 0.1, 0.2, 0.3, 0.4$, and 0.5 using all perturbed abundances at those time points.

The first scenario (Fig. S1) consists of the following parameter values of the Lotka-Volterra model:

$$\mathbf{r} = \begin{bmatrix} 1 \\ 1 \\ 1 \end{bmatrix}, \mathbf{A} = \begin{bmatrix} 1 & -2 & 0 \\ 0 & -1 & 0 \\ 0 & 2 & -3 \end{bmatrix}$$

The eigenvalues of $\mathbf{J}$ show that the feasible equilibrium for this system is a saddle point: $\lambda_1 = 1$ (unstable manifold), $\lambda_2 = -1$, and $\lambda_3 = -3$ (stable manifolds). The order of expected sensitivities

16

is given by $\mathbb{E}(s_3) < \mathbb{E}(s_2) < \mathbb{E}(s_1)$, which corresponds exactly to the order of species sensitivities $(\langle s_i \rangle)$ for all times (Fig. S1b, c). The order of eigenvector alignments is given by $|\mathbf{v}_{13}|, |\mathbf{v}_{12}| < |\mathbf{v}_{11}|$ and corresponds closely to the order of species sensitivities, but cannot distinguish species 2 and 3 (Fig. S1b, c). Note that expected sensitivities depend on the time step k, whereas eigenvector alignments do not.

The second scenario (Fig. S2) consists of the following parameter values:

$$\mathbf{r} = \begin{bmatrix} -4.5 \\ 17.5 \\ 7 \end{bmatrix}, \mathbf{A} = \begin{bmatrix} 4 & 0.5 & 0 \\ 0.5 & -10 & -8 \\ 0 & -8 & 1 \end{bmatrix}$$

The eigenvalues of $\mathbf{J}$ show that the feasible equilibrium is again a saddle point: $\lambda_1 = 5.2$, $\lambda_2 = 4.0$ (unstable manifolds), and $\lambda_3 = -14.2$ (stable manifold). However, this scenario is more challenging than the previous one for our ranking approaches because there are two (instead of one) directions of perturbation expansion. The order of expected sensitivities is given by $\mathbb{E}(s_2) < \mathbb{E}(s_1) < \mathbb{E}(s_3)$, which corresponds exactly to the order of species sensitivities from $k = 0.2$ to $k = 0.5$ (Fig. S2b, c). The order of eigenvector alignments is given by $|\mathbf{v}_{11}| < |\mathbf{v}_{12}| < |\mathbf{v}_{13}|$ and provides a reasonable match to the order of species sensitivities (Fig. S2b, c).
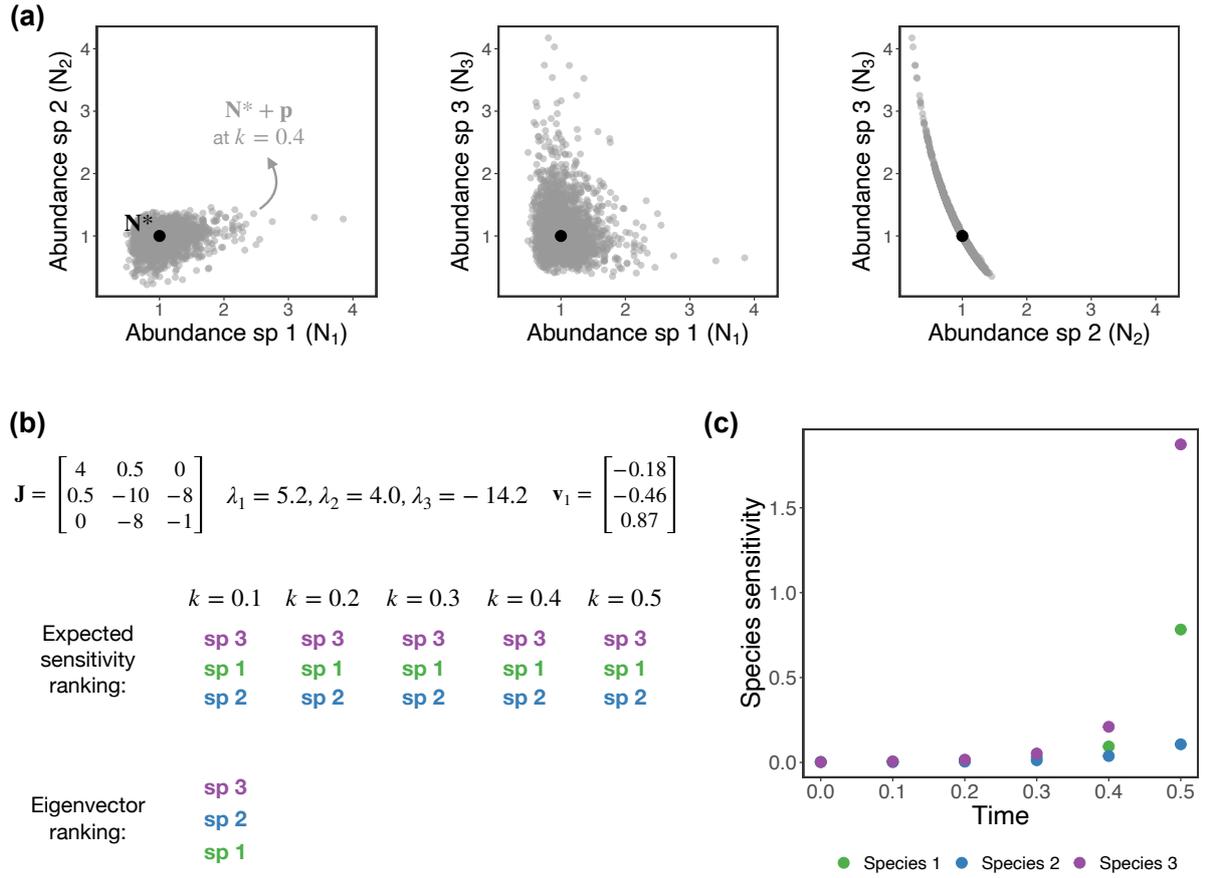
Finally, the third scenario (Fig. S3) consists of the following parameter values:

$$\mathbf{r} = \begin{bmatrix} 5 \\ -1 \\ -7 \end{bmatrix}, \mathbf{A} = \begin{bmatrix} -4 & -3 & 2 \\ -2 & 1 & 2 \\ 5 & 2 & 0 \end{bmatrix}$$

For this scenario, the leading eigenvalue of $\mathbf{J}$ is complex and therefore indicate oscillatory dynamics: $\lambda_1 = 2.0 + 0.7i$, $\lambda_2 = 2.0 - 0.7i$, and $\lambda_3 = -7.0 + 0i$. This scenario is also challenging for our ranking approaches due to this oscillatory behavior. Note, however, that the imaginary part of the leading eigenvalue is small compared to the real part. The order of expected sensitivities is given by $\mathbb{E}(s_1) < \mathbb{E}(s_3) < \mathbb{E}(s_2)$, which corresponds exactly to the order of species sensitivities from $k = 0.3$ to $k = 0.5$ (Fig. S3b, c). The order of eigenvector alignments is given by $|\mathbf{v}_{13}| < |\mathbf{v}_{11}| < |\mathbf{v}_{12}|$ and provides a reasonable match to the order of species sensitivities (Fig. S3b, c).

17

References

Arnoldi, J.F., Bideault, A., Loreau, M. & Haegeman, B. (2018). How ecosystems recover from pulse perturbations: A theory of short-to long-term responses. *Journal of theoretical biology*, 436, 79–92.

Benincà, E., Ballantine, B., Ellner, S.P. & Huisman, J. (2015). Species fluctuations sustained by a cyclic succession at the edge of chaos. *Proceedings of the National Academy of Sciences*, 112, 6389–6394.

Benincà, E., Jöhnk, K.D., Heerkloss, R. & Huisman, J. (2009). Coupled predator–prey oscillations in a chaotic food web. *Ecology letters*, 12, 1367–1378.

Boyce, W.E., DiPrima, R.C. & Meade, D.B. (2017). *Elementary differential equations*. John Wiley & Sons.

Case, T. (2000). *An Illustrated Guide to Theoretical Ecology*. Oxford University Press, Oxford.

Cenci, S., Medeiros, L.P., Sugihara, G. & Saavedra, S. (2020). Assessing the predictability of nonlinear dynamics under smooth parameter changes. *Journal of the Royal Society Interface*, 17, 20190627.

Cenci, S. & Saavedra, S. (2019). Non-parametric estimation of the structural stability of non-equilibrium community dynamics. *Nature Ecology & Evolution*, 3, 912–918.

Cenci, S., Sugihara, G. & Saavedra, S. (2019). Regularized s-map for inference and forecasting with noisy ecological time series. *Methods in Ecology and Evolution*, 10, 650–660.

Chang, C.W., Miki, T., Ushio, M., Ke, P.J., Lu, H.P., Shiah, F.K. & Hsieh, C.h. (2021). Re-constructing large interaction networks from empirical time series data. *Ecology Letters*, 24, 2763–2774.

Deyle, E.R., May, R.M., Munch, S.B. & Sugihara, G. (2016). Tracking and forecasting ecosystem interactions in real time. *Proceedings of the Royal Society B: Biological Sciences*, 283, 20152258.

Eckmann, J.P. & Ruelle, D. (1985). Ergodic theory of chaos and strange attractors. *The theory of chaotic attractors*, pp. 273–312.

Gilpin, M.E. (1979). Spiral chaos in a predator-prey model. *The American Naturalist*, 113, 306–308.

Ginelli, F., Poggi, P., Turchi, A., Chaté, H., Livi, R. & Politi, A. (2007). Characterizing dynamics with covariant lyapunov vectors. *Physical review letters*, 99, 130601.

Hastings, A. & Powell, T. (1991). Chaos in a three-species food chain. *Ecology*, 72, 896–903.

James, G., Witten, D., Hastie, T. & Tibshirani, R. (2021). *An introduction to statistical learning: with applications in R*. Springer.
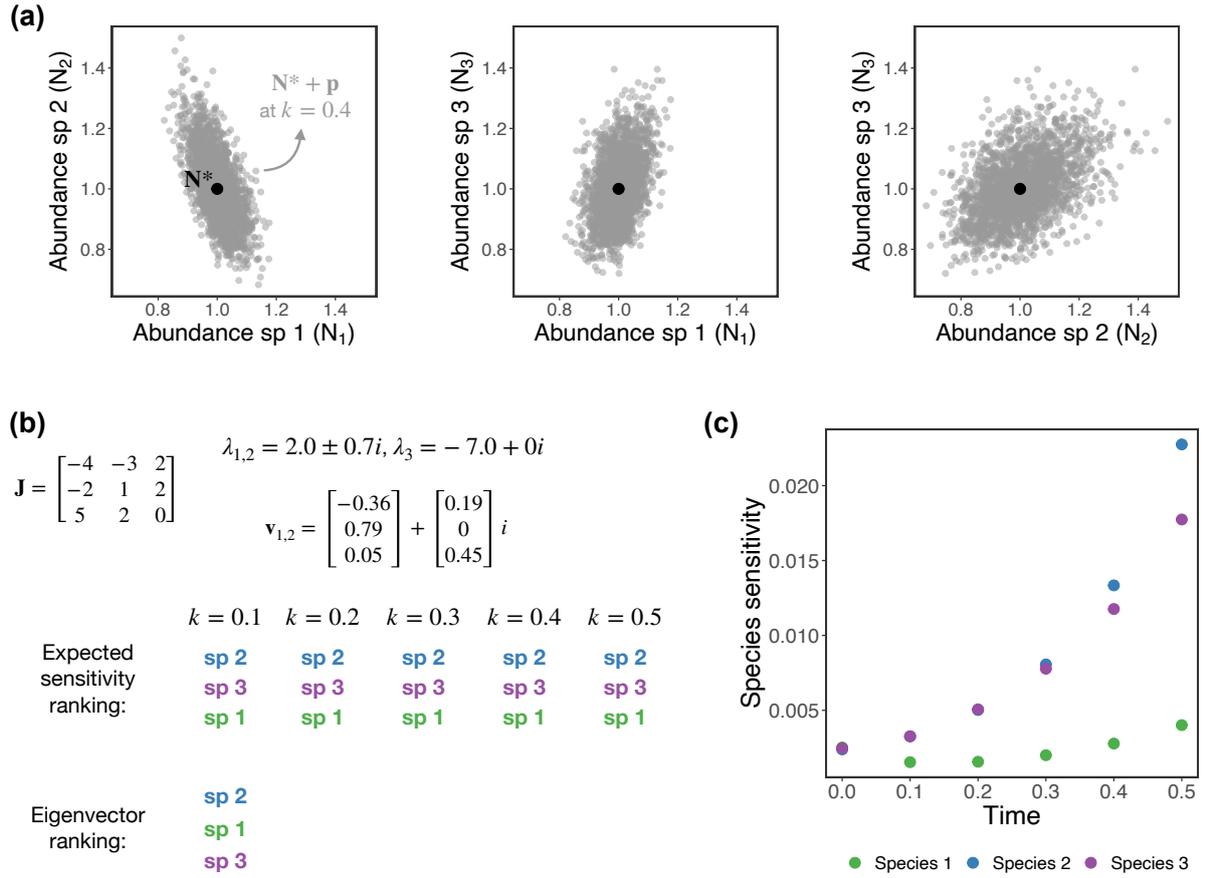
Kuptsov, P.V. & Parlitz, U. (2012). Theory and computation of covariant lyapunov vectors. *Journal of nonlinear science*, 22, 727–762.

Mease, K., Bharadwaj, S. & Iravanchy, S. (2003). Timescale analysis for nonlinear dynamical systems. *Journal of guidance, control, and dynamics*, 26, 318–330.

Song, C. & Saavedra, S. (2021). Bridging parametric and nonparametric measures of species interactions unveils new insights of non-equilibrium dynamics. *Oikos*.

Strogatz, S.H. (2018). *Nonlinear dynamics and chaos: with applications to physics, biology, chemistry, and engineering*. CRC press.

Sugihara, G. (1994). Nonlinear forecasting for the classification of natural time series. *Philosophical Transactions of the Royal Society of London. Series A: Physical and Engineering Sciences*, 348, 477–495.

Upadhyay, R. (2000). Chaotic behaviour of population dynamic systems in ecology. *Mathematical and computer modelling*, 32, 1005–1015.

Vallejo, J.C., Sanjuan, M.A. & Sanjuán, M.A. (2017). *Predictability of chaotic dynamics*. Springer.

Vano, J., Wildenberg, J., Anderson, M., Noel, J. & Sprott, J. (2006). Chaos in low-dimensional lotka–volterra models of competition. *Nonlinearity*, 19, 2391.

Yodzis, P. (1989). *Introduction to theoretical ecology*. HarperCollins College Division.
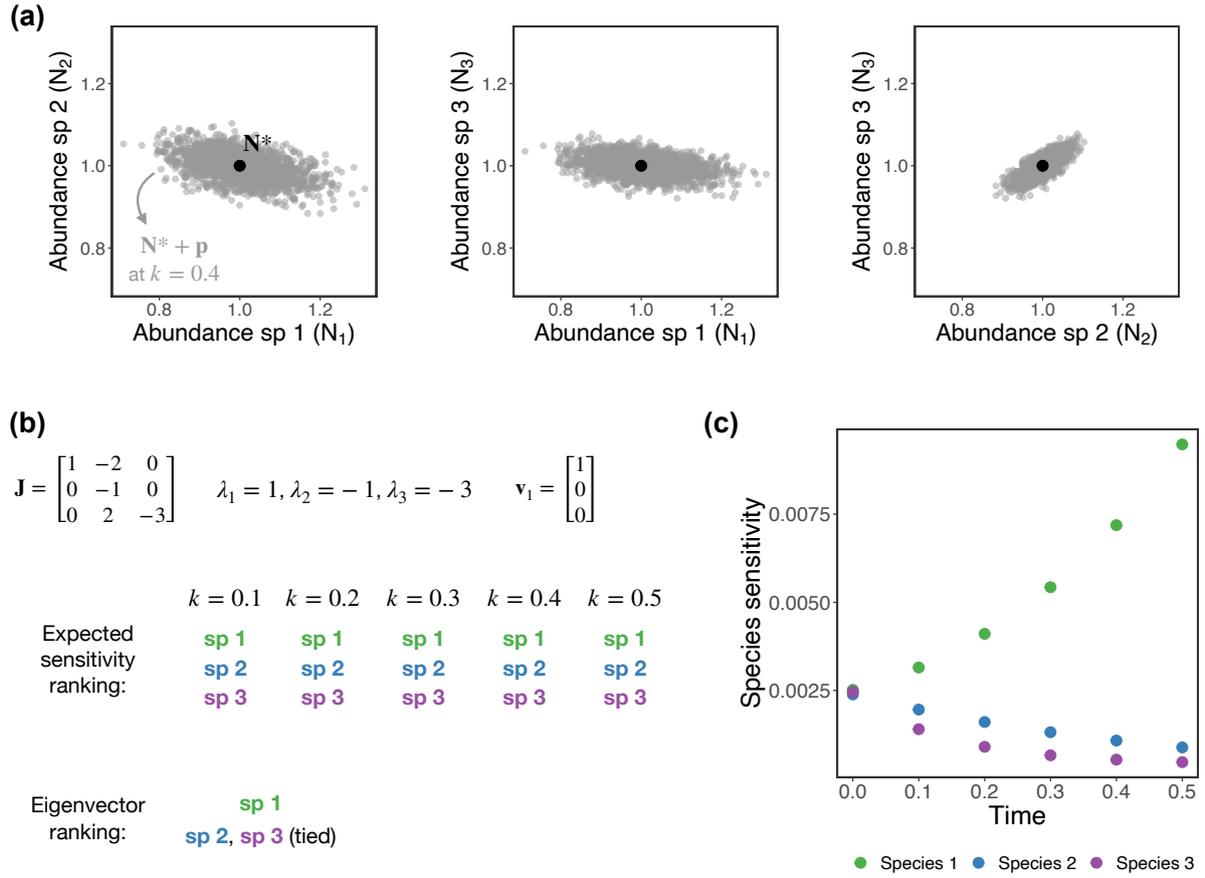
Figure S1. First scenario of Lotka-Volterra dynamics at equilibrium (see *Section 13*) showing how expected sensitivities ($\mathbb{E}(s_i)$) and alignments with the leading eigenvector ($|\mathbf{v}_{1i}|$) can rank species sensitivities to perturbations ($\langle s_i \rangle$). (a) Perturbed abundances ($\tilde{\mathbf{N}} = \mathbf{N}^* + \mathbf{p}$; 2,000 gray points) at time $k = 0.4$ projected onto the planes of species 1 and 2 (left), species 1 and 3 (middle), and species 2 and 3 (right). (b) Jacobian matrix ($\mathbf{J}$) and its eigenvalues (λ_i) and leading eigenvector ($\mathbf{v}_1$) for this Lotka-Volterra system (top). The order of expected sensitivities (computed using different values of k) and eigenvector alignments (bottom). (c) Species sensitivities computed using the perturbed abundances (gray points in (a)) at different points in time (i.e., for different values of k). In this scenario, the expected sensitivity ranking is more accurate than the eigenvector ranking.

(a)

(b)

$$\mathbf{J} = \begin{bmatrix} 4 & 0.5 & 0 \\ 0.5 & -10 & -8 \\ 0 & -8 & -1 \end{bmatrix} \quad \lambda_1 = 5.2, \lambda_2 = 4.0, \lambda_3 = -14.2 \quad \mathbf{v}_1 = \begin{bmatrix} -0.18 \\ -0.46 \\ 0.87 \end{bmatrix}$$

	$k = 0.1$	$k = 0.2$	$k = 0.3$	$k = 0.4$	$k = 0.5$
Expected sensitivity ranking:	sp 3	sp 3	sp 3	sp 3	sp 3
	sp 1	sp 1	sp 1	sp 1	sp 1
	sp 2	sp 2	sp 2	sp 2	sp 2

Eigenvector ranking:	sp 3
	sp 2
	sp 1

(c)

Figure S2. Second scenario of Lotka-Volterra dynamics at equilibrium (see *Section 13*) showing how expected sensitivities ($\mathbb{E}(s_i)$) and alignments with the leading eigenvector ($|\mathbf{v}_{1i}|$) can rank species sensitivities to perturbations ($\langle s_i \rangle$). (a) Perturbed abundances ($\tilde{\mathbf{N}} = \mathbf{N}^* + \mathbf{p}$; 2,000 gray points) at time $k = 0.4$ projected onto the planes of species 1 and 2 (left), species 1 and 3 (middle), and species 2 and 3 (right). (b) Jacobian matrix (**J**) and its eigenvalues (λ_i) and leading eigenvector ($\mathbf{v}_1$) for this Lotka-Volterra system (top). The order of expected sensitivities (computed using different values of k) and eigenvector alignments (bottom). (c) Species sensitivities computed using the perturbed abundances (gray points in (a)) at different points in time (i.e., for different values of k). In this scenario, the expected sensitivity ranking is more accurate than the eigenvector ranking.

Figure S3. Third scenario of Lotka-Volterra dynamics at equilibrium (see *Section 13*) showing how expected sensitivities ($\mathbb{E}(s_i)$) and alignments with the leading eigenvector ($|\mathbf{v}_{1i}|$) can rank species sensitivities to perturbations ($\langle s_i \rangle$). (a) Perturbed abundances ($\tilde{\mathbf{N}} = \mathbf{N}^* + \mathbf{p}$; 2,000 gray points) at time $k = 0.4$ projected onto the planes of species 1 and 2 (left), species 1 and 3 (middle), and species 2 and 3 (right). (b) Jacobian matrix ($\mathbf{J}$) and its eigenvalues (λ_i) and leading eigenvector ($\mathbf{v}_1$) for this Lotka-Volterra system (top). The order of expected sensitivities (computed using different values of k) and eigenvector alignments (bottom). (c) Species sensitivities computed using the perturbed abundances (gray points in (a)) at different points in time (i.e., for different values of k). In this scenario, the expected sensitivity ranking is more accurate than the eigenvector ranking.

Figure S4. Alignments (i.e., absolute value of cosine of the angle) between the initial ($\mathbf{p}(t)$) and final ($\mathbf{p}(t + k)$) perturbation vector for two directions of $\mathbf{p}(t)$ for the five population dynamics models (see *Section 10*). Boxplots on the left correspond to $\mathbf{p}(t)$ in the direction of the leading eignevector ($\mathbf{v}_1$) whereas boxplots on the right correspond to $\mathbf{p}(t)$ in a random direction. Note that $\mathbf{p}(t + k)$ converges to the leading Lyapunov vector ($\mathbf{w}_1$) when $\mathbf{p}(t)$ is in the direction of $\mathbf{v}_1$. The figure shows that $\mathbf{v}_1$ is on average much more aligned with $\mathbf{w}_1$ (left boxplots) than what is expected at random (right boxplots).
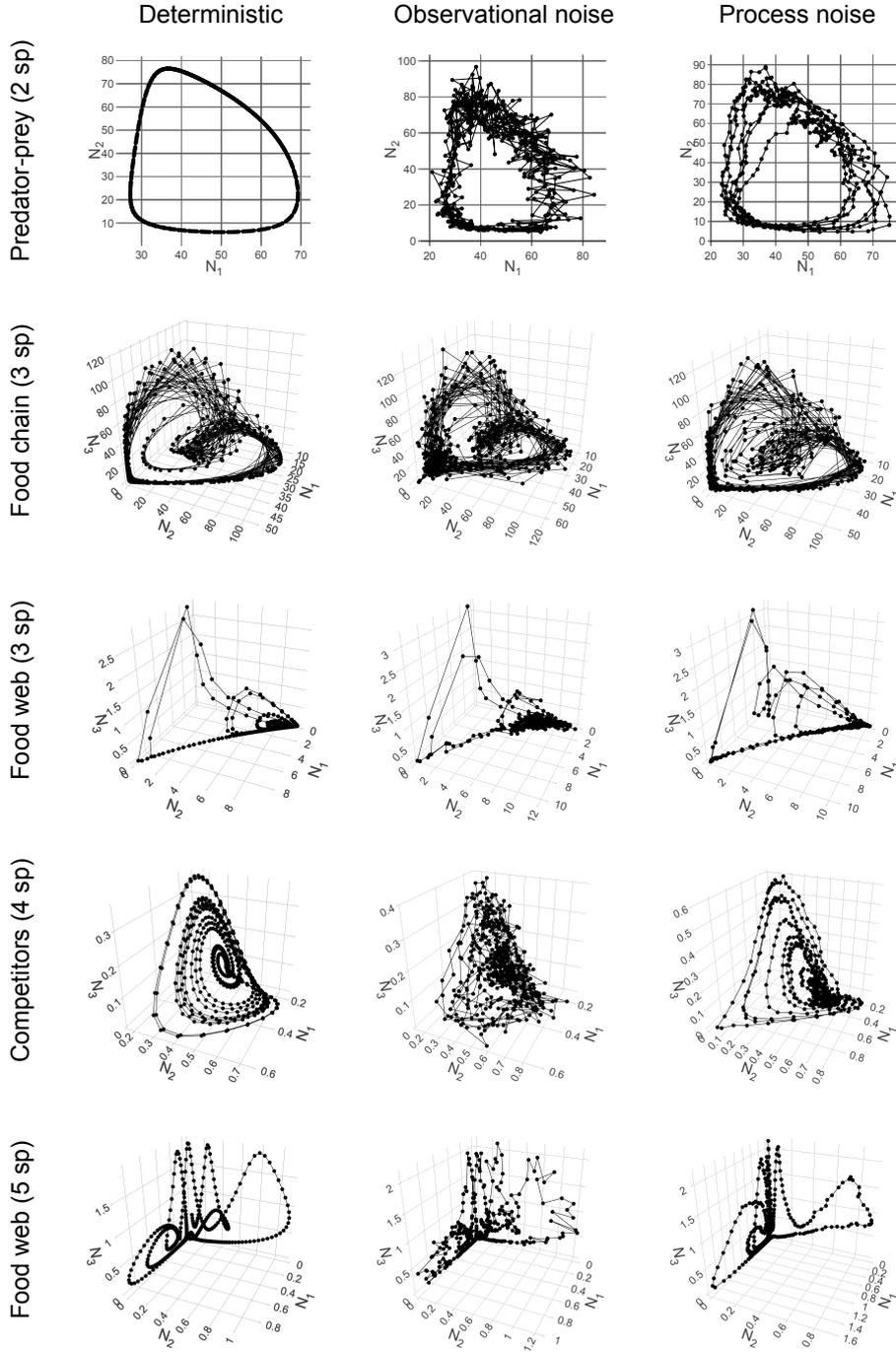
Figure S5. Attractors in state space corresponding to each multivariate synthetic time series generated from a population dynamics model (different rows; see *Section 3*) with a different type of noise (different columns; see *Section 6*). Each plot shows the 500 points ($\{\mathbf{N}(t)\}$, $t = 1, ..., 500$) generated by numerically integrating the indicated model and then sampling equidistant points. Note that we only show the abundances of species 1, 2, and 3 for models with more than 3 species.

24
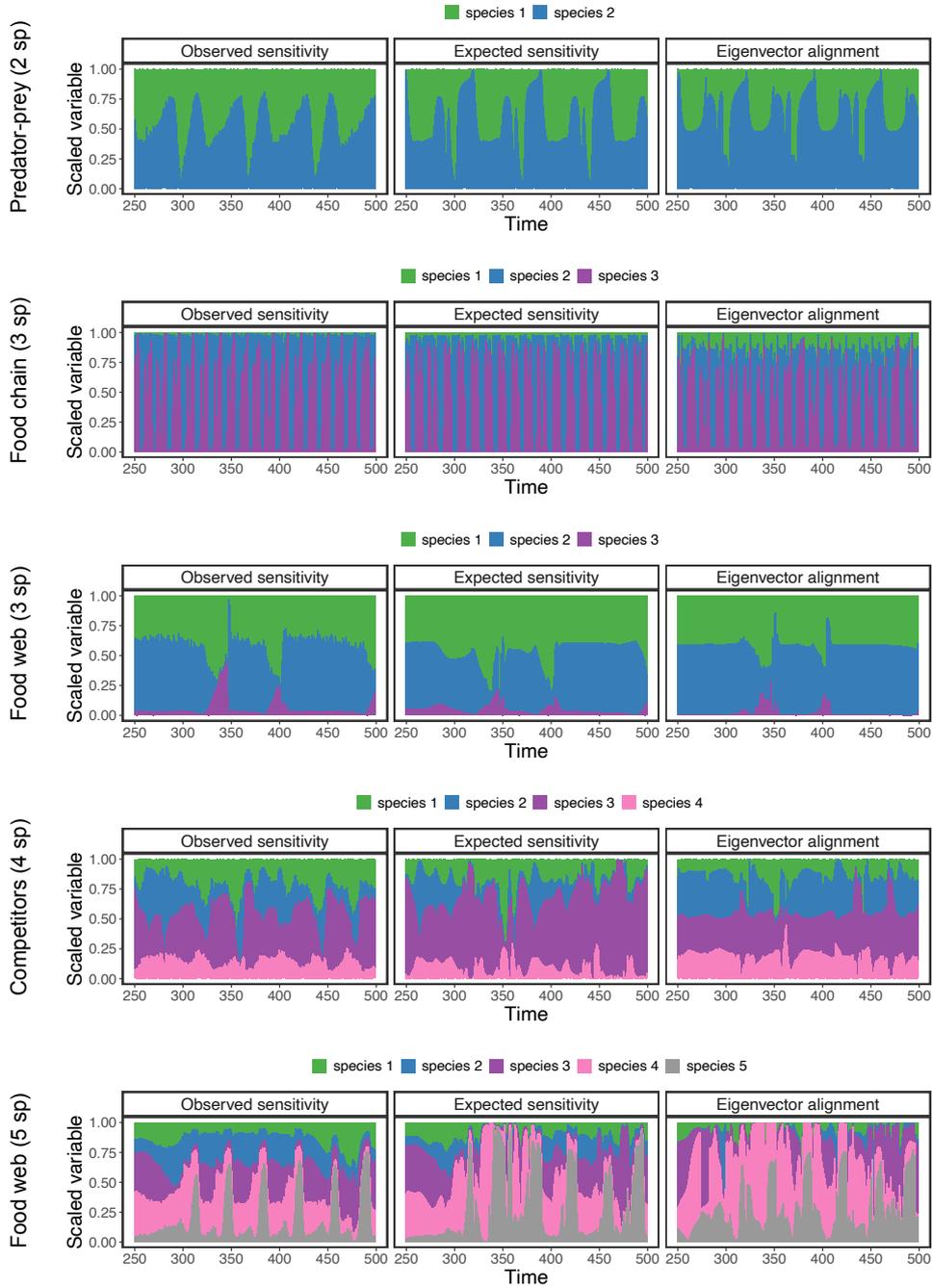
Figure S6. Species sensitivities computed from our perturbation analyses ($\langle s_i \rangle$; first column) as well as expected sensitivities ($\mathbb{E}(s_i)$; second column) and eigenvector alignments ($|\mathbf{v}_{1i}|$; third column) inferred from each synthetic time series (different rows) with the S-map over time. A bar in one of the plots shows the values of the corresponding variable (i.e., $\langle s_i \rangle$, $\mathbb{E}(s_i)$, or $|\mathbf{v}_{1i}|$) across species. Note that variables are rescaled to sum 1 across species to improve visualization but that this procedure does not change the rankings. These results correspond to our main set of analyses with synthetic time series shown in the main text (Fig. 3).
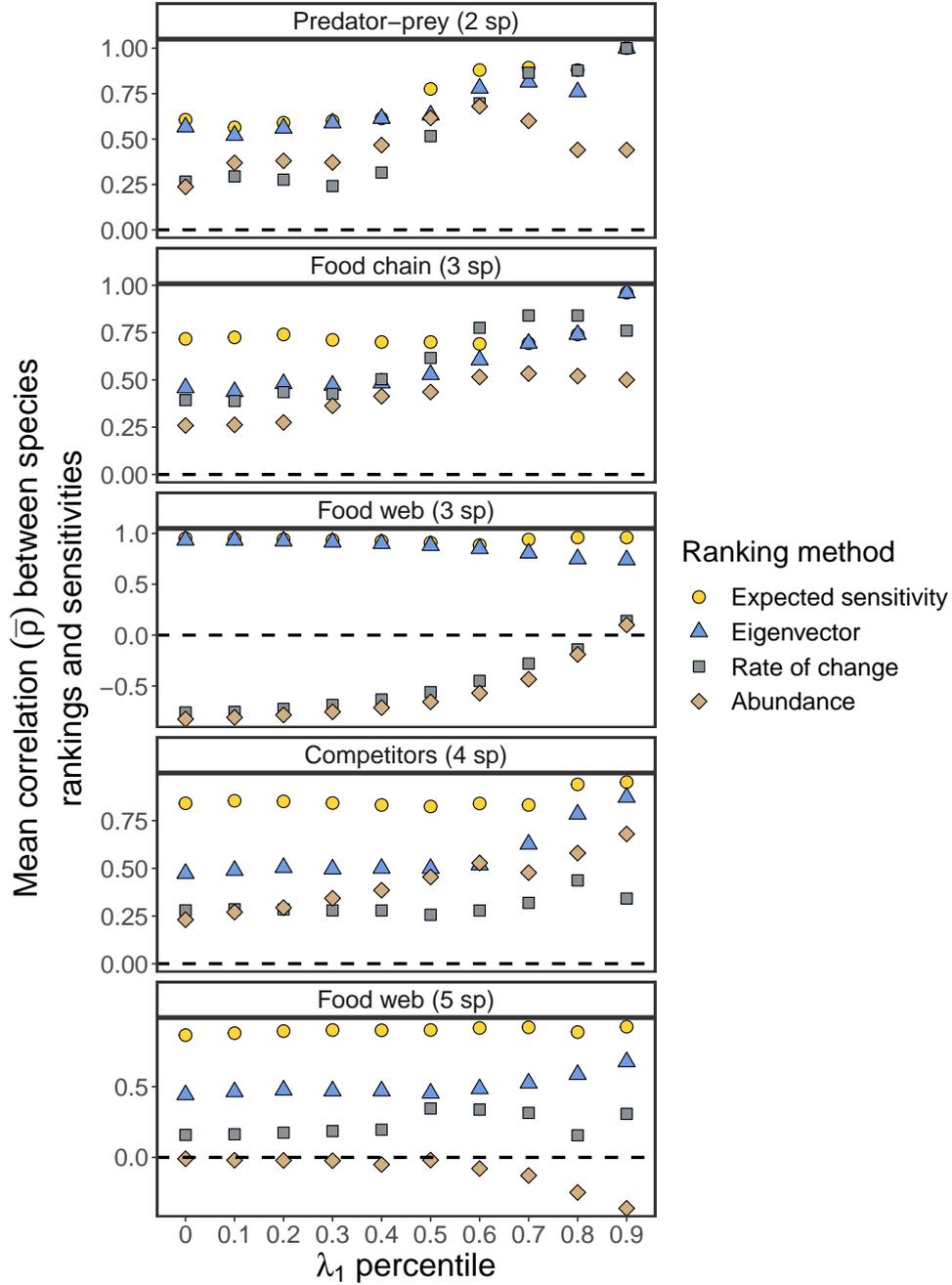
Figure S7. Mean Spearman's rank correlation over time ($\bar{\rho}$) between species sensitivities to perturbation ($\langle s_i \rangle$) and four different approaches (expected sensitivity, $\mathbb{E}(s_i)$; eigenvector, $|\mathbf{v}_{1i}|$; rate of change, $\Delta N_i(t)$; and abundance, $-N_i(t)$) as a function of the percentile of λ_1 used to filter the time series. Each point represents the $\bar{\rho}$ value obtained using a given ranking approach after removing time series points with a λ_1 value lower than the indicated percentile of the λ_1 distribution. The figure shows that, for most models, the expected sensitivity and eigenvector rankings (yellow circles and blue triangles) become more accurate (i.e., higher $\bar{\rho}$) when we only use points with a high λ_1. Note that we compute $\mathbb{E}(s_i)$, $|\mathbf{v}_{1i}|$, and λ_1 analytically for this figure. Also note that the values of $\bar{\rho}$ for the 0th percentile are exactly the same as the ones shown in Fig. 3a in the main text.
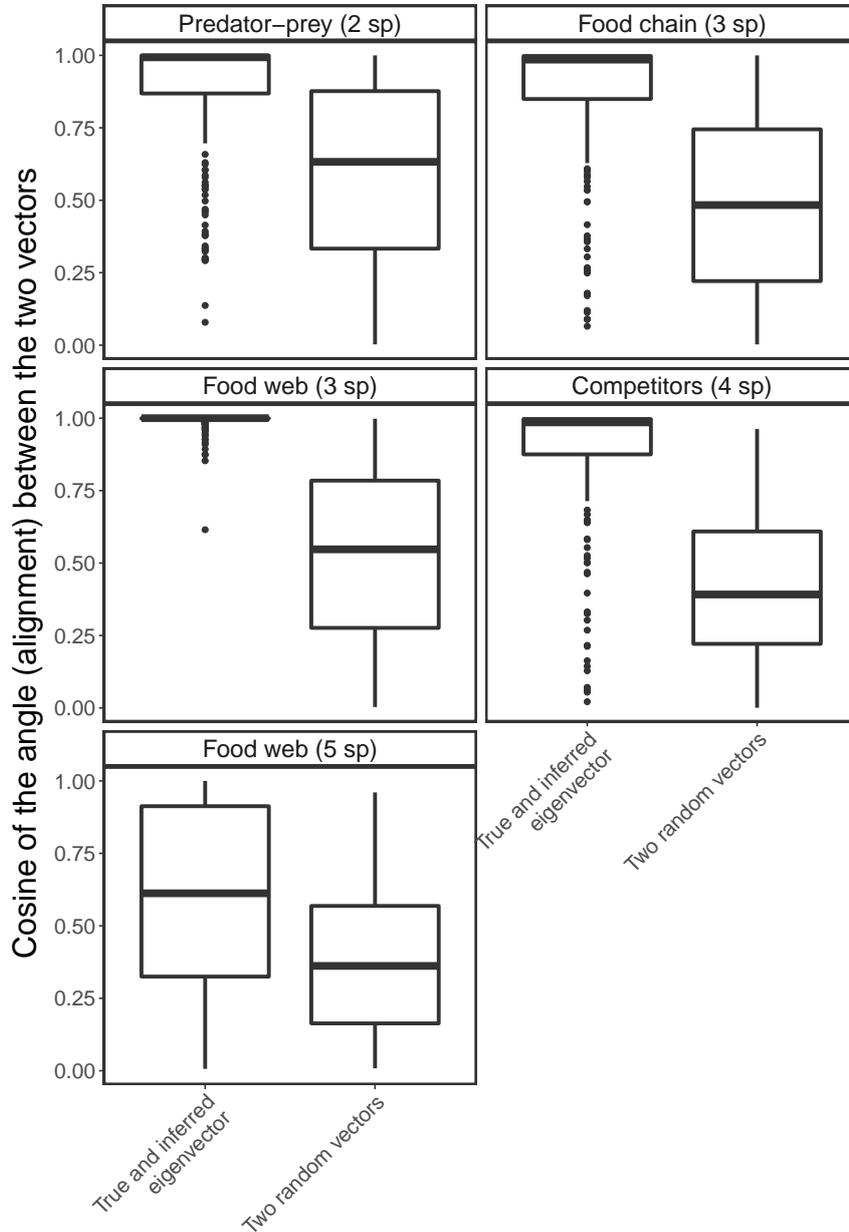
Figure S8. Alignments (i.e., absolute value of cosine of the angle) between $\mathbf{v}_1$ inferred with the S-map and $\mathbf{v}_1$ computed from the analytical Jacobian matrix (left boxplots) as well as alignments between two randomly sampled vectors (right boxplots) for each of the five population dynamics models. Each boxplot on the left shows the alignment values computed using the second half of each time series (i.e., last 250 points) for which the S-map was used to infer $\mathbf{v}_1$ (see *Section 5*). Each boxplot on the right shows the alignment values computed using 250 pairs of vectors with random directions. The figure shows that $\mathbf{v}_1$ inferred with the S-map is on average much more aligned with the analytical $\mathbf{v}_1$ than what is expected if their directions are sampled at random.
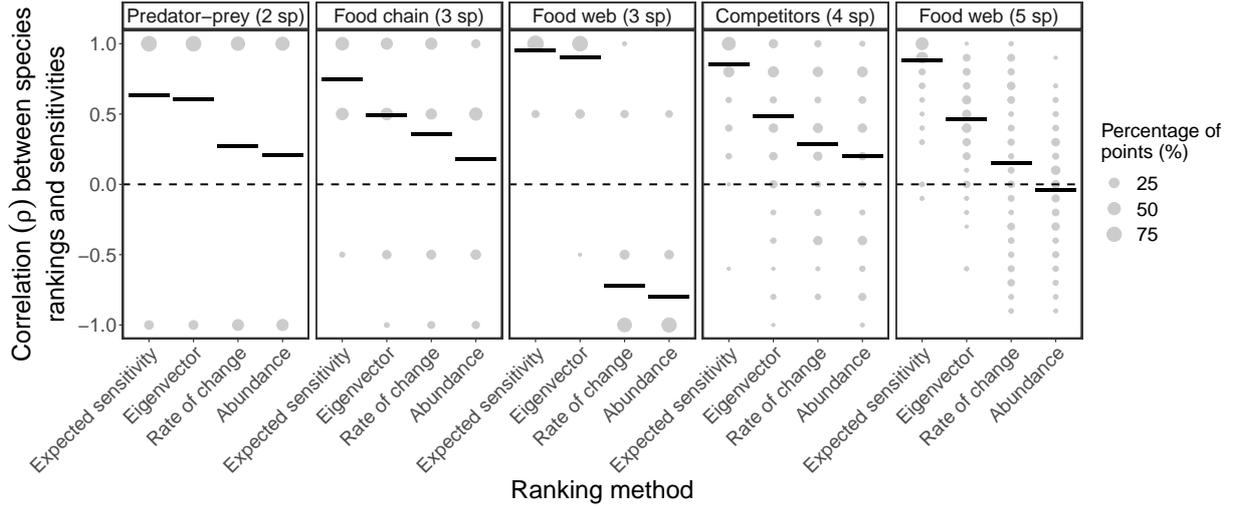
Figure S9. Same as Fig. 3a in the main text, but performing uniformly distributed perturbations instead of normally distributed perturbations (see *Section 4*). The figure shows the percentage of points with a given rank correlation value (ρ, size of gray points) and the average rank correlation ($\bar{\rho}$, horizontal lines) between species sensitivities to perturbations ($\langle s_i \rangle$) and four different approaches (expected sensitivity, $\mathbb{E}(s_i)$; eigenvector, $|\mathbf{v}_{1i}|$; rate of change, $\Delta N_i(t)$; and abundance, $-N_i(t)$). Note that we compute $\mathbb{E}(s_i)$ and $|\mathbf{v}_{1i}|$ analytically for this figure. For this figure, perturbed abundances ($\tilde{\mathbf{N}}$) are uniformly sampled inside a hypersphere of radius r centered in $\mathbf{N}$, were r corresponds to 15% of the mean standard deviation of species abundances.
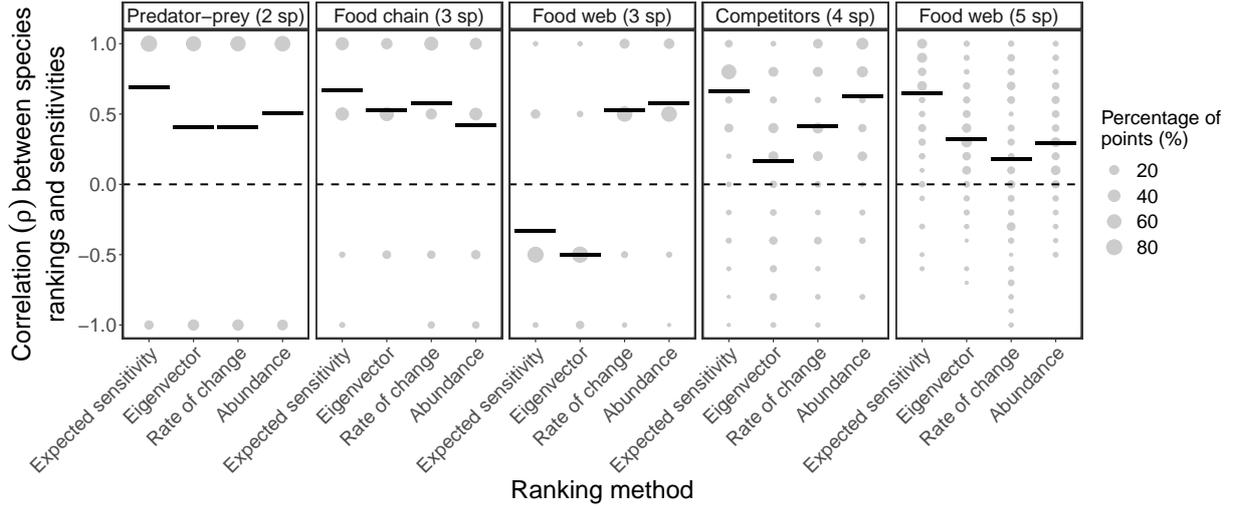
Figure S10. Same as Fig. 3a in the main text, but performing normally distributed perturbations with a variance proportional to relative species abundances instead of a fixed variance over time (see *Section 4*). The figure shows the percentage of points with a given rank correlation value (ρ, size of gray points) and the average rank correlation ($\bar{\rho}$, horizontal lines) between species sensitivities to perturbations ($\langle s_i \rangle$) and four different approaches (expected sensitivity, $\mathbb{E}(s_i)$; eigenvector, $|\mathbf{v}_{1i}|$; rate of change, $\Delta N_i(t)$; and abundance, $-N_i(t)$). Note that we compute $\mathbb{E}(s_i)$ and $|\mathbf{v}_{1i}|$ analytically for this figure. For this figure, we sample perturbations to $\mathbf{N}(t)$ as: $p_i(t) \sim \mathcal{N}(\mu = 0, \sigma^2 = N_i'(t)r^2)$, where $N_i'(t) = \frac{N_i(t)}{\sum_{i=1}^{S} N_i(t)}$ and were r corresponds to 15% of the mean standard deviation of species abundances.
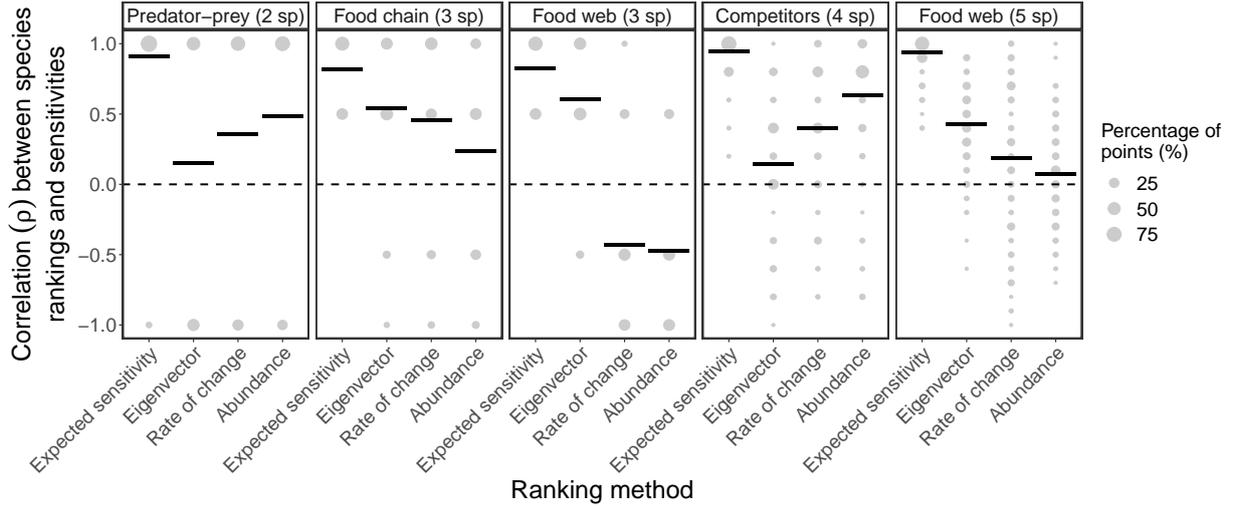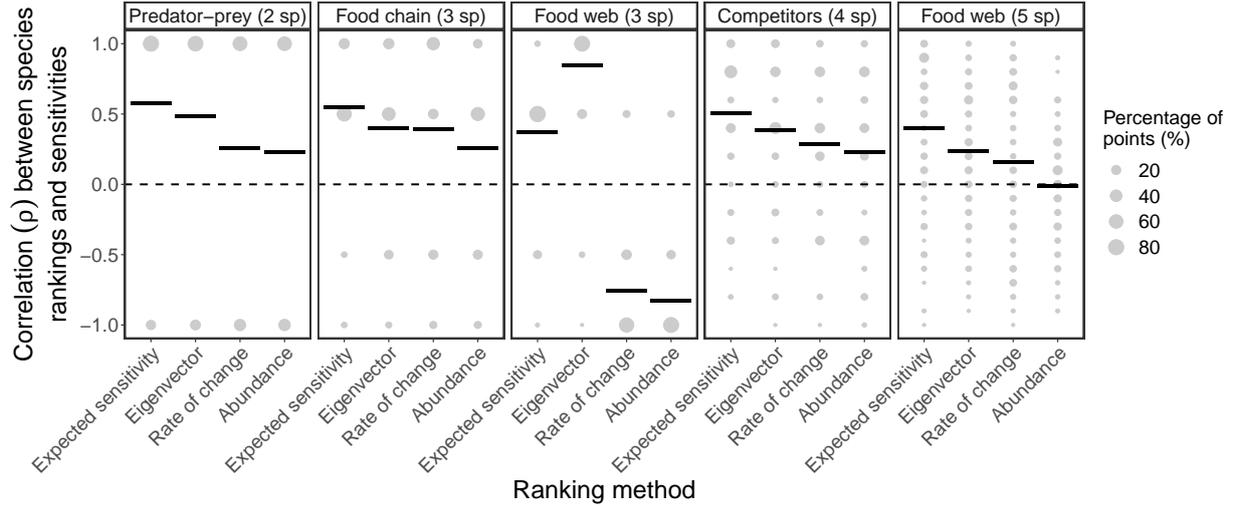
Figure S11. Same as Fig. 3a in the main text, but using $k = 1$ as the time step to integrate perturbed and unperturbed abundances instead of k being inversely proportional to the mean absolute abundance percent change (see *Section 4*). The figure shows the percentage of points with a given rank correlation value (ρ, size of gray points) and the average rank correlation ($\bar{\rho}$, horizontal lines) between species sensitivities to perturbations ($\langle s_i \rangle$) and four different approaches (expected sensitivity, $\mathbb{E}(s_i)$; eigenvector, $|\mathbf{v}_{1i}|$; rate of change, $\Delta N_i(t)$; and abundance, $-N_i(t)$). Note that we compute $\mathbb{E}(s_i)$ and $|\mathbf{v}_{1i}|$ analytically for this figure. For this figure, we numerically integrate every perturbed ($\tilde{\mathbf{N}}(t)$) and unperturbed abundance ($\mathbf{N}(t)$) for $k = 1$ time step to compute $\langle s_i \rangle$.
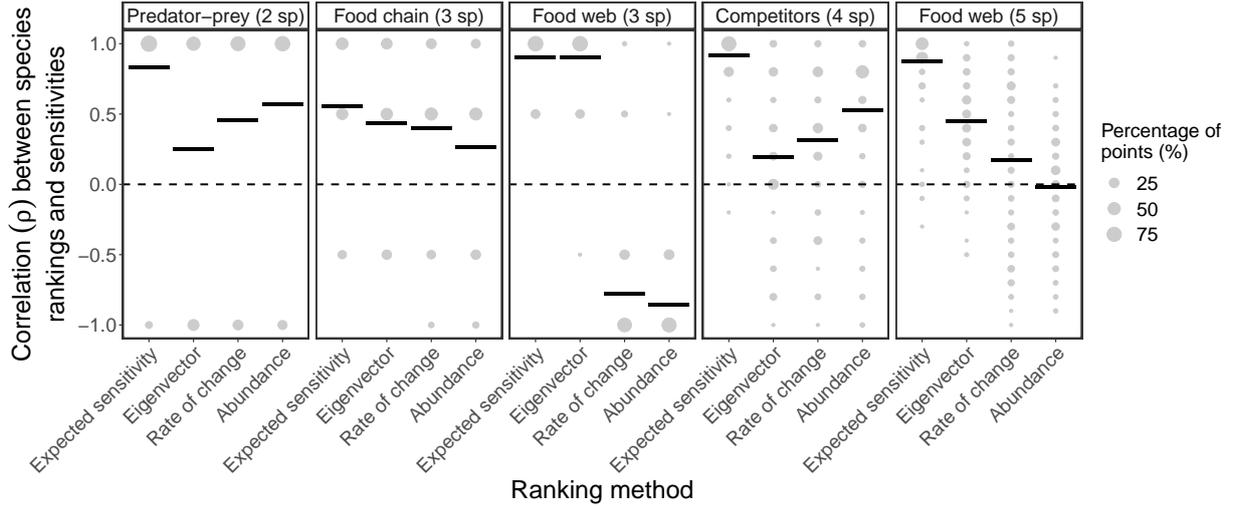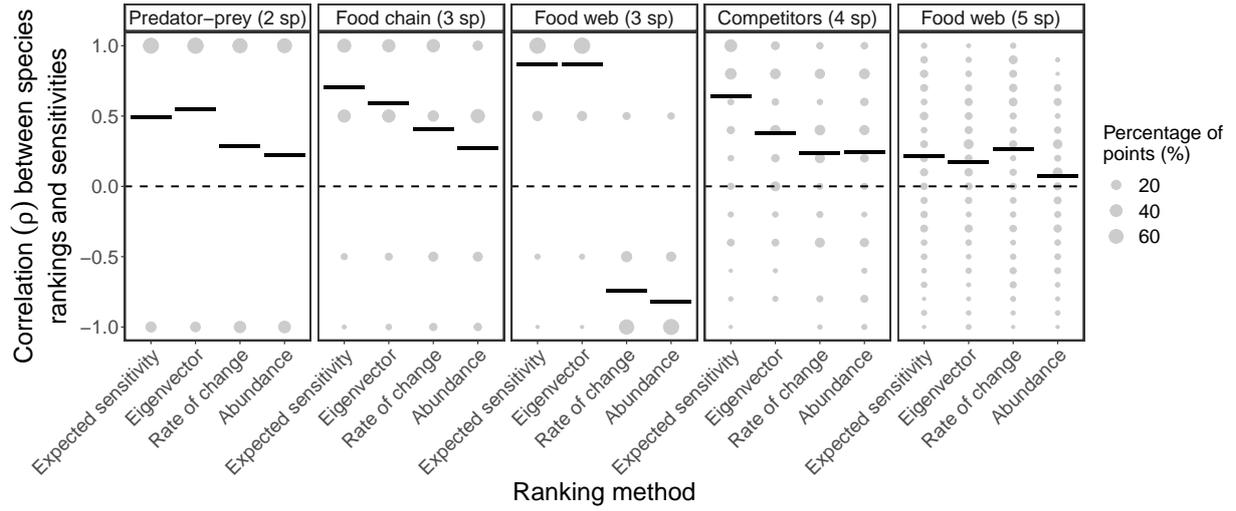
Figure S12. Same as Fig. 3a in the main text, but using $k = 3$ as the time step to integrate perturbed and unperturbed abundances instead of k being inversely proportional to the mean absolute abundance percent change (see *Section 4*). The figure shows the percentage of points with a given rank correlation value (ρ, size of gray points) and the average rank correlation ($\bar{\rho}$, horizontal lines) between species sensitivities to perturbations ($\langle s_i \rangle$) and four different approaches (expected sensitivity, $\mathbb{E}(s_i)$; eigenvector, $|\mathbf{v}_{1i}|$; rate of change, $\Delta N_i(t)$; and abundance, $-N_i(t)$). Note that we compute $\mathbb{E}(s_i)$ and $|\mathbf{v}_{1i}|$ analytically for this figure. For this figure, we numerically integrate every perturbed ($\tilde{\mathbf{N}}(t)$) and unperturbed abundance ($\mathbf{N}(t)$) for $k = 3$ time steps to compute $\langle s_i \rangle$.
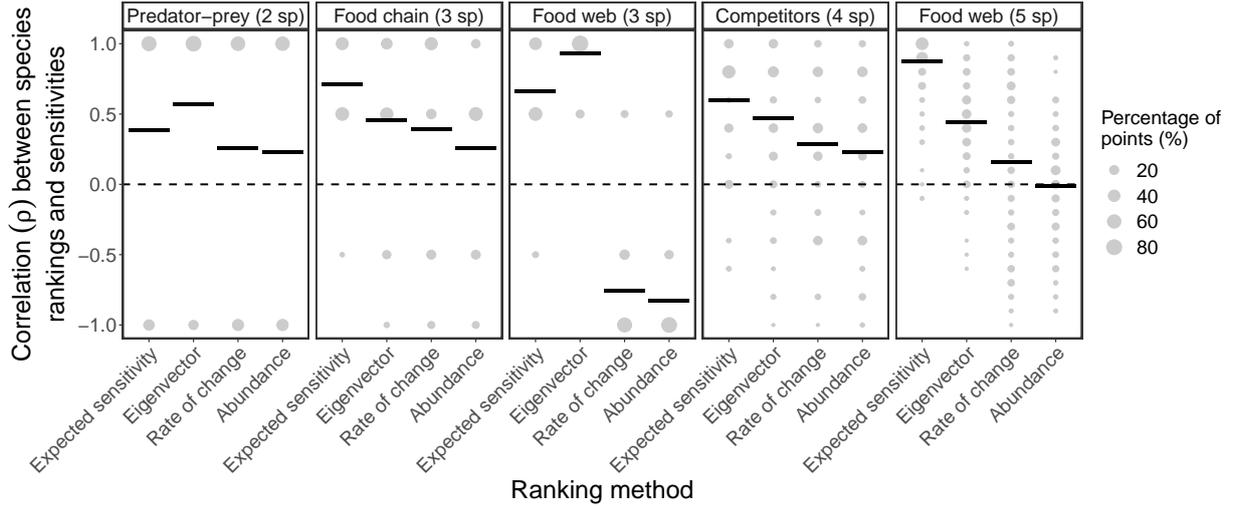
Figure S13. Same as Fig. 3a in the main text, but using $k = 1$ as the time step to compute expected sensitivities ($\mathbb{E}(s_i)$) when the true time step used to integrate perturbed and unperturbed abundances is inversely proportional to the mean absolute abundance percent change (see *Section 2*). The figure shows the percentage of points with a given rank correlation value (ρ, size of gray points) and the average rank correlation ($\bar{\rho}$, horizontal lines) between species sensitivities to perturbations ($\langle s_i \rangle$) and four different approaches (expected sensitivity, $\mathbb{E}(s_i)$; eigenvector, $|\mathbf{v}_{1i}|$; rate of change, $\Delta N_i(t)$; and abundance, $-N_i(t)$). Note that we compute $\mathbb{E}(s_i)$ and $|\mathbf{v}_{1i}|$ analytically for this figure. For this figure, we numerically integrate every perturbed ($\tilde{\mathbf{N}}(t)$) and unperturbed abundance ($\mathbf{N}(t)$) for a time step k that depends on the local time scale of the dynamics, but always compute $\mathbb{E}(s_i)$ using $k = 1$.
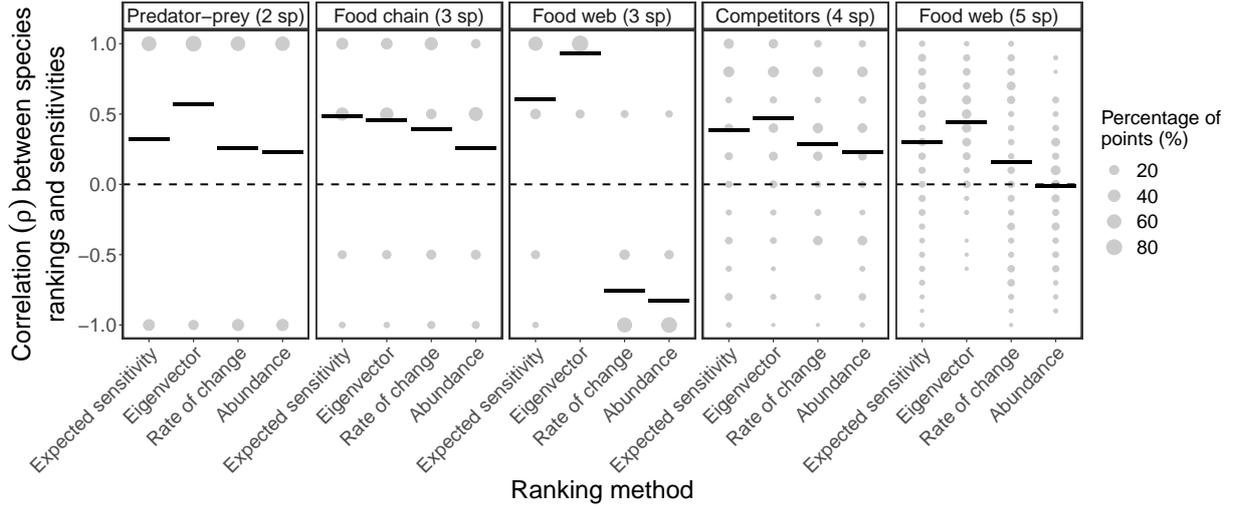
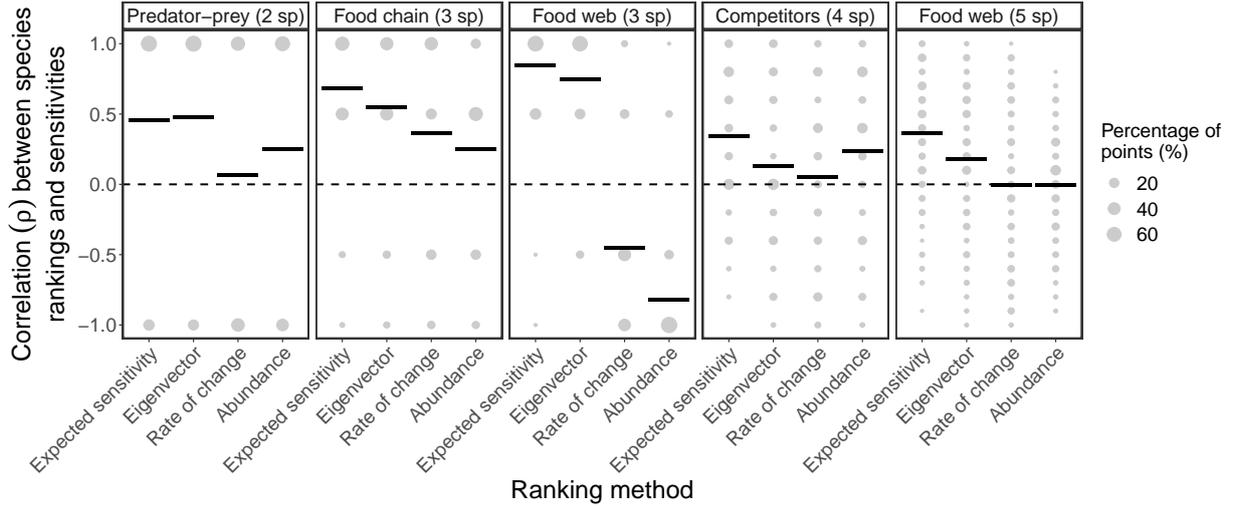**Figure S14.** Same as Fig. 3a in the main text, but adding a normally distributed noise to k and $\boldsymbol{\Sigma}_t$ at each point in time to compute expected sensitivities ($\mathbb{E}(s_i)$; see *Section 2*). The figure shows the percentage of points with a given rank correlation value (ρ, size of gray points) and the average rank correlation ($\bar{\rho}$, horizontal lines) between species sensitivities to perturbations ($\langle s_i \rangle$) and four different approaches (expected sensitivity, $\mathbb{E}(s_i)$; eigenvector, $|\mathbf{v}_{1i}|$; rate of change, $\Delta N_i(t)$; and abundance, $-N_i(t)$). Note that we compute $\mathbb{E}(s_i)$ and $|\mathbf{v}_{1i}|$ analytically for this figure. For this figure, we perform the same perturbation analyses as described for Fig. 3 (see *Section 4*), but add 100% of a normally distributed noise to the true value of k and to $\boldsymbol{\Sigma}_t = \mathbf{I}$ before computing $\mathbb{E}(s_i)$.
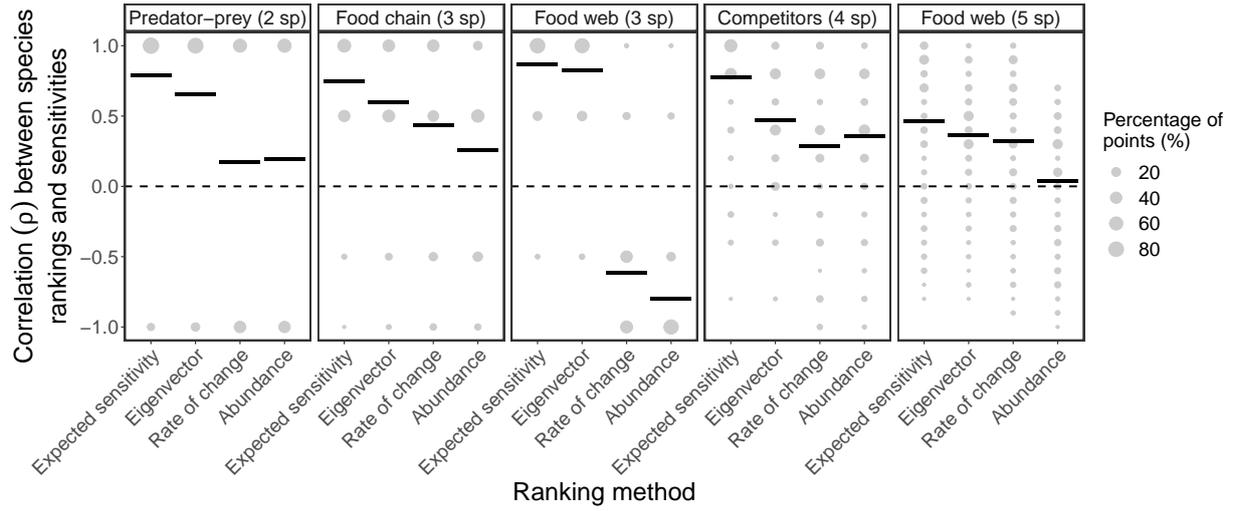
Figure S15. Same as Fig. 3b in the main text, but normalizing the abundances of each species i ($N_i(t)$) in the training set to mean zero and unit standard deviation before performing the S-map. The figure shows the percentage of points with a given rank correlation value (ρ, size of gray points) and the average rank correlation ($\bar{\rho}$, horizontal lines) between species sensitivities to perturbations ($\langle s_i \rangle$) and four different approaches (expected sensitivity, $\mathbb{E}(s_i)$; eigenvector, $|\mathbf{v}_{1i}|$; rate of change, $\Delta N_i(t)$; and abundance, $-N_i(t)$). Note that we infer the Jacobian matrix with the S-map using a moving training set in order to compute $\mathbb{E}(s_i)$ and $|\mathbf{v}_{1i}|$ for this figure.
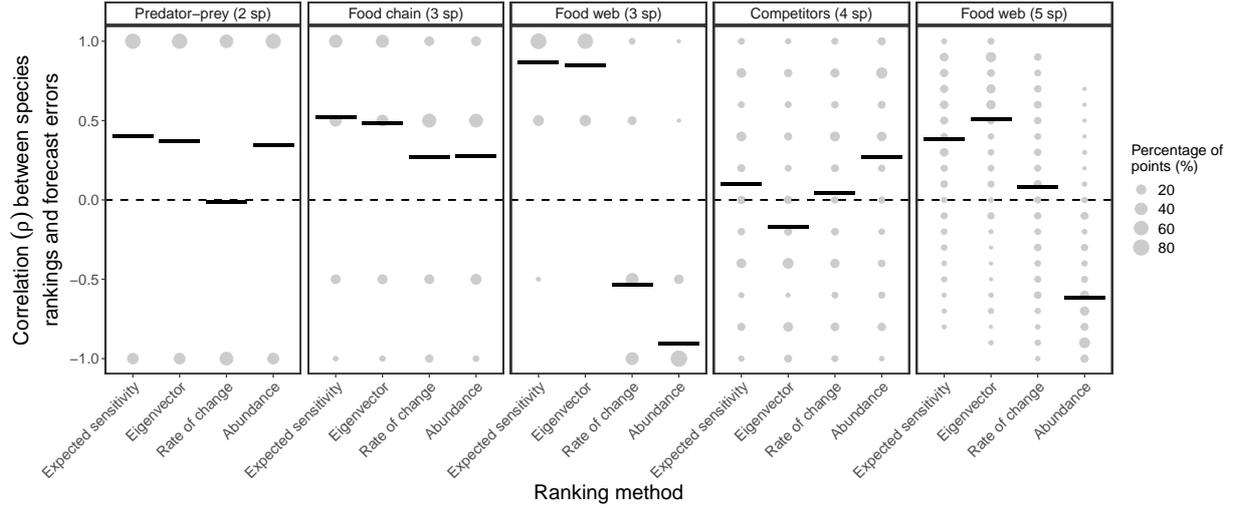
Figure S16. Same as Fig. 3b in the main text, but using a shorter training set with 100 instead of 250 points to perform the S-map (see *Section 6*). The figure shows the percentage of points with a given rank correlation value (ρ, size of gray points) and the average rank correlation ($\bar{\rho}$, horizontal lines) between species sensitivities to perturbations ($\langle s_i \rangle$) and four different approaches (expected sensitivity, $\mathbb{E}(s_i)$; eigenvector, $|\mathbf{v}_{1i}|$; rate of change, $\Delta N_i(t)$; and abundance, $-N_i(t)$). Note that we infer the Jacobian matrix with the S-map using a moving training set in order to compute $\mathbb{E}(s_i)$ and $|\mathbf{v}_{1i}|$ for this figure.

Figure S17. Same as Fig. 3b in the main text, but adding 10% of observational noise to the training set before performing the S-map (see *Section 6*). The figure shows the percentage of points with a given rank correlation value (ρ, size of gray points) and the average rank correlation ($\bar{\rho}$, horizontal lines) between species sensitivities to perturbations ($\langle s_i \rangle$) and four different approaches (expected sensitivity, $\mathbb{E}(s_i)$; eigenvector, $|\mathbf{v}_{1i}|$; rate of change, $\Delta N_i(t)$; and abundance, $-N_i(t)$). Note that we infer the Jacobian matrix with the S-map using a moving training set in order to compute $\mathbb{E}(s_i)$ and $|\mathbf{v}_{1i}|$ for this figure.
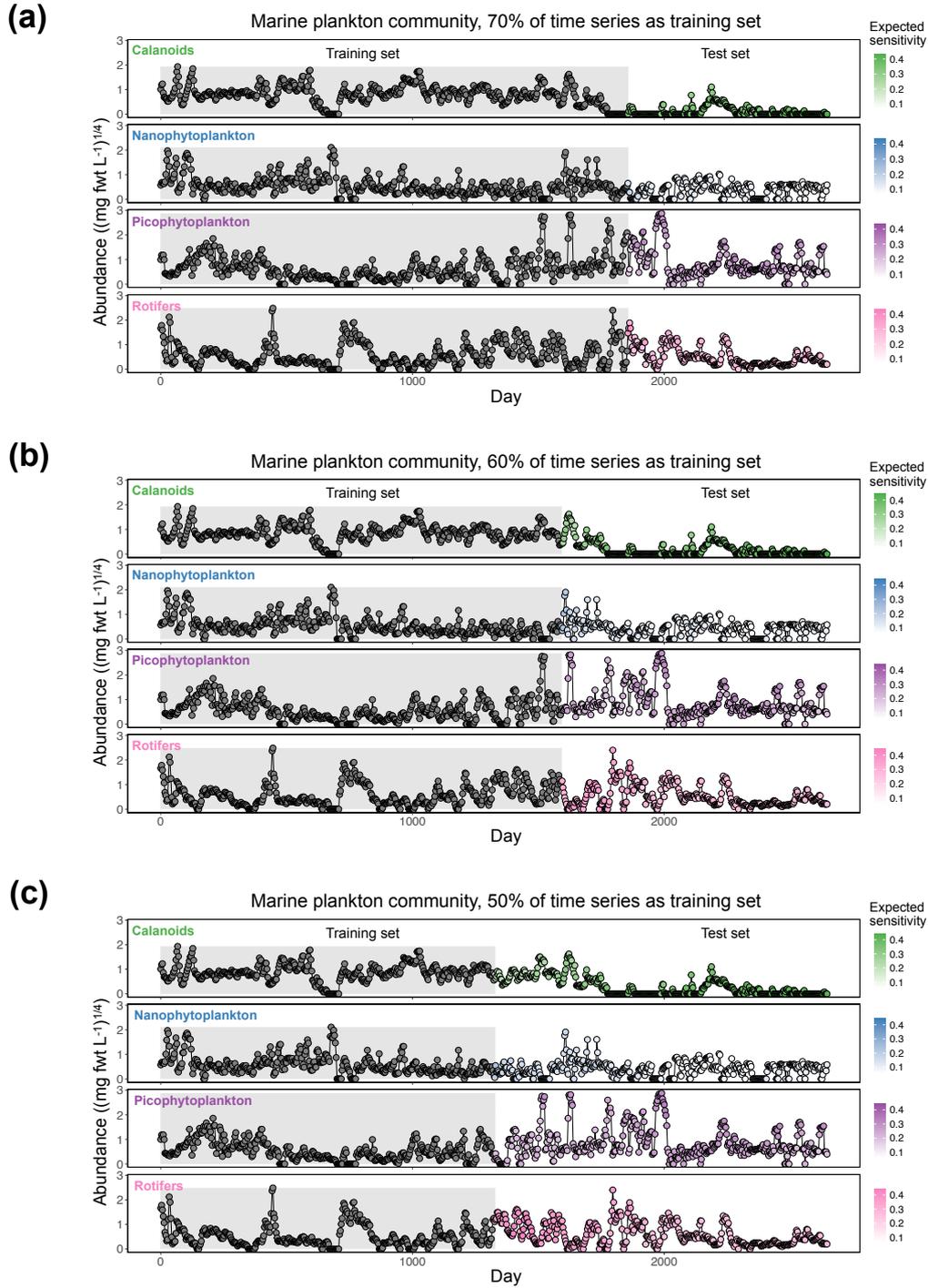
Figure S18. Same as Fig. 3b in the main text, but generating each synthetic time series with the population dynamics model containing stochasticity (i.e., process noise; see *Section 6*). The figure shows the percentage of points with a given rank correlation value (ρ, size of gray points) and the average rank correlation ($\bar{\rho}$, horizontal lines) between species sensitivities to perturbations ($\langle s_i \rangle$) and four different approaches (expected sensitivity, $\mathbb{E}(s_i)$; eigenvector, $|\mathbf{v}_{1i}|$; rate of change, $\Delta N_i(t)$; and abundance, $-N_i(t)$). Note that we infer the Jacobian matrix with the S-map using a moving training set in order to compute $\mathbb{E}(s_i)$ and $|\mathbf{v}_{1i}|$ for this figure.

Figure S19. Similar to Fig. 3b in the main text, but here we compute the Spearman's rank correlation (ρ) between species average forecast errors under perturbations ($\bar{\epsilon}_i$; see *Section 8*) and the four ranking approaches (expected sensitivity, $\mathbb{E}(s_i)$; eigenvector, $|\mathbf{v}_{1i}|$; rate of change, $\Delta N_i(t)$; and abundance, $-N_i(t)$). The figure shows the percentage of points with a given ρ value (size of gray points) and the average rank correlation ($\bar{\rho}$, horizontal lines). Note that we infer the Jacobian matrix with the S-map using a moving training set in order to compute $\mathbb{E}(s_i)$ and $|\mathbf{v}_{1i}|$ for this figure. This figure illustrates our hypothesis that species that are more sensitive to perturbations (i.e., high $\mathbb{E}(s_i)$ or $|\mathbf{v}_{1i}|$) tend to be harder to forecast under perturbations (i.e., high $\bar{\epsilon}_i$).
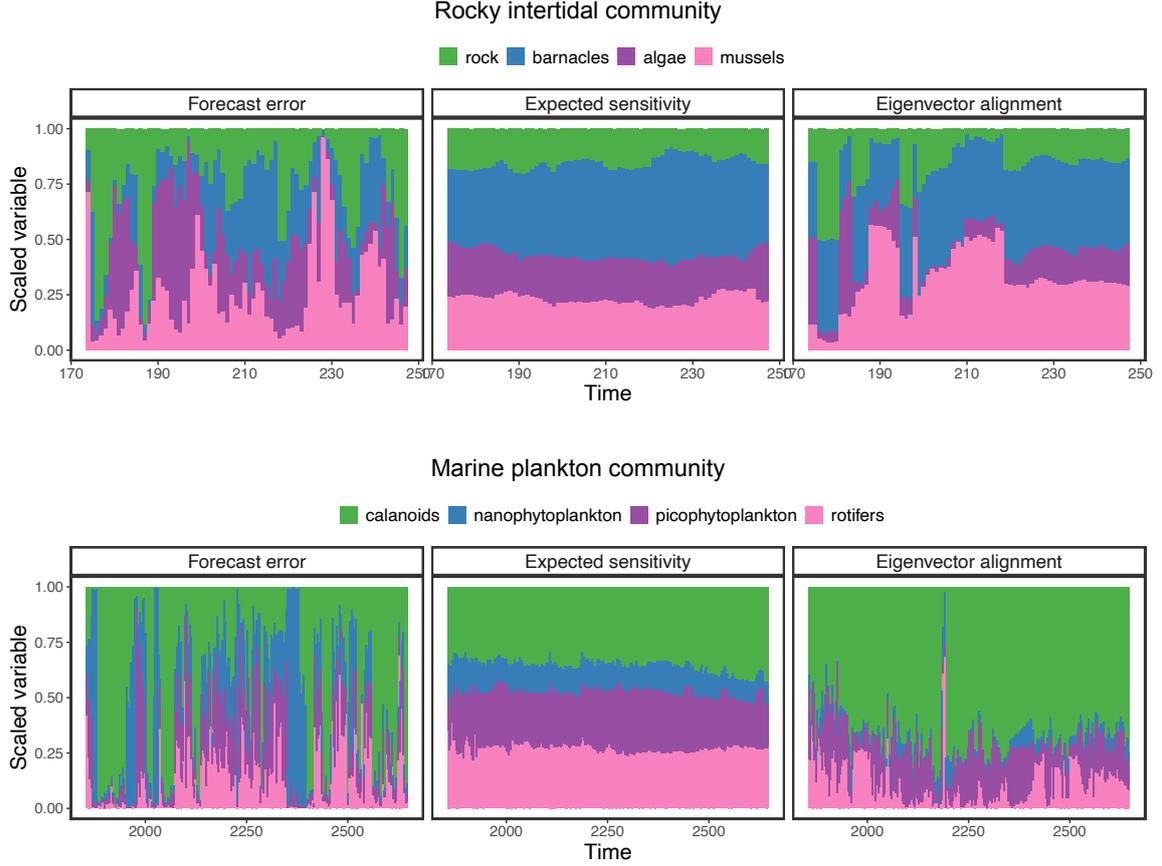
Figure S20. Species standardized forecast root-mean-square error computed from our forecast analyses (ϵ_i; first column; see *Section 7*) as well as expected sensitivities ($\mathbb{E}(s_i)$; second column) and eigenvector alignments ($|\mathbf{v}_{1i}|$; third column) inferred from each empirical time series (different rows) with the S-map over time. A bar in one of the plots shows the values of the corresponding variable (i.e., ϵ_i, $\mathbb{E}(s_i)$, or $|\mathbf{v}_{1i}|$) across species. Note that variables are rescaled to sum 1 across species to improve visualization but that this procedure does not change the rankings. These results correspond to our main set of analyses with empirical time series shown in the main text (Fig. 4).
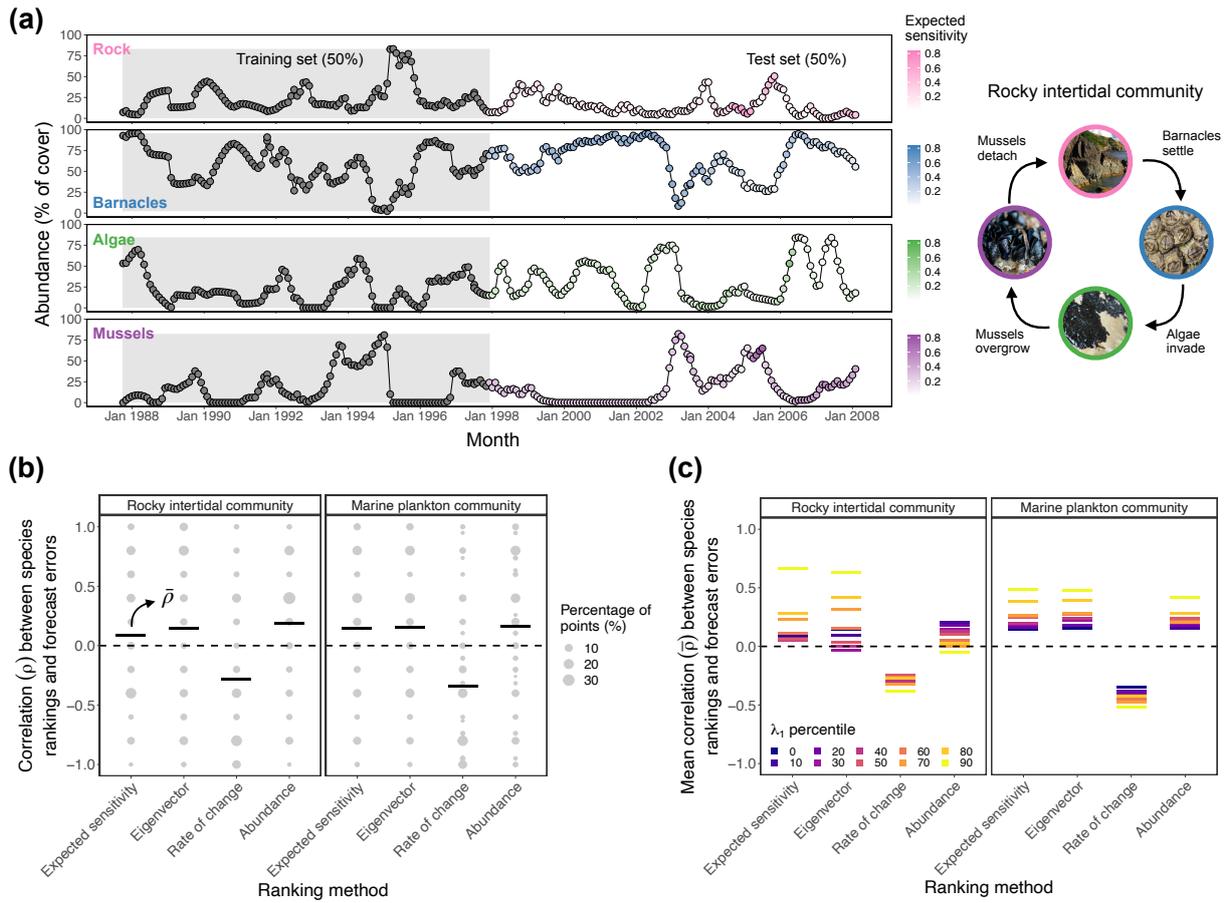
Figure S21. Same as Fig. 4a in the main text but for the empirical time series of marine plankton species (Benincà *et al.*, 2009) (see *Section 7*). Each panel shows the time series of the abundance of a given species with points colored according to their expected sensitivity value ($\mathbb{E}(s_i)$). We infer $\mathbb{E}(s_i)$ at the last point in the training set with the S-map trained on a moving training set (gray region) containing (a) 70%, (b) 60%, or (c) 50% of the whole time series. In general, calanoids are the most sensitive species followed by rotifers or picocyanobacteria depending on the point in time.
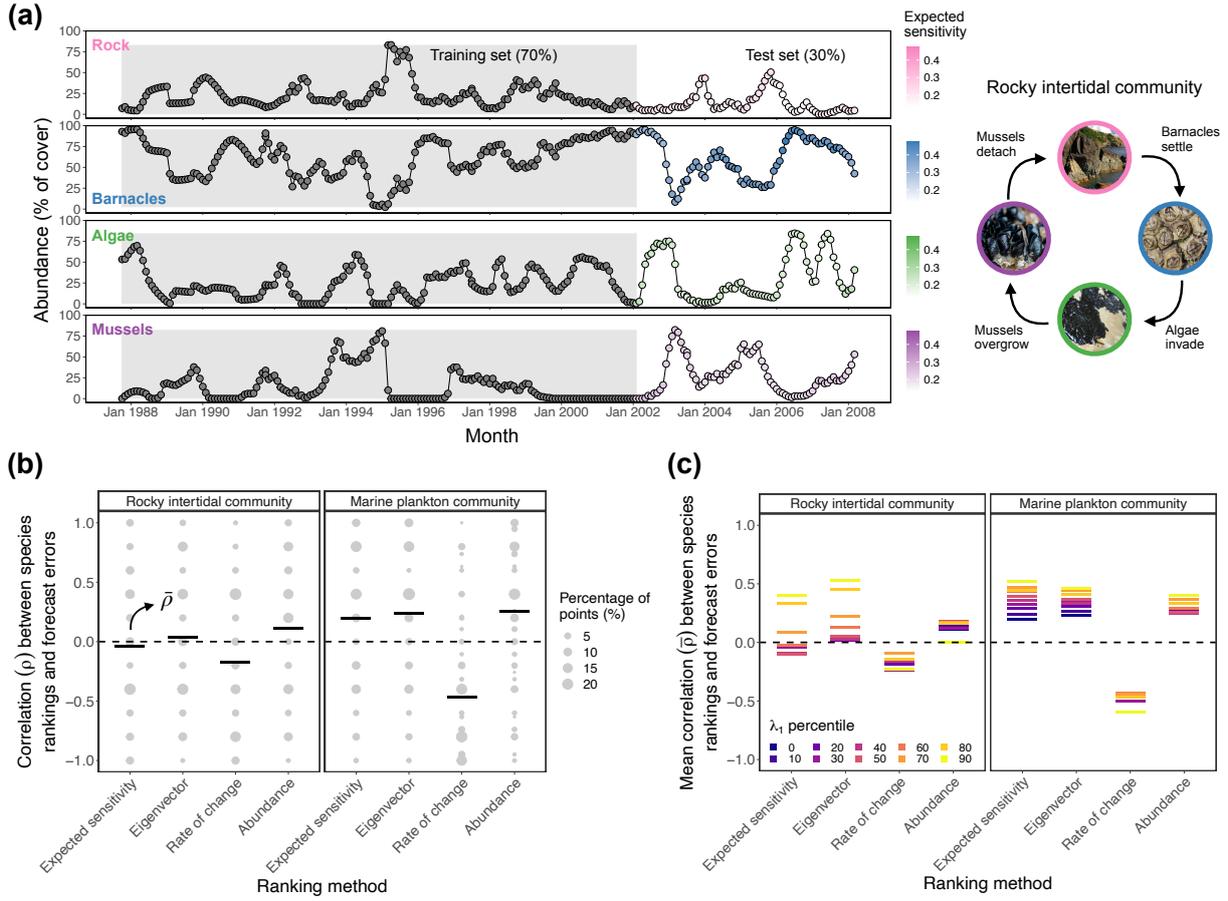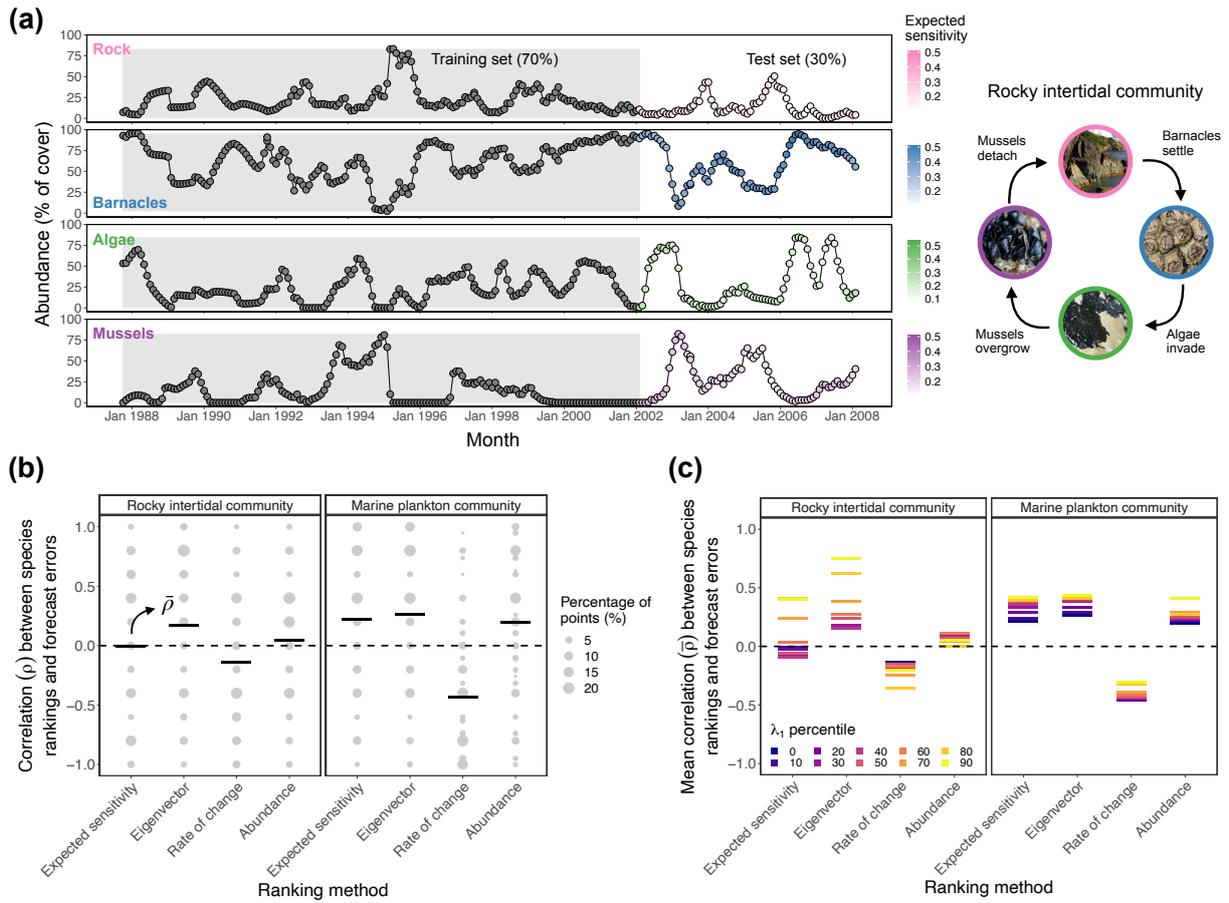
Figure S22. Same as Fig. 4 in the main text but using $\tau = 2$ steps ahead to forecast species abundances and compute forecast errors (ϵ_i) instead of $\tau = 3$ (see *Section 7*). Note that here we use $k = 2$ instead of $k = 3$ to compute expected sensitivities ($\mathbb{E}(s_i)$). (a) Time series of a rocky intertidal community containing four species with point color depicting their expected sensitivity value. (b) Rank correlation (ρ) between ϵ_i and four different approaches (expected sensitivity, $\mathbb{E}(s_i)$; eigenvector, $|\mathbf{v}_{1i}|$; rate of change, $\Delta N_i(t)$; and abundance, $-N_i(t)$). Each panel shows the percentage of points with a given ρ value (size of gray points) and the average of these values across the test set ($\bar{\rho}$, horizontal lines) for a given empirical time series. (c) Average correlation ($\bar{\rho}$) between ϵ_i and the different ranking approaches computed for points in the test set that have a λ_1 value higher than a given percentile of the λ_1 distribution.

41
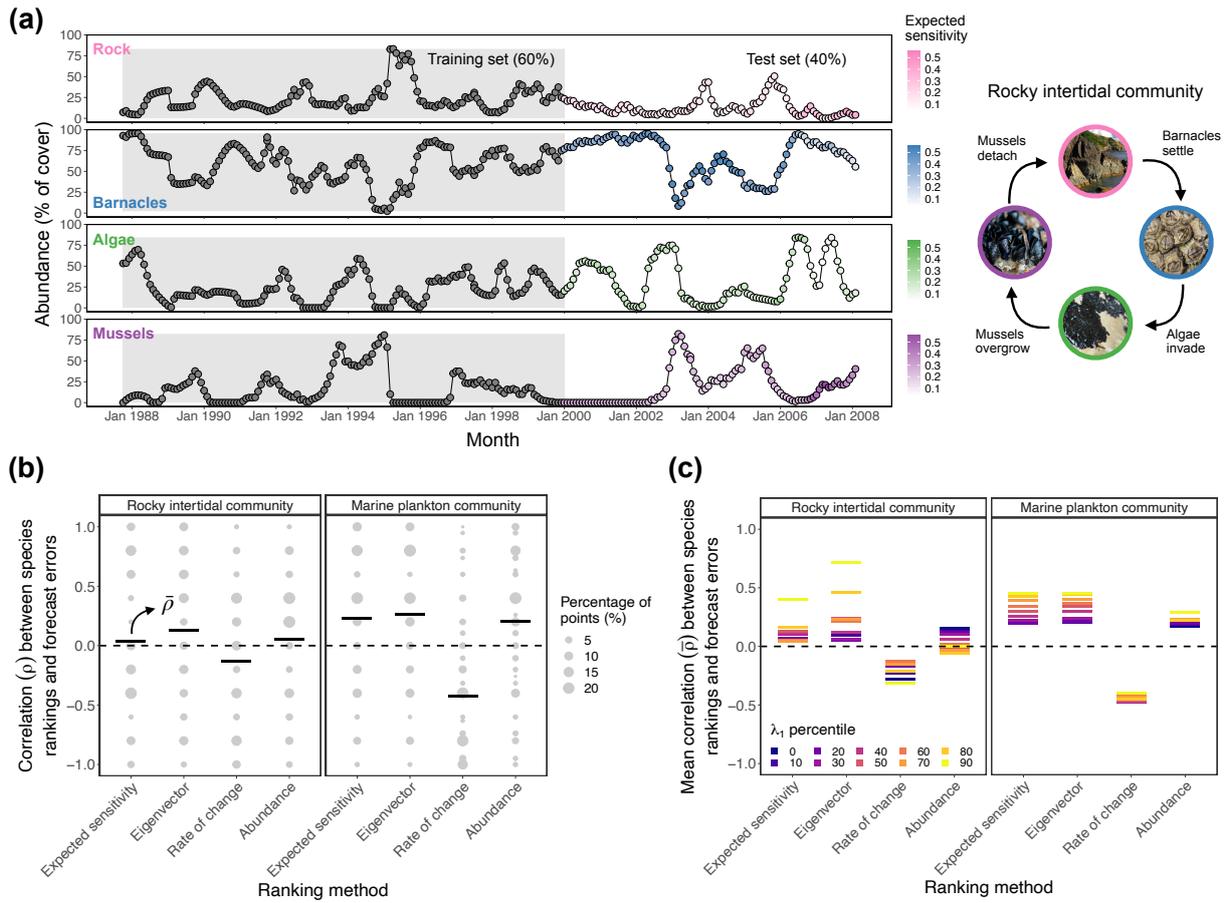
Figure S23. Same as Fig. 4 in the main text but using 60% instead of 70% of the each empirical time series as the moving training set (gray region in (a); see *Section 7*). (a) Time series of a rocky intertidal community containing four species with point color depicting their expected sensitivity value ($\mathbb{E}(s_i)$). (b) Rank correlation (ρ) between ϵ_i and four different approaches (expected sensitivity, $\mathbb{E}(s_i)$; eigenvector, $|\mathbf{v}_{1i}|$; rate of change, $\Delta N_i(t)$; and abundance, $-N_i(t)$). Each panel shows the percentage of points with a given ρ value (size of gray points) and the average of these values across the test set ($\bar{\rho}$, horizontal lines) for a given empirical time series. (c) Average correlation ($\bar{\rho}$) between ϵ_i and the different ranking approaches computed for points in the test set that have a λ_1 value higher than a given percentile of the λ_1 distribution.

Figure S24. Same as Fig. 4 in the main text but using 50% instead of 70% of the each empirical time series as the moving training set (gray region in (a); see *Section 7*). (a) Time series of a rocky intertidal community containing four species with point color depicting their expected sensitivity value ($\mathbb{E}(s_i)$). (b) Rank correlation (ρ) between ϵ_i and four different approaches (expected sensitivity, $\mathbb{E}(s_i)$; eigenvector, $|\mathbf{v}_{1i}|$; rate of change, $\Delta N_i(t)$; and abundance, $-N_i(t)$). Each panel shows the percentage of points with a given ρ value (size of gray points) and the average of these values across the test set ($\bar{\rho}$, horizontal lines) for a given empirical time series. (c) Average correlation ($\bar{\rho}$) between ϵ_i and the different ranking approaches computed for points in the test set that have a λ_1 value higher than a given percentile of the λ_1 distribution.

43

Figure S25. Same as Fig. 4 in the main text but normalizing the abundances of each species i ($N_i(t)$) in the training set to mean zero and unit standard deviation before performing the S-map (see *Section 7*). Note that we always normalize abundances before the forecast analyses (i.e., LSTM neural network). (a) Time series of a rocky intertidal community containing four species with point color depicting their expected sensitivity value ($\mathbb{E}(s_i)$). (b) Rank correlation (ρ) between ϵ_i and four different approaches (expected sensitivity, $\mathbb{E}(s_i)$; eigenvector, $|\mathbf{v}_{1i}|$; rate of change, $\Delta N_i(t)$; and abundance, $-N_i(t)$). Each panel shows the percentage of points with a given ρ value (size of gray points) and the average of these values across the test set ($\bar{\rho}$, horizontal lines) for a given empirical time series. (c) Average correlation ($\bar{\rho}$) between ϵ_i and the different ranking approaches computed for points in the test set that have a λ_1 value higher than a given percentile of the λ_1 distribution.